Design and Fabrication
of Carbon Nanotube Array
based Field Emission Cathode
for X-ray Tube

by

Yonghai Sun

A thesis

presented to the University of Waterloo

in fulfillment of the

thesis requirement for the degree of

Doctor of Philosophy

in

Systems Design Engineering

Waterloo, Ontario, Canada, 2013

Author's Declaration

I hereby declare that I am the sole author of this thesis. This is a true copy of the thesis, including any required final revisions, as accepted by my examiners.

I understand that my thesis may be made electronically available to the public.

Abstract

Field emission cathodes have proven themselves to be excellent candidates for some special medical X-ray applications. Spindt cathode and CNT (carbon nanotube) based field emission cathode have been widely studied for many years. Spindt cathode has the near perfect structure, but the material property limits its applications. On the other hand, low density vertically aligned CNT array has been proved the best candidate of field emission material. Several attempts have been made to combine the advantages of the Spindt cathode and CNT array, but some most important advantages of Spindt cathode have not been successfully utilized in CNT emitter design, for example: ballast resistor, self-aligned fabrication process, sub-micron scale gate electrode, and low control voltage.

In this thesis, the design, fabrication and test of CNT based field emission cathode with a novel ballast resistor and coaxial cylinder shape gate electrode is reported. A connection pad has been reported for the first time. This structure makes the ballast resistor can be utilized in a CNT field emitter array. Therefore, the uniformity and stability of field emission current is improved significantly. In addition, the stabilized emission current heated up the sample to a high temperature and changes the emission from field emission to Schottky emission regime. This is the first report of the self-heating Schottky emission from a CNT emitter array. Coaxial cylinder shape gate electrode is another important improvement in the CNT emitter design. The gate electrode adopts the self-alignment property of the Spindt cathode, and adjusted to fit the structure and synthesis process of CNT array. This new design and fabrication process has all the advantages of both the Spindt cathode and CNT emitter.

In addition to the field emission cathode design, a novel PMMA (poly methyl methacrylate) based FEM (field emission microscope) is designed to evaluate the emission

uniformity and capture high resolution images of the distribution of field emitted electrons. Compare to the conventional phosphor screen based FEM, the PMMA based FEM has a much higher resolution and sensitivity. Images of this new FEM have a resolution of as high as 0.34 nm and clearly show the boundary of crystal facets.

Acknowledgements

Dedication

This work is dedicated to my parents, my loving wife and our amazing kids.

Table of Contents

List of Figures

List of Tables

List of Abbreviations

CNT	carbon nanotube
CT	X-ray computer tomography
CVD	chemical vapor deposition
DC	direct current
FEM	field emission microscope
F-N equation	Fowler–Nordheim equation
IC	integrated circuit
IPA	Isopropyl alcohol
MIBK	Methyl isobutyl ketone
MOSFET	metal–oxide–semiconductor field-effect transistor
MWCNT	multi wall carbon nanotube
NDT	non-destructive testing
NEA	negative electron affinity
PECVD	plasma enhanced chemical vapor deposition
PMMA	poly methyl methacrylate
PTFE	polytetrafluoroethylene
QFP	quad flat package
SWCNT	single wall carbon nanotube
ZnO	zinc oxide

Chapter 1
Introduction

1.1 Motivation

The motivation behind the work in this dissertation is to develop a carbon nanotube (CNT) based field emission cathode for X-ray source that can be integrated into either a stationary computer tomography (CT) scanner system for medical diagnosis or an electronic brachytherapy system for cancer treatment.

The ultimate purpose of this project is to develop some novel X-ray sources that cannot be achieved with current widely used thermionic emission cathodes. The thermionic cathodes used in current X-ray tubes are made of conventional machining technology. This fabrication method limits the size of thermionic cathode. In addition, the thermionic emission limits the switching speed of the cathodes. To overcome these limitations, new electron emission cathodes are desired. Field emission cathodes have been successfully demonstrated, but are still far from commercialization. Stability, uniformity, brightness, and lifetime of field emission cathodes need significant improvement.

Early studies of other research groups demonstrate that Spindt cathode and CNT thin film emitters are the most successful field emission cathodes by far. We found both Spindt cathode and CNT emitters have their own advantages and disadvantages. To achieve a high performance field emission cathode, a new field emission cathode is designed to combine the advantages of both Spindt cathode and CNT emitters and avoid their disadvantages. The emission cathodes are made in micro-fabrication facilities. Similar to Spindt cathodes, the fabrication processes of the cathode are self-assembly.

1.2 Thesis Organization

This section provides a brief outline of the material covered in this thesis.

In Chapter 1 the motivation behind the work done for this project is discussed.

Chapter 2 presents the brief history and some major medical applications of X-ray. The fundamentals of electron emission and theory of field emission are also described.

Chapter 3 describes the materials and structures of previous achieved field emission cathodes. Field emission property of nano-materials used in our early studies is compared. By reviewing the results of our early studies, a carbon nanotube (CNT) based field emission cathode structure is developed. A novel ballast resistor layer and a cylinder shape coaxial gate electrode are used in the emission cathode for the first time.

Chapter 4 presents numerical simulation results of the field emission cathodes. Effects of ballast resistor, dimension of ballast resistor, and efficiency of coaxial gate electrode are calculated.

Chapter 5 presents the fabrication process of the device. The fabrication process is divided into three parts, namely: ballast resistor, CNT, and cylinder shape coaxial gate electrode.

Chapter 6 presents the emission property of the non-gated and gated CNT emitters. During an experiment of the non-gated CNT emitter, self-heating Schottky emission is observed and reported for the first time.

In Chapter 7, a PMMA (poly methyl methacrylate) based field emission microscope (FEM) is described. The structure is designed to evaluate the emission uniformity of field emission array. Resolution of this FEM is 0.3 nm. The FEM has the capability of capture details of the crystal structure of the emission site. Boundary of crystal facet is clearly shown for the first time.

In Chapter 8, diode and triode structured field emission X-ray tube is described. Experimental result and X-ray images from a diode X-ray tube are given. In addition, the thin film based field emission cathode is transparent to X-ray beam. Therefore, a reflection target X-ray tube is feasible.

Chapter 9 presents the contribution and future works of this research.

Chapter 2

Background

2.1 Brief History of X-ray Tube

X-ray was first discovered in 1895 by German physicist Wilhelm Röntgen, when he was working with a cathode ray tube [1]. Figure 2-1 shows the first X-ray picture of the human body ever taken [2]. This cathode ray tube is a discharge tube called Crookes tubes invented by British physicist William Crookes [3]. Crookes tubes require a small amount of air in them to function (7×10^{-4} - 4×10^{-5} Torr). Crookes tubes generate electrons needed to create X-ray by ionization of residual air in the tube, instead of a cathode. Crookes tubes are unreliable and temperamental. Both the energy and the quantity of X-rays produced depend
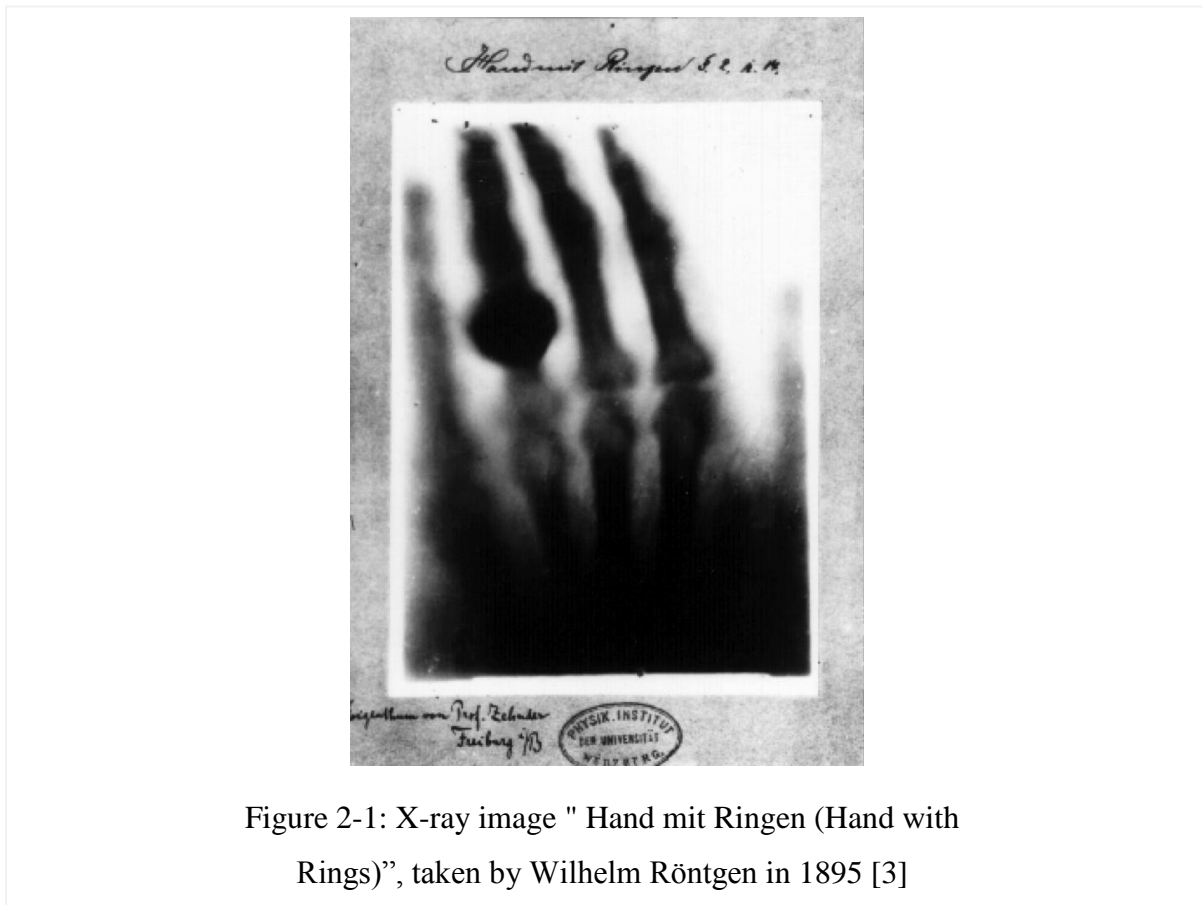
Figure 2-1: X-ray image " Hand mit Ringen (Hand with Rings)", taken by Wilhelm Röntgen in 1895 [3]
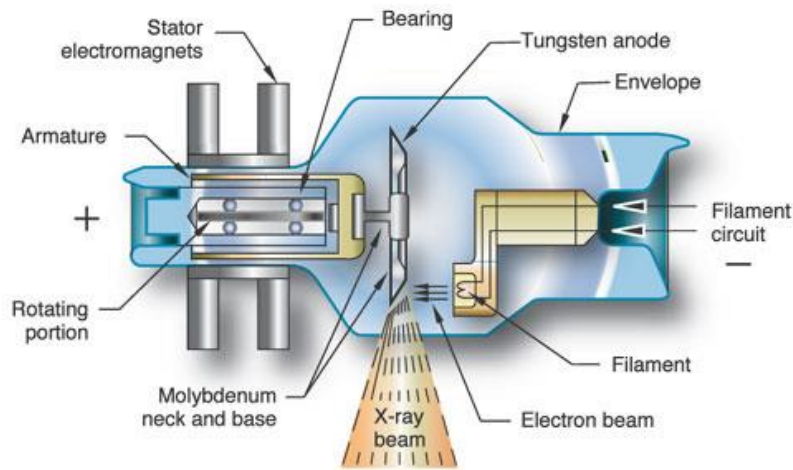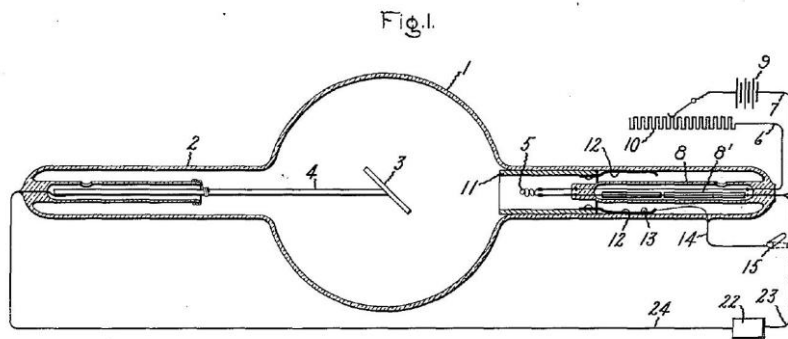
Figure 2-2: Structure of the X-ray tube invented by Coolidge (upper)

[5] and a modern medical X-ray tube (lower) [6]

on the pressure of residual gas in the tube. Over time, the gas is absorbed by the walls of the

tube, and the pressure in the tube is reduced. This pressure reduction reduces the amount of

cathode rays produced and causes the voltage across the tube to increase. Soon the pressure

got so low the tube stops working entirely. These first generation cold cathode X-ray tubes

are used until the 1920s.

In 1913, an American physicist William David Coolidge made a major contribution

to X-ray machines [4]. He invented a hot cathode tube. Electrons are produced from a

tungsten filament heated by an electric current. Coolidge tube consists of a tungsten filament
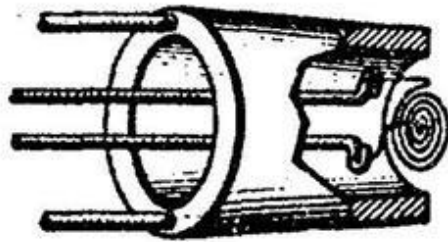
Figure 2-3: Early Coolidge tube cathode (left) [4] and modern X-ray tube cathode (right) [6]

cathode and a metal anode. It has been the most widely used x-ray source till today. Figure 2-2 shows the structure of an early Coolidge X-ray tube [5] and a modern X-ray tube [6]. Many new features have been employed in X–ray tubes and improve the performance of modern X-ray tubes significantly. However, the cathode has no big change in the past one hundred years. Figure 2-3 shows the structures of an early Coolidge cathode [4] and a modern X-ray tube cathode [6].

2.2 Medical Applications of X-ray

2.2.1 Computer Tomography

X-ray computed tomography (CT) is an important application of X-ray in both medical diagnose and industrial non-destructive testing (NDT). In a medical CT scanner, an X-ray tube, a power supply, and an X-ray detector array are mounted on a supporting gantry and rotated around a patient to collect radiation images from different directions [7]. In a typical industrial CT scanner, X-ray components are fixed, but the object makes a full 360° rotation during a scan. The collected X-ray image set is converted to 3D images by a reconstruction algorithm [8].
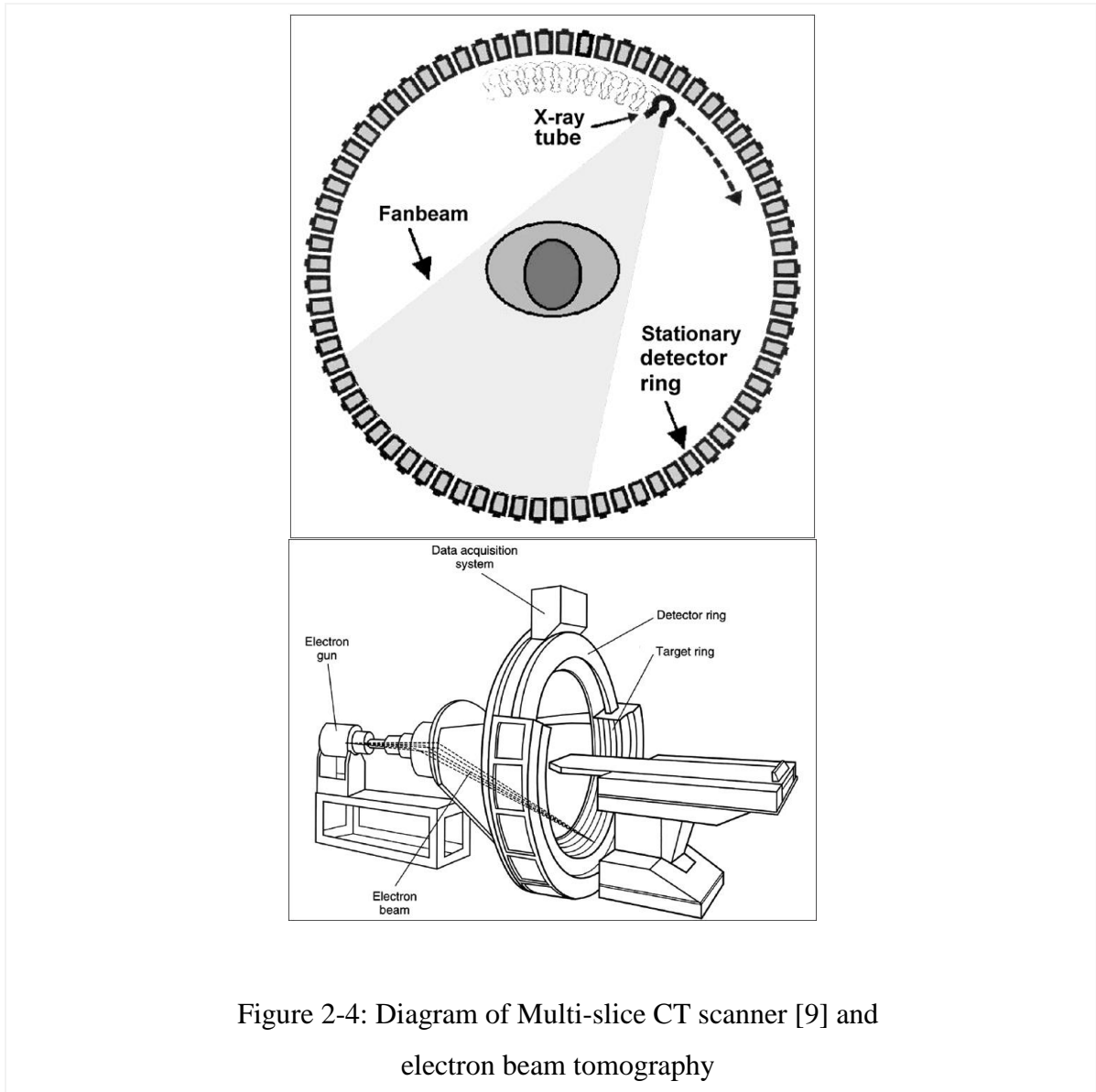
Figure 2-4: Diagram of Multi-slice CT scanner [9] and

electron beam tomography

After the first commercially viable CT scanner is announced in 1972, the progress of

CT scanner is rapid. The fourth generation CT scanner appears in 1978, just six years after

the first CT scanner [9]. In a current fourth generation CT scanner, several thousand of X-ray

detectors are statically mounted all around the gantry to avoid of ring artifact. And the

mechanical motion is the rotation of the x-ray source around a fixed detector array. A fourth

generation multi-slice CT has a resolution as high as 0.2 mm and the slice acquisition time of

320 ms can be achieved. However, it is still not fast enough for a cardiac scanning. Electron

beam tomography is the fastest scanning technology, which can achieve an acquisition time of 50 ms. Figure 2-4 shows diagrams of a multi-slice CT scanner and an electron beam tomography. However, the posterior left ventricular wall moved at a maximum velocity of 52.5 mm/sec, necessitating a scan time of 19.1 ms or less to avoid artifact [10]. Therefore, a technology with a faster scanning speed is still desired. For a conventional CT scanner, to achieve such a high scanning speed, the gantry speed of 5 rotations per second will generate a centrifugal force as high as 75G, which is not feasible. The maximum achievable rotation speed is 3 rotations per second. Throughout all the CT scanning technologies, the maximum of two X-ray sources have been achieved [11]. When compared to the several thousand X-ray detectors, the solo-source or dual-sources becomes the bottleneck of CT scanners. Multi-pixel X-ray source is a potential technology to solve this problem.

Besides the mechanical challenge, power density of the X-ray sources is another obstacle. For a body CT, approximately 250 mAs (i.e., tube current in milliamps times scan time in seconds) per slice are required [12]. For a 20ms scanning time (no motion artifact cardiac scan), the required tube current is 12.5 Amps. A typical target voltage of a CT scanner is 80kV to 140kV. The corresponding target power is over 1 megawatt. Therefore, it is extremely difficult to avoid the target being melted.

In addition to the challenges of the mechanical strength and power density, the high speed mechanical rotation leads to high power consumption, high cost, complex structure, and high maintenance cost. Therefore, a multi-source stationary CT scanner is a solution to overcome these problems.

With the development of the reconstruction algorithm, full circle rotation is not necessary to reconstruct 3D images. In an electron beam tomography, a 210˚ sweep is

sufficient [13]. In a digital tomosynthesis, the tube rotates 40˚ and 2 or 3 exposures are made every 1˚ [14]. These reconstruction algorithms make a multiple X-ray source based 3D image X-ray system feasible.

2.2.2 Electronic Brachytherapy

Brachytherapy, also known as internal radiotherapy, is a form of radiotherapy where a radiation source is placed inside or next to the area requiring treatment. A key feature of brachytherapy is that the irradiation only affects a localized area around the radiation sources. Exposure to radiation of healthy tissues further away from the sources is therefore reduced [15]. In addition, if the patient moves or if there is any movement of the tumor within the body during treatment, the radiation sources retain their correct position in relation to the tumor. These characteristics of brachytherapy provide advantages over external beam radiotherapy, i.e., the tumor can be treated with very high doses of localized radiation, whilst reducing the probability of unnecessary damage to surrounding healthy tissues.

Electronic brachytherapy is a type of radiotherapy that uses a miniaturized high dose rate X-ray source to apply radiation to the cancerous site. It combines the benefits of external beam radiation therapy and traditional brachytherapy to successfully treat breast, skin and gynecological cancer. Patients who undergo this unique treatment can achieve effective results without the dangerous side effects and lengthy downtimes often associated with treating these conditions. Electronic brachytherapy system enables clinicians to administer high-dose-rate brachytherapy for skin lesions without the use of a radioactive isotope or a megavoltage linear accelerator. It can be performed at locations without requiring a heavily shielded room, due to minimal shielding required at these low energies with a faster dose fall-off. As the therapists can remain at the patient side during treatment, visual monitoring

9
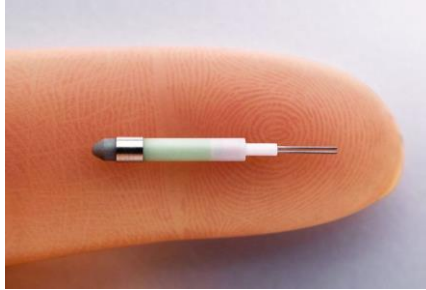
Figure 2-5: Miniature X-ray tube for electronic
brachytherapy system [16]

of applicator set-up, procedure and patient during the treatment is possible and increases

patient comfort and cooperation and improves targeting of the tumor. Due to the low kilo-

voltage energy level, near ocular treatments are possible with thin tungsten eye-shields. On

and off switch and quick stop capability of the controller provide increased procedural safety.

Figure 2-5 shows a miniature X-ray tube for electronic brachytherapy system. Due to its

miniature size, the design of the X-ray tube has many limitations, for example, the lifetime of

the X-ray tube is just 150 minutes [16]. In briefly, lifetime and preference of the tiny X-ray

tube still needs some improvements.

2.2.3 Other Applications of X-ray Irradiation

Radiation sterilization refers to a process that using radiation such as electron beam,

X-ray, gamma ray or subatomic particle to kill all forms of microbial life present on a

surface, contained in a fluid, in medication or in a compound. Food irradiation is used in

many countries to control foodborne pathogens, reduce microbial load and insect infestation,

and extend the durable life of perishable produce [17]. Radiation is also a useful process in

medicine production and medical device sterilization [18]. Sterilization through irradiation is

considered a clean and efficient process. Irradiation with X-ray or gamma ray does not make

materials radioactive. Furthermore, irradiation of blood is used in many countries to eliminate the risk of fatal graft-versus-host disease [19].

Nowadays, irradiations are done with radioactive isotopes, which require heavy lead shielding and have the risk of radiation leakage. Some facilities use high energy X-ray beam to irradiate large packages and pallet loads of medical devices, or other products. X-ray sterilization is an electricity based process, and do not require any radioactive materials. When the radiation source is turned off, there is no radiation generated. Therefore, the X-ray devices do not require any shielding during storage or transport. Conventional X-ray tubes are point sources, which are not designed for continuously irradiating a large area or volume. A flat panel X-ray source has many advantages over a point source in X-ray irradiation applications [20, 21]. First, the X-ray beam is more uniform in the irradiated area. Second, the X-ray target has a much lower power density; therefore, the lifetime of the target is significantly increased. Third, a uniform radiation beam can decrease the target-object distance and makes the facility small and increase the power efficiency.

2.3 Electron Emission from Solids

Electron sources are one of the most important components in many devices, which include electron microscopes, microwave amplifiers, displays, cathode ray tubes and X-ray sources. The most widely employed electron source is still the thermionic cathode. A general theoretical description of electron emission was provided by Murphy and Good [22] and later verified experimentally by Christov and Vodenicharov [23] for a wide range of surface electric fields and temperatures. The Murphy-Good theory provides a complex integral expression for the electron emission current density that can only be evaluated numerically. As a consequence, the much simpler Fowler–Nordheim [24] and Richardson–Dushman [25]

11
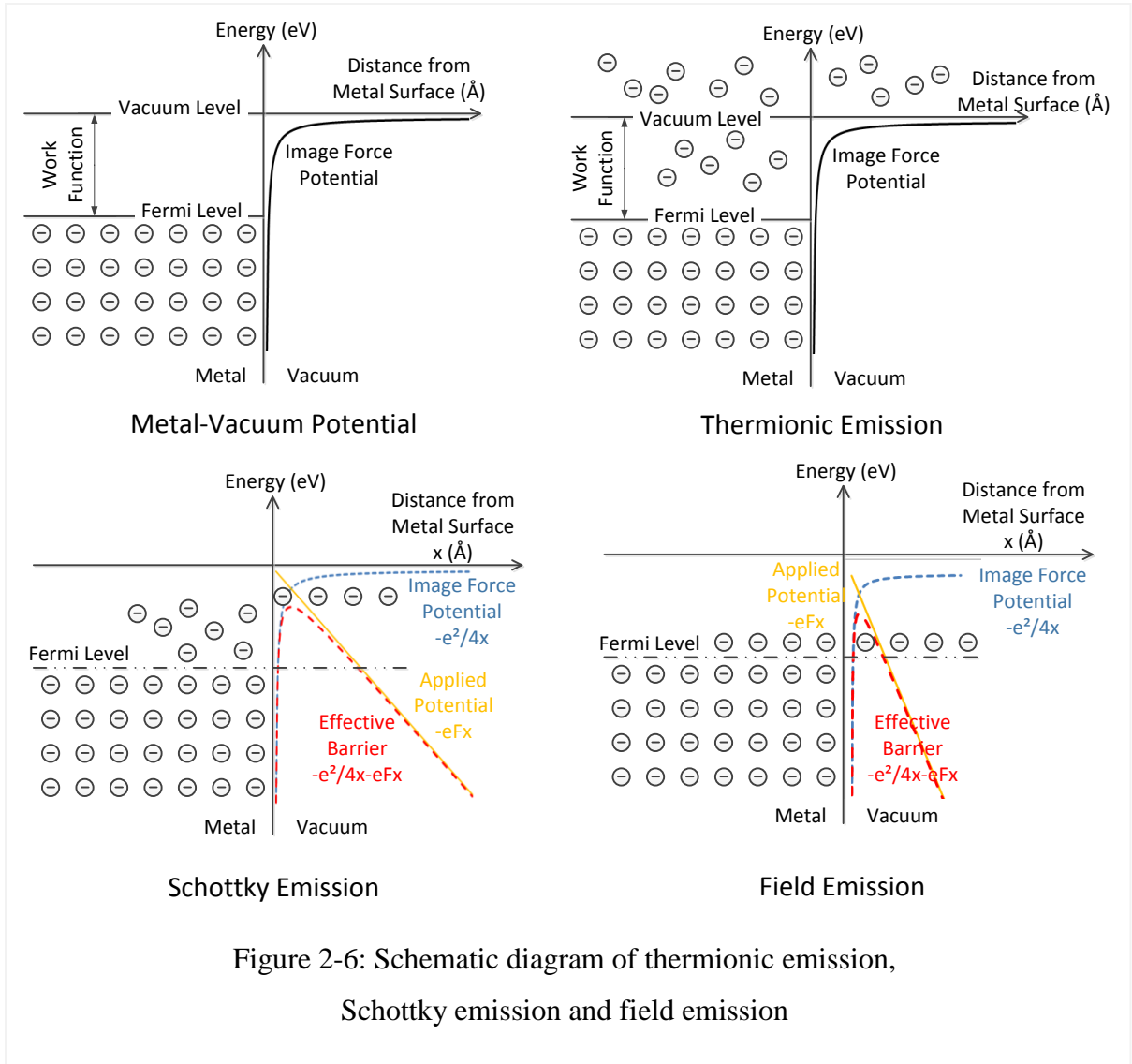
Figure 2-6: Schematic diagram of thermionic emission,
Schottky emission and field emission

analytical equations are widely used, respectively, for field emission and thermionic emission.

2.3.1 Thermionic Emission

In a solid, electrons tend to fill the lowest energy states. At a temperature of 0 K, every low-energy states is occupied, right up to the Fermi level, but no states are filled at energies greater than the Fermi level. At the material-vacuum interface, an image force potential prevents the electrons leave the surface and escape into vacuum. Figure 2-6A shows a diagram of the energy distribution of electrons in an electron emission material at a

temperature of 0 K. When the solid is heated up, kinetic energy of the electrons increases. Electrons, with kinetic energy higher than the potential barrier, can overcome the image force and exit the solid surface without being pulled back in. This phenomenon was first observed by Thomas Edison in 1883 and is known as the Edison effect. The concept of thermionic emission is diagrammatically shown in Figure 2-6B. At the temperature of operation, an electron cloud is formed surrounding the material. The cloud of emitted electrons can form a space charge region, which is treated as a continuum of charge distributed over a region of space rather than distinct point charges. The resulting cloud is negatively charged, and can be attracted to any nearby positively charged object, thus producing an electrical current which passes through the vacuum. Such a cloud acts to repel low-energy electrons, which return to the cathode. This limiting mechanism is aptly referred to as the space-charge-limited operation. In a vacuum electron device, a positive voltage applied to an anode electrode to attract electrons from the cloud. The higher the voltage, the more electrons flow to the anode until all the emitted electrons are attracted to the anode. At this point, the electron flow is known as the saturation current. The thermionic emission can be quantifying described by the Richardson-Dushman equation [25]

$$J_{RD} = AT^2 e^{-\frac{\varphi}{k_B T}} \tag{2.1}$$

and Langmuir-Child law [26, 27]

$$J_{LC} = 2.33 \times 10^6 \frac{V_a^{\frac{3}{2}}}{d^2} \tag{2.2}$$

where J is current density, A is a constant of the material and its surface finish, T is the temperature of the solid, φ is the work function of the material, k_B is Boltzmen's constant, V_a is the anode voltage, and d is the distance between the anode and the cathode. The

Richardson-Dushman equation describes the quantity of electrons that can be emitted from the cathode, and the Langmuir-Child equation describes the quantity of electrons that can pass through the vacuum is limited by the mutual repulsion [28].

2.3.2 Schottky Emission

At a certain temperature, the saturation voltage is a voltage applied to the anode to attract all the emitted electrons from the thermionic emission cathode to the anode. When the applied voltage keeps increasing after reaching the saturation voltage, the emission current keeps increase. This is due to the potential barrier is decreased by the applied electric field. This phenomenon is known as Schottky effect. Potential energy diagram for Schottky emission is shown in Figure 2-6C. The current density of Schottky emission is a function of electric field, emitter temperature, and work function. The Schottky emission can be quantifying described by the Richardson-Dushman equation corrected for Schottky effect [29]

$$J_S = A_R(k_B T)^2 e^{\left(-\frac{\varphi - \Delta\varphi}{k_B T}\right)} \tag{2.3}$$

$$\Delta\varphi = \sqrt{\frac{e^3 F}{(4\pi\epsilon_0)}} \tag{2.4}$$

where A_R is the Richardson constant, k_B is the Boltzmann constant, T is the emitter temperature, φ is the work function of the emitter material, F is the electric field strength at the tip, and ϵ_0 is the permittivity constant. $\Delta\varphi = 3.79 F^{1/2}\ eV$ represents the lowering of the barrier height brought by the applied field. The current density is strongly dependent on both the tip temperature and the electric field strength at the surface.

The Schottky emission is further divided into thermal assisted field emission [30] and field enhanced thermionic emission [31] depends on the difference of the operating electric

field and temperature. Schottky emission cathodes have many advantages over thermionic emission cathodes, For example, small effective source radius, high brightness, long lifetime, and narrow electron energy distribution. Thus Schottky emission cathodes are the most advanced electron source commercially available. They are widely used as point sources in electron devices such as scanning electron microscope, transmission electron microscope, and electron-beam lithography.

2.3.3 Field Emission

Field electron emission is a pure quantum mechanical effect. The phenomenon of electrons emitter from platinum in an intense electric field was discovered by R.W. Wood in 1897 [32]. This phenomenon occurs when the electric field strength is at the scale of 10^9 V/m. In order to produce such high electric fields, the emitter is usually formed into a tiny tip, which has apex radius range from several nanometers to sub-micrometer. The electric field concentrates at the emitter tip and narrows the potential barrier at the metal-vacuum interface to several nanometers. Therefore, the free electrons in the metal have a significant probability of tunneling from the solid into the vacuum. Potential energy diagram for field emission is shown in Figure 2-6D.

2.3.3.1 Needle Tip Emitter

In the early years, the metallic needle tips are fabricated by fusing or chemical etching a thin filament. The radius of the apex is at micrometer scale. Field emission microscope (FEM) studies show that only metal with a high melting point, like tungsten and molybdenum, can show stable images. Since the work functions of tungsten and molybdenum are around 4.5 eV, which is much higher than that of some electropositive materials, like sodium (2.36 eV) and thorium (3.4 eV), studies of coating a thin film of metal

with low work function to tungsten tips started form the very early investigations [33]. In 1937, Muller described that a monatomic layer of thorium coated on a tungsten point cathode can decrease the work function of the cathode to 2.7 eV. He also studied the poisoning of the thorium layer by oxygen and the removal of the thorium layer by ion bombardment and high temperature [34]. In 1940, R. Haefer quantitatively studied the emitter's shape and emitting area and obtained stationary extremely high current densities of 10^6 A/cm², far in excess of those possible with thermal electron emission [33]. In the same year, Fleming and Henderson described the measurement of the cooling effect on a cathode caused by the escape of field and thermionic currents [35]. In 1950s, W. P. Dyke and his group not only achieved a current density of 10^7 - 10^8 A/cm², but also demonstrated a more than 12,000 hr stable operation of field emission cathode in continuous mode with a current density close to the maximum achievable values of $\sim 10^7$ A/cm² in a vacuum of 10^{-12} Torr [36-40]. In these studies, a maximum of continuous 7.5 mA or pulsed 45mA current were drawn from single cold tungsten needle. In 1960s, M.I. Elinson and co-workers found that the maximum current densities depend on emitter geometry and by increasing the tip cone angle the current density could be increased without damage the emitter tip [33]. However, when the etched needles were used as cathodes in miniaturized devices, they have many limitations. The biggest problems are the limited lifetime due to the sputtering damage, and the necessity of using high voltage and maintaining an ultra-high vacuum. The technical difficulties encountered in using etched needles makes the studies stalled.

2.3.3.2 Thin Film Emitter Array

In 1968, C.A. Spindt demonstrated a succeeded in fabricating a gated thin film field emitter array [41, 42]. The emitter array, now known as the Spindt cathode, consists of

16

Figure 2-7 : Diagram and SEM image of Spindt cathode [43].
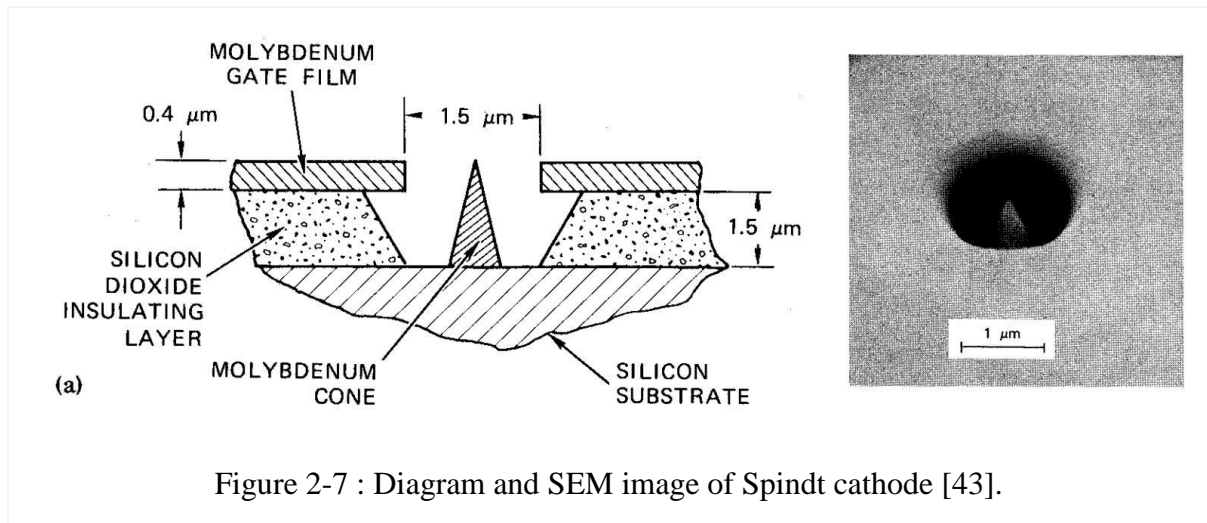
molybdenum cones, a silicon dioxide insulation layer, and a molybdenum gate electrode. Figure 2-7 shows a diagram and a SEM image of the Spindt cathode [43]. This multilayer structure is fabricated on a silicon substrate by thin film vacuum deposition techniques. The fabrication process allows the cathode to be fabricated in arrays of up to thousands emitters. A current density of 10A/cm² was achieved [43]. And they also demonstrated a 2mA total emission current from a 100 cones array in an area of 0.0625mm² for over 7,000 hours [43].

The Spindt cathodes have many inherent advantages in stability. First, the operating gate voltage is range from 100V to 300V, which is much lower than that of needle tip emitters (1,000V to 30,000V) [41]. By shrinking the device dimension, the gate voltage can be reduced to a few tens of volts [44]. Second, the excessive noise of the cathode can be reduced by increasing the number of the emitters in an array. Third, the emission efficiency (anode current/cathode current) is higher than 99%, makes the total cathode current and joule heat much lower than that of other emitters. Fourth, the emitters are fabricated with thin film processes in high vacuum environment, which assure less release gas from substrates. Fifth, the diameter of the emitters are few micrometers and hundreds of emitters can be combined

17

to form a single emission pixel, so even some emitters are failure, the pixel still works properly.

The biggest problem of the metal emitters is if it is operated at a system pressure greater than 10^{-9} Torr, the emission is unstable and the lifetime of the emitter is just a few seconds [45].

2.4 Electron Emission Theory

2.4.1 Fermi-Dirac Statistics

In statistical mechanics, Fermi-Dirac statistics is used to describe the energies of particles that obey the Pauli Exclusion Principle. Fermi-Dirac statistics applies to systems comprising many identical particles, which is called fermions. In these systems, mutual interaction between the particles is assumed to be negligible. Therefore, the many-particle systems can be described in terms of single-particle energy states. In a metal emitter, free electrons are fermions that obey Fermi-Dirac statistics. Electron emission current from a metal emitter increases with the temperature of the metal and the applied electric field. The emission process has been thoroughly studied on the basis of the Fermi-Dirac distribution for a free electron gas and the classical image force barrier. For a system of identical fermions, Fermi-Dirac distribution gives the average number $\bar{n}$ of fermions in a single-particle state i

$$\bar{n}_i = \frac{1}{e^{(E_i - \mu)/k_B T} + 1} \tag{2.5}$$

where $\bar{n}_i$ is the average number of fermions in state i, E_i is the energy of the state i, μ is the chemical potential, k_B is Boltzmann's constant, and T is temperature [46]. When a state has energy ϵ equals chemical potential μ, the state have 50% chance of being occupied by an electron, and the energy of this state is Fermi level. At the temperature of $T = 0K$, Fermi

energy of a metal equals to the Fermi level, and all the electrons are stacked neatly below the Fermi level. To remove an electron from a metal to a point immediately outside the metal surface, the minimum necessary energy equals to the difference between the Fermi level and the energy level of vacuum (absolute energy reference zero). This energy difference is known as work function. Work function is a characteristic property for any solid phase of a substance. In solid-state physics, the free electron model is a combination of the classical Drude model and quantum mechanical Fermi-Dirac statistics. It is also known as Drude-Sommerfeld model. It predicts, in three dimensions, the density of state of a fermions gas is proportional to the square root of the kinetic energy of the particles. This model is successful in explaining experimental phenomena of thermionic electron emission and field electron emission from bulk metals.

2.4.2 Energy Barrier

At the metal-vacuum interface, an energy barrier exists. To calculate the electrostatic force on an electron in the neighborhood of the metal, we assume the metal-vacuum interface is a mirror and the electron is attracted by its electric image. From the Coulomb's law, the image force F_i between an electron and its image is

$$N_i(x) = \frac{e^2}{(2x)^2} \qquad (2.6)$$

where e is electron charge, x is the distance from the electron to the metal-vacuum interface. The image force potential is

$$V_i(x) = -xN_i(x) = -\frac{e^2}{4x} \qquad . \qquad (2.7)$$

When an electric field F is applied, the external applied potential is

$$V_e(x) = -eFx. \qquad (2.8)$$

The assumed potential energy of the electrons near the metal-vacuum interface is

$$V(x) = -\frac{e^2}{4x} - eFx \qquad (2.9)$$

where $V(x)$ is the effective electron potential energy. Term $-\frac{e^2}{4x}$ is the contribution from the image force, and $-eFx$ is the contribution from the externally applied field F. The effective electron potential energy inside the metal is a constant. In the region near $x = 0$, it is assumed that the potential energy $V(x)$ is regular and connects smoothly. The maximum value of the potential energy is $-(e^3 F)^{1/2}$ [22].

2.4.3 Murphy-Good Theory

For high temperature and low field strength, electrons have energy higher than the image force barrier predominates and the emission current variation is determined by the temperature dependence of the distribution function. This process is known as thermionic emission. For high field strength and low temperature, electrons have energy below or close to Fermi level predominates and the emission current variation is determined by the field dependence of the barrier shape. This process is called field emission. The transition region among thermionic emission and field emission is called thermo-field emission or Schottky emission [47]. The thermal-field emission is further divided into field enhanced thermionic emission [31] and thermal assisted field emission [30]. The thermal-field emission current densities can be several orders of magnitude higher than that of thermionic emission, field emission and their simple sum [48].Thermionic emission and field emission can be described by Richardson equation and Fowler-Nordheim equation separately. Some attempts have been made to study the transition region [49-51]. A comprehensive study of the entire emission phenomenon is preformed from a unified point of view [22]. From the free electron model,

we can get the number of electrons per unit time per unit area having energy within a small range incident on the barrier. Then, a function of the probability of the electrons that can escape through the barrier is derived. Next, two integrations are applied on the escape probability function to obtain the total energy distribution and emission current density. The emission current density is a function of temperature, field, and work function in the form of a definite integral [52]

$$J_{M-G} = e \int_{-W_a}^{\infty} D(F,W) N(W,T,\varphi_0) dW \qquad (2.10)$$

where e is electron charge, $-W_a$ is the effective constant potential for the electron inside the emitter, $D(F,W)$ is the probability of the electrons with energy W to penetrate the barrier, $N(W,T,\varphi_0)$ is number of electrons having energy between W and $W + dW$ interval, per unit time incident on unit area of the barrier surface from within the metal, W is the energy of an incident electron on the potential barrier, φ_0 is the work function, F is the applied external electric field and T is the temperature. The equation 2.10, also known as Murphy-Good theory [22], can be used to calculate the emission current density of electron emitter have temperature range from 300 K to 5000 K, electric field range from 10^7 V/m to 10^{10} V/m, and work function range from 2.6 eV to 6 eV. Murphy-Good theory has been experimentally verified for a wide range of surface electric fields and temperature [23]. Murphy-Good theory provides a complex integral expression that can only be evaluated numerically. Therefore, Richardson's law, Schottky equation, and Fowler-Nordheim equation are used for thermionic emission, thermal-field emission, and field emission respectively [24, 47].

2.4.4 Fowler-Nordheim Theory

Fowler-Nordheim theory is developed for calculate field emission from bulk solid materials [24], but they are used for other materials as a rough approximation as well. The theory is based on some assumptions: i) the calculation is preformed for temperature of 0K; ii) the emission surface is planar, therefore, only one-dimensional problem is considered; iii) the potential barrier outside the emitter is a simplified potential model, and the external field do not affect the electron states inside the emitter material [33]. Fowler-Nordheim equation has a similar definite integral form of Murphy-Good equation without a temperature factor. For the simplified potential barrier $V(x) = -\frac{e^2}{4x} - eFx$, the transparency of the barrier can be calculated using the semi-classical method of Wentzel-Karmers-Brillouin (WKB) approximation, which is a method for finding approximate solutions to linear partial differential equations with spatially varying coefficients, and given by

$$D(F, W) = exp\left[-\frac{8\pi(2m)^{\frac{1}{2}}}{3he}\right]\frac{|W|^{\frac{3}{2}}}{F}\vartheta(y) \tag{2.11}$$

where $\vartheta(y)$ is the Nordheim function [33]. Calculation result of the simplified potential barrier is much lower than the current density of experimental results. However, if a more realistic barrier model is used, the function is known to be mathematically impossible to solve.

The Fowler-Nordheim equation is based on an assumption of planar surface. However, to achieve a high electric field with a reasonable potential, the emitter is usually formed into a tip with a nanometer scale apex radius, which is close to or less than the barrier width. In this case, the assumptions of a one-dimensional barrier and field uniformity over the emission site are no longer justified. Therefore, it is necessary to solve the three-

dimensional Schrodinger equation using an asymmetric potential barrier. Due to the complexity of the calculation, only rough calculations have been made. The Fowler-Nordheim equation is simplified as

$$J_{FN} = 1.56 \times 10^{-10} \frac{(\beta F)^2}{\varphi} \, exp\left(-6.83 \times 10^9 \frac{\varphi^{3/2}}{\beta F}\right) \tag{2.12}$$

where J_{FN} is emission current density, β is field enhancement factor, F is applied electric field strength, and φ is the emitter work function. Even though the Fowler-Nordheim theory has some inaccuracy, the simplified Fowler-Nordheim equation is the only simple method to calculate the emission current density.

In Fowler-Nordheim plot, another form of Fowler-Nordheim theory, the quantity $Ln(\frac{I}{F^2})$ is plotted against $1/F$. As predicted by the Fowler-Nordheim equation, this plot should be an exact straight line. Slope (*m*) of the Fowler-Nordheim plot would be $m = -6.83 \times 10^9 \varphi^{3/2}/\beta$. Therefore, the field enhancement factor β can be calculated as long as work function φ is known [53, 54]. Furthermore, the measured intercept (*b*) of the Fowler-Nordheim plot is $b = ln(1.56 \times 10^{-10} A\beta^2/\varphi)$, where A is the effective emission area [54]. Even though there are many inaccuracies, Fowler-Nordheim plot is still the most used method to evaluate electron emission properties of nano-scale field emitters.

2.5 Chapter Summary

In this chapter, the history of X-ray tube and some applications of X-ray are briefly introduced. Electron sources are one of the most important components of the electron devices. Thermionic emitter is the most widely used electron source. However, Schottky emitters and field emitters are used in specific applications. Due to the limitation of the thermionic emission cathode, some applications are not feasible by far. To develop some new

X-ray devices, a novel electron source is desired. Electron sources can be divided into three categories: thermionic emitter, Schottky emitter, and field emitters. The differences between these emissions are described. In addition, electron emission theory is also presented.

Chapter 3
Design of Field Emission Cathode

3.1 Field Emission Material

In the early years, field emission cathodes are always made of metal. Due to the high current density, the emission sites are heated up to a very high temperature by Joule heating and Nottingham effect if the average energy of emitted electrons is higher than the Fermi energy of the cathode material [48, 55]. Furthermore, field emission microscope studies show that only metals with high melting point, like tungsten and molybdenum, can show stable images [33]. As a result, tungsten and molybdenum are the most common materials for field emitters. Since the work functions of tungsten and molybdenum are around 4.5 eV [56, 57], which is much higher than that of some electropositive materials, like sodium (2.36 eV) and thorium (3.4 eV), studies of coating a thin film of metal with low work function to tungsten tips started form the very early investigations. It is demonstrated that a monatomic layer of thorium coated on a tungsten point cathode can decrease the work function of the cathode to 2.7 eV [34]. However, residue oxygen can lead to the thorium coating layer poison and ion bombardment and high temperature can remove the coating layer as well. As a result, the metal field emitters, no matter coated or not, require an ultrahigh vacuum to work stability, otherwise their lifetime is just few seconds [45].

In addition to the high melting point metals, some semiconductor materials, such as silicon, germanium, silicon carbide, zinc sulfide, and zinc oxide, are used to form field emitters as well [58]. Furthermore, diamond, a metastable allotrope of carbon, is also used as a coating material to form negative electron affinity (NEA) field emitter [59]. Theoretically,

these materials have some nature advantages, but outstanding performance from these materials have not been experimentally achieved by far [33].

Carbon is an alternative material for field emitters [60]. Carbon based emitters have strong carbon-carbon covalent bond. This bond makes the emitter has a high electric and thermal conductivity. Furthermore, the C-C band makes surface diffusion of carbon material lower than that of metals; as a result, the apex shape of the carbon emitters is more stable than that of metals. It was reported, for a single needle tip carbon fiber emitter, the lifetime is 2,400 hours at an emission current of 10 µA in a vacuum of 10^7-10^8 Torr [45, 60], which is five orders higher than the required pressure (10^{-12} Torr) of a tungsten emitter. Field emission microscope study shows some individual image spots are stable for hundreds of hours under constant voltage, some others may flicker or vanish [61]. After the first synthesis of fullerene [62], some other allotrope of carbon, such as carbon nanotube (CNT) [63, 64], carbon nanocone [65], carbon nanoform [66] and graphene [67] have been discovered and synthesized. CNT has a nanometer scale diameter, high respect ratio, high thermal and electrical conductivity, high chemical stability, and high melting point [68]. Furthermore, many different synthesis methods have been thoroughly studied to fabricate different kinds of CNTs with well controlled parameters [69, 70]. Therefore, CNT is one of the best candidates of field emission material.

3.2 Structure of Field Emission Cathode

To achieve a high electric field with a reasonable voltage, a nanometer scale sharp tip is commonly used to form a field emitter. In the early years, emitters are made of thin metal rods. The tip is formed by fusing or chemical etching and the radius of the apex is at micron meter scale. Field emitter can provide a current density as high as 10^7-10^8 A/cm² [36, 37], but

the tiny emission apex area limits its total emission current. As a result, emitter arrays or flat panel field emitter are desired to provide a high total emission current. Making a field emitter array with conventional technology is not achievable; therefore, micro/nano fabrication process and nanotechnology are employed to develop field emission arrays with nano-meter scale emitter tips.

3.2.1 Thin Film Field Emitter

With the development of nanotechnology, many nano scale materials are available in different forms, for example: nanowire, nanotube, nanofiber, and nanoparticle. Field emission properties of nano materials are widely studied [71-76]. Among these nano materials, diamond-like-carbon, graphene film, and carbon nanotube thin film based field emission cathode achieve a certain success. There are two major methods to fabricate a nano-material based thin film emitters, i.e.: i) coat or deposit a synthesized nano-material layer on a substrate, for example, spin coat, dip coat, screen print and electrophoresis [77-79]; and ii) direct grow or synthesis such materials on a substrate, for example, chemical vapor deposition (CVD), and plasma enhanced chemical vapor deposition (PECVD) [80, 81].

3.2.1.1 Deposited nano-Structure Film Field Emitter

We started our CNT emitter study with the first method. CNT powder is dispersed in acetone by ultrasound, and then spin coated on a substrate [77]. CNT thin films made with this method have a good uniformity, but the adhesive of the CNT to the substrate is poor. As a result, CNTs can easily be peeled off from the substrate and lead to the emitter failure. To improve the adhesion, conductive adhesive is mixed with the CNT mixture and deposited onto the substrate to form a composite film [82]. Furthermore, some mechanical [83], optical [84], or electro chemistry methods [85] are utilized to active hinder emitters. The CNT thin
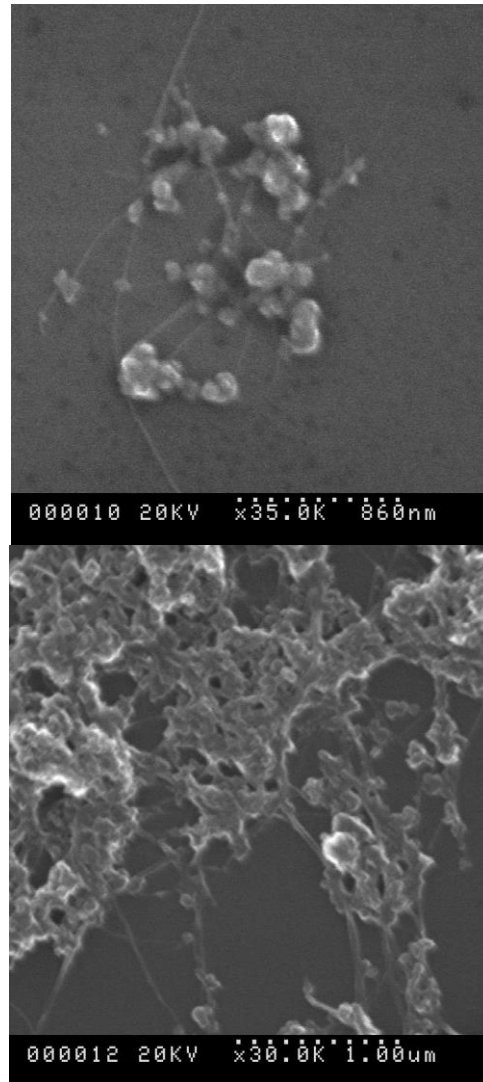
Figure 3-1: CNT thin film emitter composed of CNTs
dispersed in conductive binder matrix. The surface of the
sample is not flat and the CNT density is not controllable.

film field emitter is used in our first X-ray tube prototype. Figure 3-1 shows a SEM image of our CNT thin film emitter. Emission current of 40 uA is achieved and 10 mRad/hour radiation is detected by a dose rate meter. The problem of this emitter is the emission current degrades very fast and the lifetime of the emitter is just several minutes. During the experiment, green glows are captured by a video camera. Visible light emitted from CNT during field emission may lead by a high temperature [86] or micro-arc discharges [79].
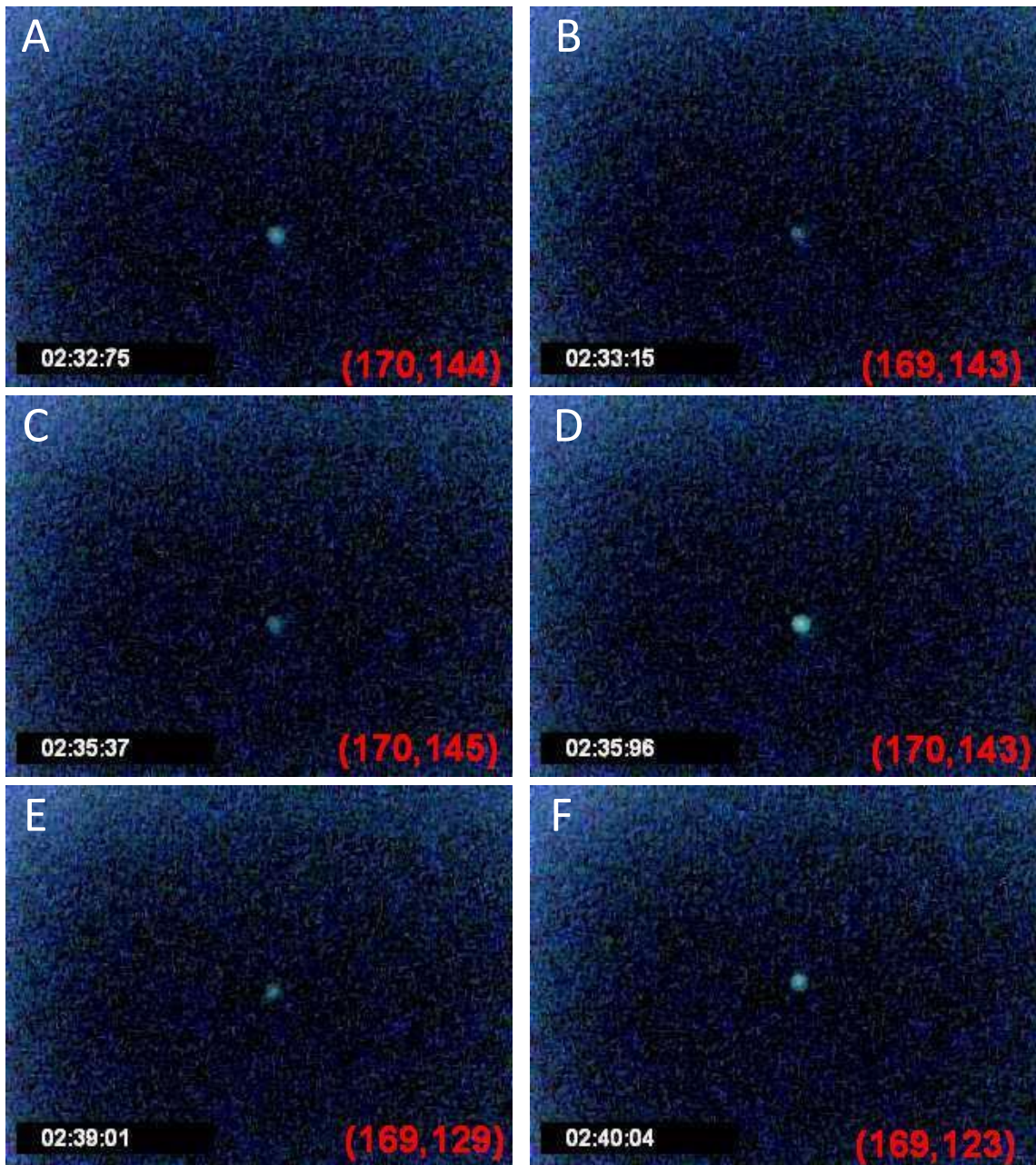
Figure 3-2: Snapshots of a video clip shows visible light emitted during field emission. Time and position of the light spots are shown in the image. The visible light emitting may caused by high temperature or micro-arc discharge.

Our video clip recorded 15 glows in 23 seconds. Each glow lasts about 0.2 second and positions of each glow are different. Therefore, we believe, these glows are corresponding to CNTs which are dominating the emission and destroyed by over-current. Images captured from the video clip are shown in Figure 3-2.

In addition to the CNT emitters, we tested graphene thin film as well. Figure 3-3 shows two SEM images of a graphene thin film. Unlike needle tip shape emitter site, the emission site of graphene emitters is their single atom thick edge. The graphene film is deposited by spray. Like the spin coated CNT film, graphene films do not provide good results in field emission experiments.

CNT field emission cathode based on the abovementioned deposition technology is already available in the market [87] and some devices based on the deposition technology have been demonstrated [88, 89]. But the current density of these products is still quite low [79]. Furthermore, from the experimental results described above, we believe this cathode has some disadvantages that cannot be overcome: i) the height and density of the activated

Figure 3-3: SEM images of graphene thin film deposited on silicon wafer by spray
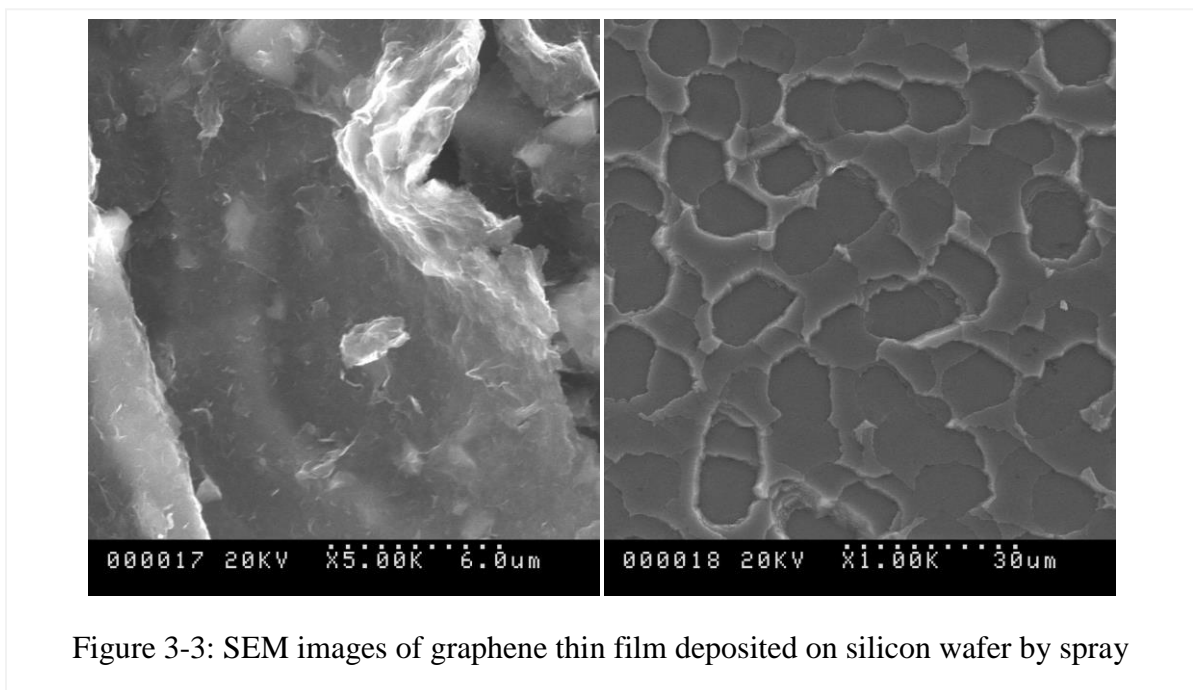
CNT cannot be controlled; ii) ballast resistor is not utilizable in this structure; iii) the emitter does not have an integrated gate, thus the control voltage is high; iv) distance between emission sites is random; and v) the distance from CNT tips to a mesh gate is random, therefore the emission uniformity is poor. These disadvantages cause this cathode requires an over one thousand volt gate voltage to work, and emission current uniformity over a large area is not achievable.

3.2.1.2 Direct Grown Nanotube/Nanowire Field Emitter Array

The other fabrication method of field emitter is directly grown or synthesis nano structures on a substrate. The common fabrication process is CVD or PECVD. Either random or vertically aligned CNTs can be grown [90]. The random CNT film has a similar shape and similar field emission properties to the deposited CNT film discussed above. Both
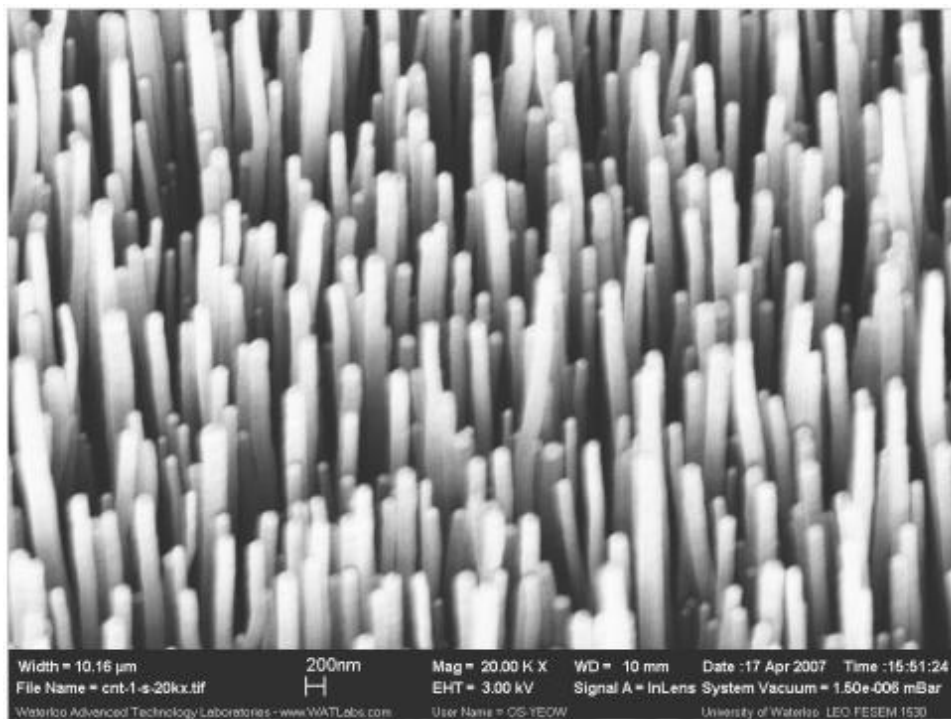
Figure 3-4: SEM image of a high density vertically aligned multi-wall
CNT array. The height and tip diameter is not uniform.
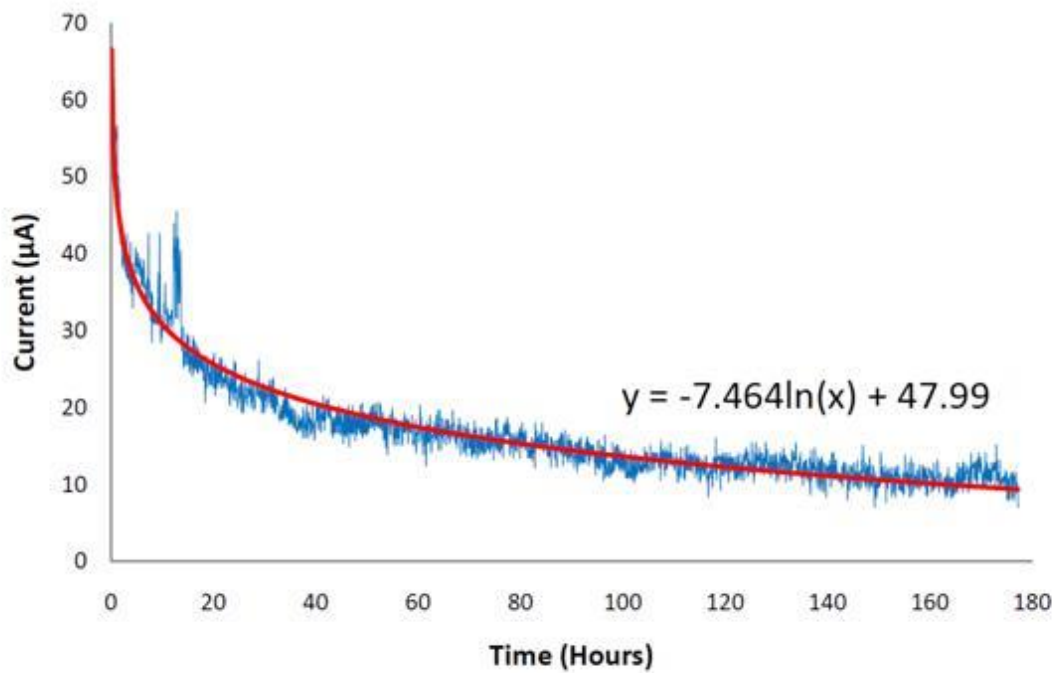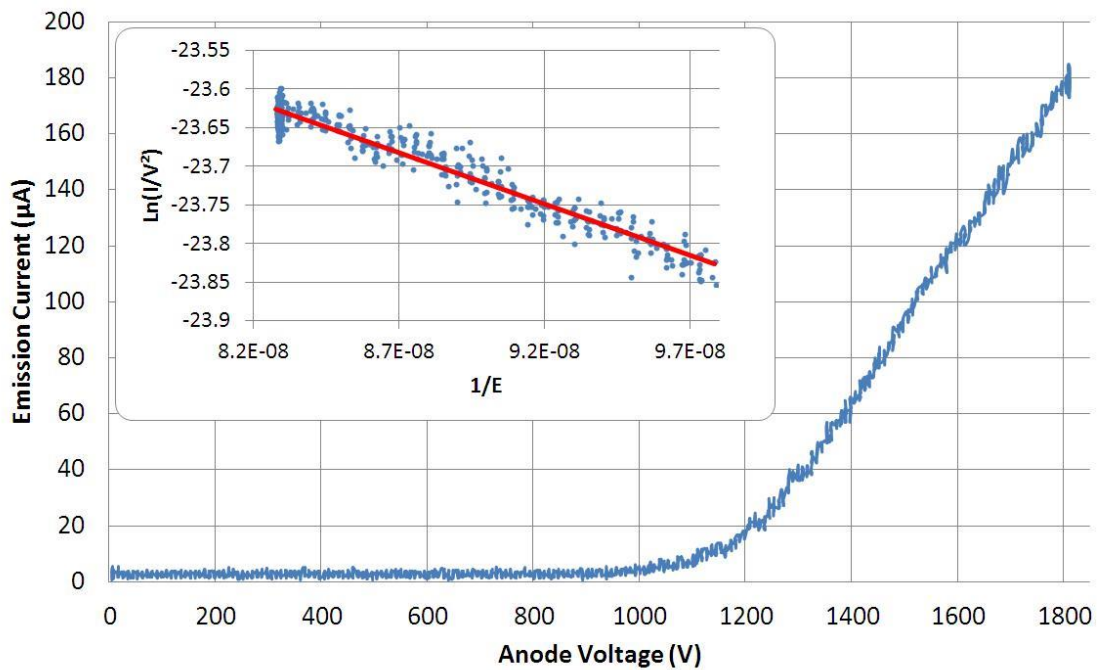
Figure 3-5: Field emission property of high density vertically aligned CNT array grown on silicon wafer. Current versus voltage (upper), Fowler-Nordheim plot (inset), and current versus time curve (lower).
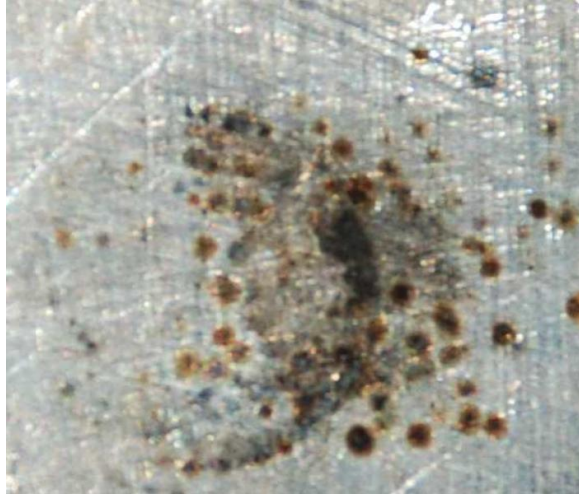
Figure 3-6: Optical image of an aluminum plate used as an
anode of a field emission experiment. Black spots appear
on the anode after a field emission experiment.

single-wall CNT and multi-wall CNT are available in high density form. However, low density CNT, also known as free standing CNT, is only available for multi-wall CNT [91]. Figure 3-4 shows SEM images of high density vertically aligned CNT arrays used in our early experiments. The sample is tested with a diode configuration, in a vacuum chamber with a pressure of 1×10^{-7} Torr. The cathode-anode gap is about 150 micrometer. The area of the CNT array is 0.785 cm². Figure 3-5 shows an emission current versus anode voltage curve, Fowler-Nordheim plot and a long term current versus time curve. Form the Fowler-Nordheim plot, the field enhancement factor β is 7000 and effective emission area is 1.65×10^{-9} m². Due to the complex geometry of the surface of CNT thin film, the field enhancement factor has a big difference with the CNT aspect ratio, which is used to approximate the field enhancement factor in single CNT cases. To calculate the accurate field enhancement factor of such a complex surface, more theoretical studies are needed. After a long term stability experiment, damages of the sample are visible to naked eye. An optical
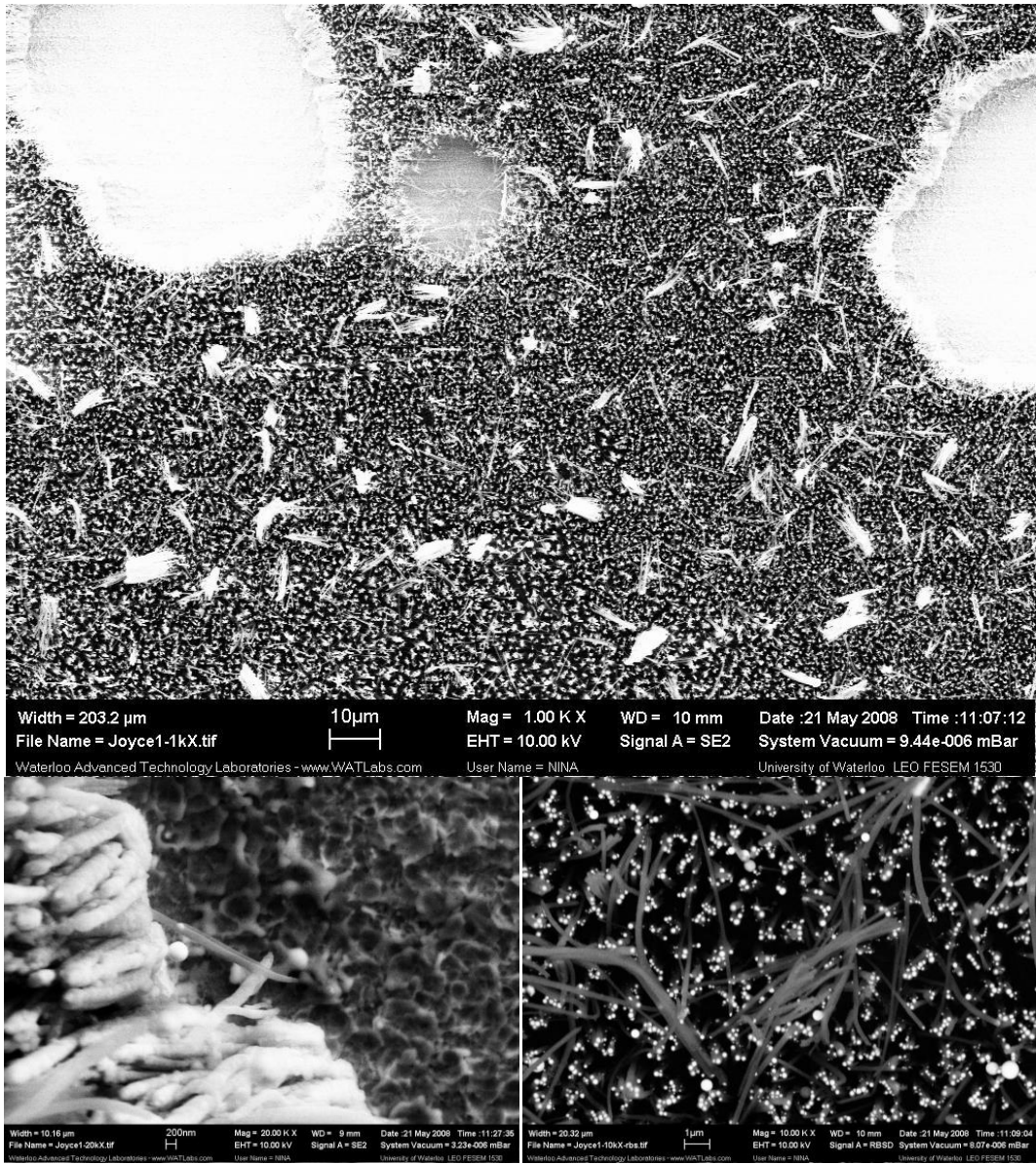
Figure 3-7: SEM images of high density vartically aligned CNT array after field emission experiments. The sample has some defects after the experiments (upper). The defects are visible on bear eyes. There are two kinds of defects: CNT peel off from the substate (lower left) and CNT clustered (lower right)

image of an anode after a field emission experiment is shown in Figure 3-6. The black spots on the anode are traces of entire CNTs or segments of CNTs peeled off from the cathode. The diameter of the largest spot is about 0.7 mm. SEM images of the sample after the experiments are shown in Figure 3-7. The images indicate there are two kinds of damage in the CNT emitter array, i) CNTs are clustered, and ii) CNTs are pulled out from the substrate or removed from the array. These defects indicate the high density CNT array has three major disadvantages, namely i) adhesive of CNT to the substrate is poor, ii) the emission uniformity is poor and just a very small amount CNTs are involved in the emission, and iii) interactions between neighbor CNTs are not negligible and may lead to the emission current degradation. To make a field emitter have a high current and long lifetime, these three problems need to be overcome.

Some other emitters are also tested. Figure 3-8A and 3-8C shows SEM images of low density CNT array and high density ZnO nanowires. After a field emission experiment of a low density CNT array, only a few CNTs left. Figure 3-8B shows CNTs are removed from the substrate and the bases of the CNTs are remained. This result proofs that the vertically aligned CNTs has a poor adhesion to the substrate [79]. On the other hand, FEM image shows a high density ZnO nanowire emitter, which has an area over 100 mm², has just thirteen emission sites activated. This result proofs that the emission uniformity of a high density nano-structure array is poor. In additional to these two problems, the thin film emitters have another disadvantage. To achieve a high switching speed, a gate electrode needs to be placed between the cathode and the anode. Since the top surface of the emitter film is not flat, the gap between the emitter tips to the gate cannot be very small, normally over 100 micrometers, as a result the operate voltage is over several thousand volts.
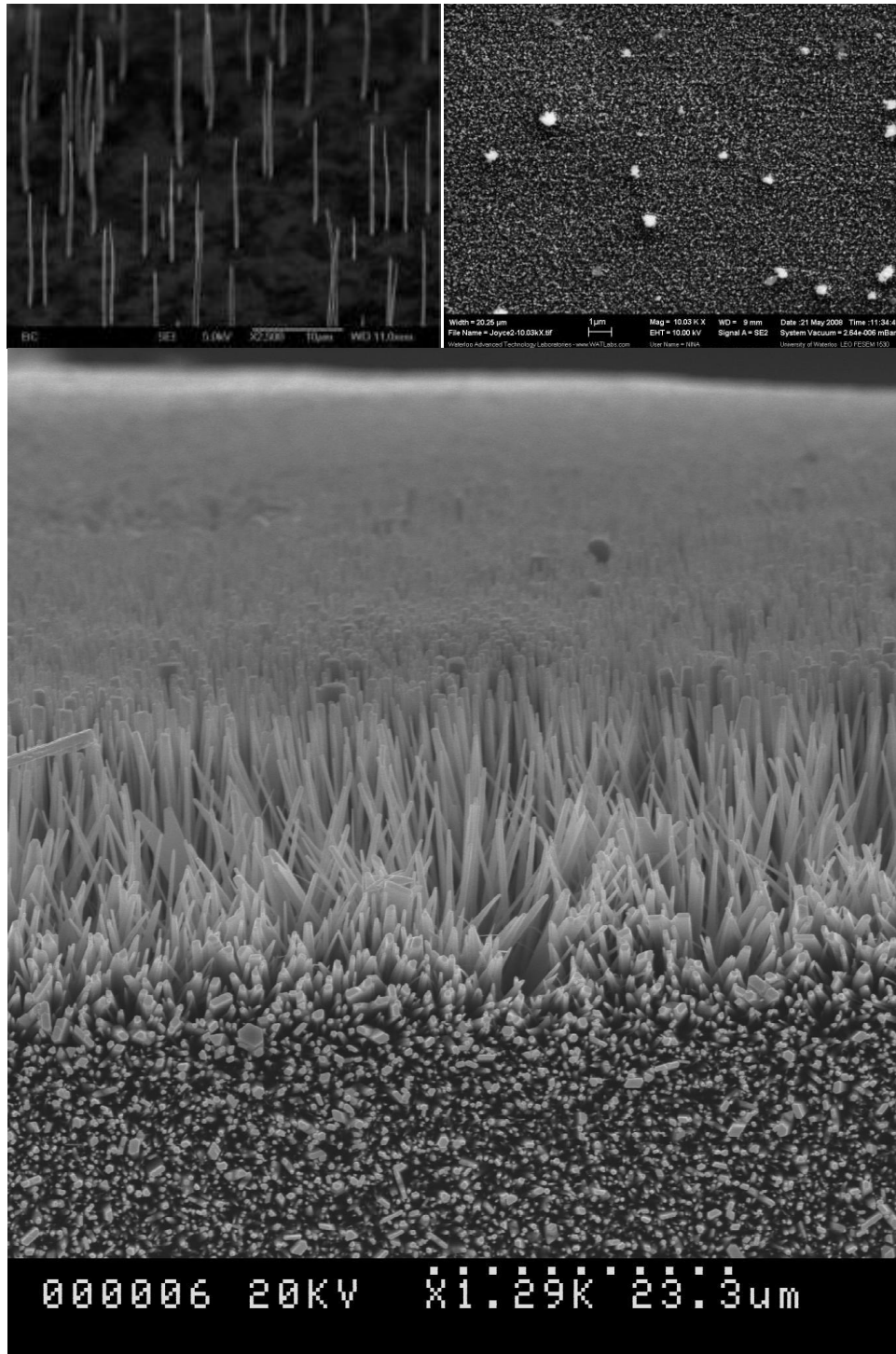
Figure 3-8: SEM images of low density vertically aligned CNT before
field emission (upper left). After field emission (upper right) the CNTs are
removed from the substrate and only catalyst dots are left. SEM images of
ZnO thin film field emitter (lower).

Moreover, the emitter-gate gap is not well controlled. As a result, the emission uniformity over the entire emission area in a triode emitter is even worth than the thin film emitter with a diode configuration.

3.2.2 Gated Field Emission Array

Fast response time is the biggest advantage of field emission cathode over thermionic emission cathode. In some applications, such as field emission display, X-ray beam array, and microwave amplifier, a triode structure is needed to achieve a high switching speed and an addressable emitter array. High emission current, high uniformity and low control voltage are desired as well. Array of field emitter with individual gate structure possesses all the desired properties for these applications.

3.2.2.1 Spindt Cathode

Spindt cathode was first designed in 1968 [41] and successfully commercialized after a ballast resistor layer was employed in 1990 [92]. Each Spindt cathode contains thousands of micrometer scale emitters. Each emitter consists of a hole gate electrode, a cone shape metal emitter, and a ballast resistor. Figure 3-9 shows the structure of a Spindt emitter from ref [93]. Due to its ingenious structure, Spindt cathode has some inherent advantages. First, the gap between emitter tip and gate electrode is smaller than one micron, the control voltage is between 100 V to 300 V, much lower than that of metal needle tip emitters [41]. Second, the transmission efficiency (anode current/cathode current) is higher than 99% [94], makes the total cathode current and Joule heating much lower than that of other emitter. Third, the emitters are fabricated with thin film processes in high vacuum environment, which assure less release gas from substrates. Fourth, the deposition process of the cone shape emitter is self-aligned, thus no nano-lithography is necessary. Fifth, the ballast resistor not only
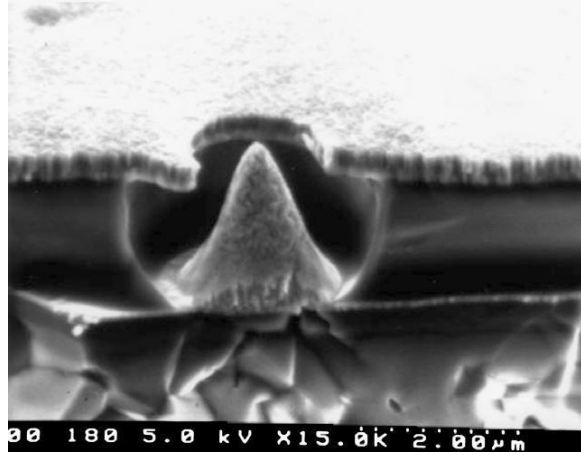
Figure 3-9: SEM image of a typical structure of a Spindt emitter [93]

increases the emission uniformity, and stability, but also makes the device fail-safe [95]. These advantages lead to Spindt emitter shows good performance since it was first designed. From the first Spindt cathode, a 2 mA total emission current was obtained from a 100 emitter array in an area of 0.0625 mm² for over 7,000 hours [43]. It was also indicated that emission sites are just one or a few atoms located on the tip of the emitters. Some records of Spindt cathodes are: largest current from single cone 850 µA [96]; 6 mA from 12 tips [97]; smallest-dimension of tip-to-gate 80 nm; tip density of 10^9 cm^{-2}; and lowest gate voltage of 10 V [44]. A prototype of Spindt cathode based medical X-ray source characteristics is consistent with the requirements for human breast imaging [98]. However, the Spindt cathode is still imperfect in the following two aspects, (i) it needs an ultra-high vacuum to work stably; (ii) the fabrication process is not compatible to the new one dimensional nano structures like nanowires and nanoubes. In briefly, Spindt cathode has an excellent structure, but their material and related fabrication processes need some adjustments to compatible with current 1D nano structures, what can work in medium level vacuum.

3.2.2.2 Gated CNT Field Emission Array

Some attempts have been made to combine the advantages of the Spindt emitter's structure and CNT's material properties [99-104]. In these designs, the original metal cone shape emitters are replaced by CNT emitters. However, the crystal structure and synthesis process of CNT and metal cone have some essentially differences, thus the emitter fabrication process must be changed. There are two methods to fabricate these devices, namely, grown CNTs in gate hole cavities or place round hole shape gate electrode around CNTs. Although these structures have some improvement in the emission performance, their long term stability and lifetime study are still insufficient. Moreover, there are few obvious shortages of such structures and fabrication processes. First, the cone shape metal emitter has the best thermal and mechanical stability, but the CNT have a weak adhesive to the substrate, thus CNT may be over heated or pulled out from the site. Second, the original Spindt process are self-aligned, so the emitter apexes are aligned to the center of the gate holes, but the CNT grown process cannot guarantee the position of CNT apexes are centered to the holes. Third, the uniformity of CNT height is much lower than that of the metal cones. Fourth, the ballast resistor layer is easy to fabricate in Spindt emitters to improve the stability and uniformity, but it has not been utilized in the CNT based emitters. In conclusion, these hybrid emitters combine the advantages of Spindt cathode and CNT emitters, but their structure and fabrication process needs some significant improvements.

3.3 CNT Emitter with Coaxial Cylinder Gate

The Spindt cathode has a near perfect structure and CNT is the best material of field emitter. The design of our field emission cathode tries to combine the advantages of the structure of Spindt cathode and the material properties of CNT. Figure 3-10A, 3-10B, and 3-
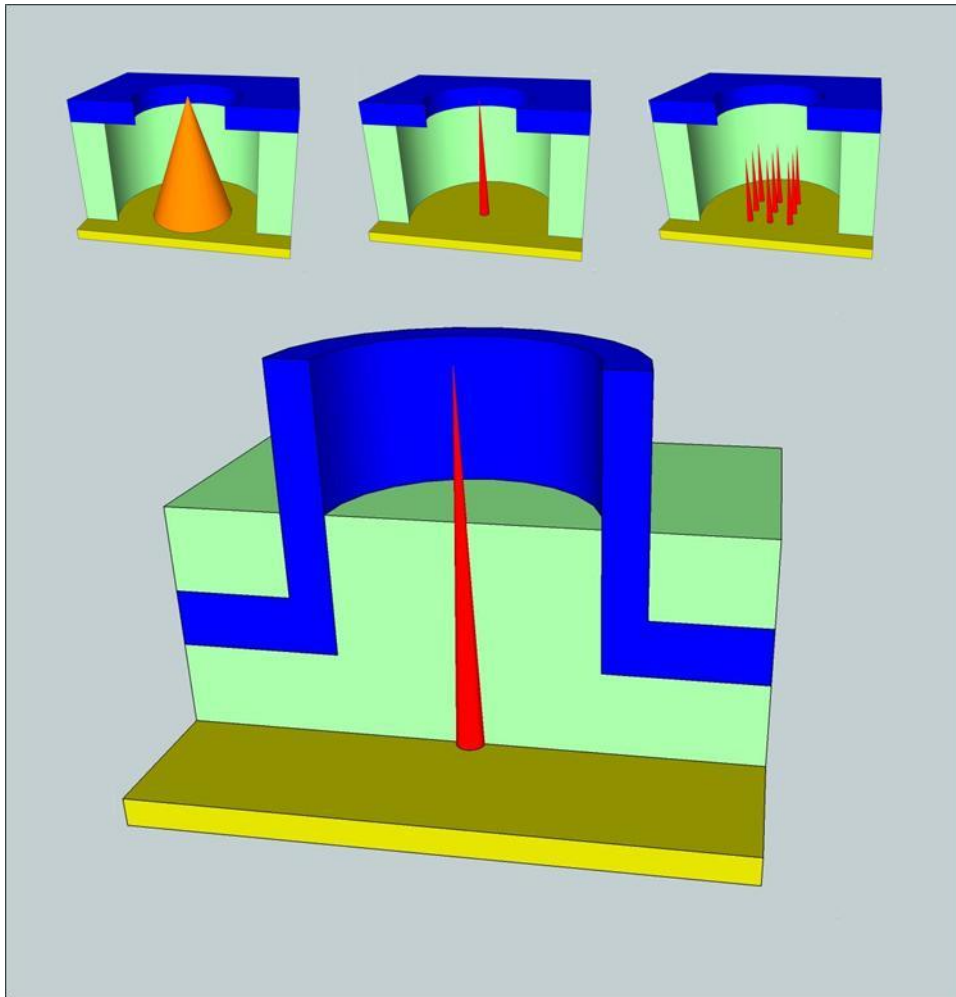
Figure 3-10: Diagrams of Spinde emitter (upper left), gated single CNT
emitter (upper middle), gated CNT cluster (upper right) and new design of
CNT emitter with cylinder shape coaxial gate electrode (lower)

10C show diagrams of the Spindt emitter and gated CNT emitters. In these former
approaches, the gate electrodes, similar to the structure of Spindt cathodes, consists of a flat
metal thin film with holes. Emitters, either an individual CNT or a CNT cluster, are grown in
cavities underneath the holes. Ideally, the emitter tips are desired to locate at the center of the
gate holes and have the same height to the top surface of the gate electrodes. The deposition
process of Spindt emitter is self-aligned, so the metal cone is centered to the gate hole and

has a good uniformity. However, the fabrication process and structure of the metal cone emitter in Spindt cathode and CNT are essentially different. Vertically aligned CNT array can be grown by PECVD [105, 106]. In a well controlled PECVD process, the CNTs are not perfectly straight and the CNT heights follow Gaussian distribution with standard deviations of 6.3% [107]. As a result, if the CNT emitters are grown after the gate hole is formed, the CNT tips may be misaligned to the gate hole center. Thus, the fabrication process of a conventional Spindt cathode is not suitable for a CNT based emission cathode.

To take advantages of the structure of the individual gate electrode, a novel gate structure of CNT emitter array and corresponding fabrication process of CNT emission cathode need to be developed. The new achievement must be self-aligned, self-centered, and highly uniform. The CNT and the top surface of the gate electrode have the same height, and the CNT tips are located at the center of the gate hole. Figure 3-10D shows a diagram of a new designed CNT emitter with a coaxial cylinder shape gate. Considering the essential difference of the synthesis of CNT and metal cone, if the CNT is deposited after the gate cavity and gate hole is fabricated, the alignment of the emitter tip to the gate center is not achievable. Therefore, we designed a fabrication process in an opposite order of the Spindt cathode; namely, the gate electrode is deposited on the cathode with a uniform gap to the emitters. As a result, the CNT emitter and the gate electrode are self-centered. After the gate is deposited, a polish process is utilized to remove the cap on the CNT tip and expose the emitter. This process can cut the CNT and gate electrode to the same height. Therefore, the emitter tip and the top surface of the gate electrode are self-aligned.

3.4 Ballast Resistor for CNT Field Emitter

In a Spindt cathode, the shape and size of the gate holes relies on photolithography, and the shape of the metal cone emitters relies on the size and shape of the holes. Therefore, the shape of the metal cone emitter and size of the gate holes are not perfectly uniform. If an emitter tip is a little bit sharper than other emitters, or a gate hole is slightly smaller than other holes, this emitter has an optimized geometry, and the necessary electrical field to turn-on this emitter is much lower than that of other emitters. As a result, in a Spindt cathode with thousands emitters, a small amount of optimized emitters is active at a low voltage and contribute most of the emission current. Field emission current is exponential to the field strength, therefore, an increase of the voltage cannot active more emitters, and instead, it will attract more current from the optimized emitters. With the increase of the emission current, micro-arc occurs and the emitter tip is destroyed [94]. To overcome the emitter degradation caused by the non-uniformity, a current limiter in serial with individual emitter is utilized [92]. Even through MOSFET has been used as a current limiter [108], ballast resistor underlayer is the simplest and most effective current limit structure. When ballast resistors are in serial with the emitters, voltage drop on the resistors are proportional to the emission currents from corresponding emitters. The high current on preferred emitters lead to a high voltage drop on the resistor, thus both the electrical field strength at the emitter apex and the emission current is reduced; meanwhile, the other emitters have a higher electric field strength and will contribute more emission current. With a proper resistance, this negative feedback process can effectively reduce the emission current of the preferred emitters to a value close to the average level; as a result, the uniformity of the overall emitter array is increased remarkably. In the event of an arc, energy stored in the base-gate capacitor is released to the gate and causes it to melt and splatter, thereby destroying the emitter site or
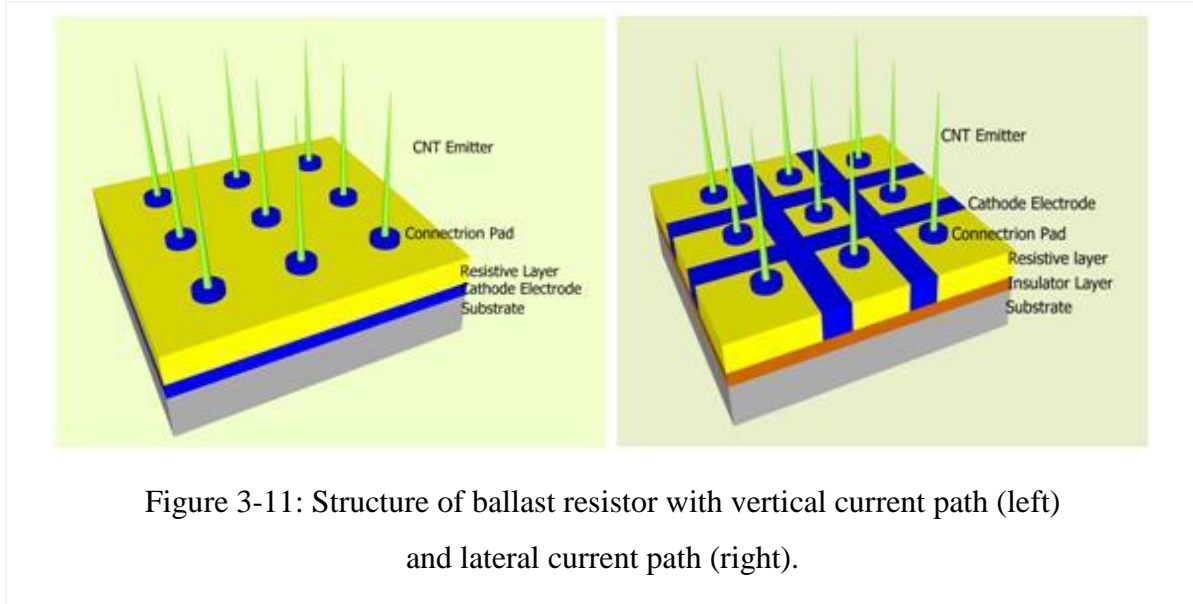
Figure 3-11: Structure of ballast resistor with vertical current path (left)
and lateral current path (right).

even the cathode. A ballast resistor provides a voltage drop in proportion to the emitted current thereby suppresses current runaway and limits damage. In briefly, ballast resistor of Spindt cathode has several benefits [109]. First, it protects the cathode from catastrophic arc damage by limiting the current. Second, it homogenizes the emission across the cathode. Finally, it improves the robustness of the cathode, so it can be turned on without bake-out after exposure to air.

The ballast resistor has two geometries: (i) vertical resistor [92]; and (ii) lateral resistor [110]. Figure 3-11 shows the geometry of these structures. A vertical resistor consists of a resistive polysilicon layer which is sandwiched between a connection pad and a cathode electrode. The resistance can be approximated by $R=\rho*L/A$, where ρ is the resistivity of the material, L is the thickness of the polysilicon layer, and A is the area of the connection pad. On the other hand, a lateral resistor consists of a resistive polysilicon layer, which is sandwiched between a connection pad and an insulation layer. The cathode electrode is placed beside the connection pad, either in or above the polysilicon layer. The current path is lateral from the connection pad to a cathode electrode. In a lateral resistor, the geometry

complexity of the effective area of the polysilicon layer makes calculation and control of the resistance difficult. Furthermore, the structure and fabrication process of the vertical resistor is simpler than that of the lateral resistor. Therefore, we adopt the vertical resistor in our CNT emitter design.

In a vertically aligned CNT array, the stand deviation in heights and tip diameters of individual tubes could be approximate 6.3% and 4.1% [107, 111], which is worse than that of a Spindt cathode. In a CNT emission cathode, the CNT is heated up by Joule heating and the tip is cooled down by Nottingham effect [112]. Temperatures and tensile stresses have been measured [86, 113] and calculated [114, 115], and the structural damage and failure during field emission of individual CNT emitters is also observed [116-119]. When the temperature of a CNT is over 1500 K lights are emitted from emission tips and are visible to bear eyes [86]. Field emission current is an increasing function of temperature [120]. This positive feedback is observed at a temperature above 750 K and the tip temperature can achieve 2000 K [86]. Study shows the apex temperature increase with the emission current and the Fermi level decrease from 0 to -1.4 eV while emission current increase from 0 to 100 nA. Although, in a field emission device, the reasons of emitter failure are complex, it is supported by the experiments and calculations listed above, that, to an individual CNT, the high temperature caused by Joule heating is a main reason of the emitter degrading and failure. The maximum current can be carried by an individual CNT is about 20 μA per tube (SWCNT) [121] and 12 μA per shell (MWCNT) [122]. On the other hand, experimental results show, in field emission, MWCNTs can be shortened [119], or their outer layer can split off [116, 119] at the emission current about 10 μA. This current is close to the maximum current carrying capacity of a single shell of a multi-wall CNT. Since the emission sites are just one or few

atoms located at the apex of the outermost layer, we can assume that the 12 μA saturation current of single shell is the upper limitation of emission current of a CNT without destroys it. In additional to the emitter tip destroy, substrate melting is another problem. In our early experiment (Figure 3-7 and 3-8), CNTs pulled out from the substrate is observed, which is caused by both the weak adhesive between CNT and the substrate, and the Joule heating melt the surrounding area of the CNT base. To avoid an emitter destroy by over current, the suggested safe operating current of individual CNT is 1 μA [119]. Therefore, we adopt a ballast resistor as a current limiter to improve the performance of a CNT emitter array and set 1 μA per emitter as the maximum current value in our design.

One significant difference between the geometry of an emitter in a conventional Spindt cathode and a CNT emitter is the contact area to the underlying layer. In a Spindt emitter, the diameter of the base of the cone is in the scale of sub-micrometer; thus the ballast resistor is easy to realize. However, the connection area of a vertically aligned CNT is in the
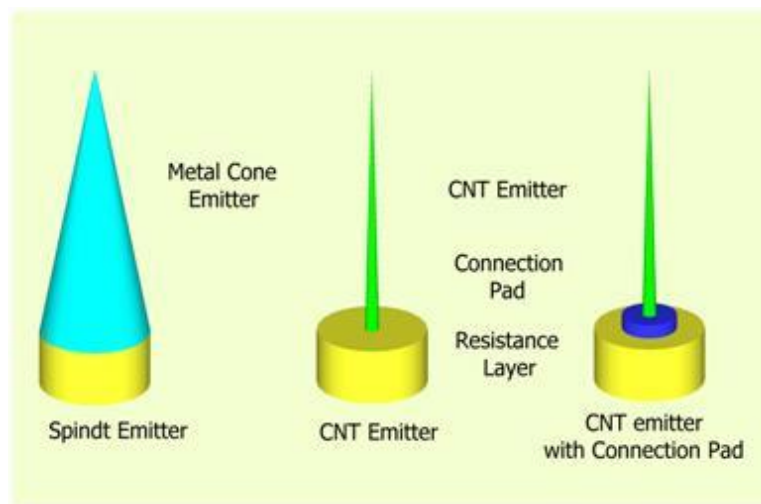
Figure 3-12: Diagram of metal cone in Spindt emitter,
vertically aligned CNT grown on resistance layer, and
vertically aligned CNT with connection pad.

45

order of several tens nanometer and is not controllable [91]. Furthermore, a cone shaped emitter has better mechanical and thermal stability than a narrow cylinder emitter [123] because of larger thermal conductive path. In the case of CNT emitters, the contact point of CNT and substrate can be melted, thus leading to emitter failure [115]. To overcome these problems of CNT emitters, a chrome connection pad is employed. Figure 3-12 shows the structures of a Spindt emitter, a CNT emitter and a CNT emitter with a connection pad. The connection pad has four significant advantages: i) it provides a homogeneous resistance by using a uniform connection area; ii) the metal connection pad has higher thermal conductivity than the polysilicon resistive layer; thus heat can be removed from the contact area faster and emitter failure caused by substrate melting can be avoided; iii) the chrome pad works as buffer layer to avoid the diffusion of CNT catalyst dots into the resistor layer, thereby it avoids a decrease in resistivity and non-uniform catalyst size; and iv) chrome can increase the adhesion of CNT to the underlying layer. This connection pad structure is also
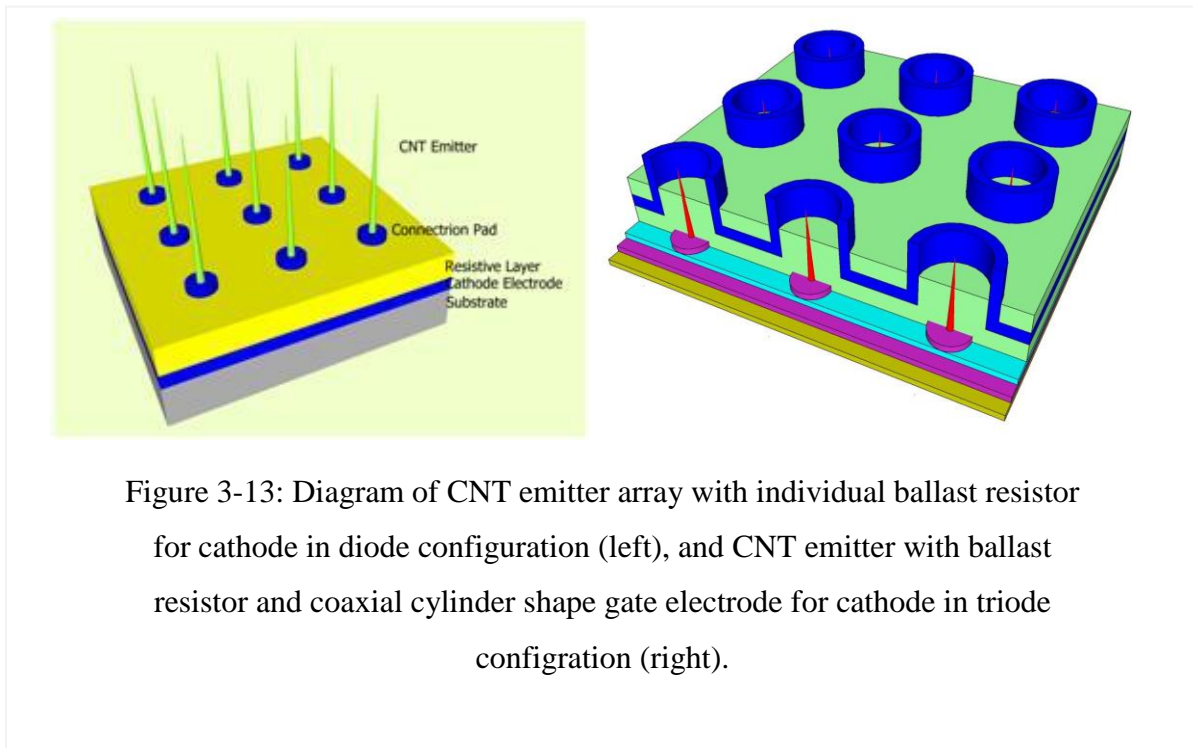
Figure 3-13: Diagram of CNT emitter array with individual ballast resistor for cathode in diode configuration (left), and CNT emitter with ballast resistor and coaxial cylinder shape gate electrode for cathode in triode configration (right).

suitable for gated CNT emitters. Figure 3-13 shows diagrams of A) CNT emitter array with ballast resistors for cathode in diode configuration; and B) CNT emitter array with ballast resistor and coaxial cylinder gate electrode for cathode in triode configuration.

3.5 Chapter Summary

In this chapter, the material of field emitter and structures of field emission cathode are described. Amount the well studied emitter materials and cathode structures, low density vertically aligned CNT array is the best candidate for diode field emission devices, and CNT emitter array with individual gate is the best structure for triode devices. Comparing the difference of the structure and synthesis method between Spindt cathode and CNT array, we design a new coaxial cylinder shape gate electrode for CNT emitter. The fabrication process of the gate electrode is self-centered and self-aligned. Therefore, this design can combine the advantages of the Spindt cathode structure and CNT material. To further improve the performance of the emitters, a new ballast resistor structure is utilized in both diode emitters and gated triode emitters.

Chapter 4
Numerical Simulation of Field Emission Cathode

4.1 Introduction

Low density vertically aligned CNT array is one of the best candidate for field emission cathode. So far PECVD is the only method to produce free standing CNTs [69, 91, 107]. Free standing CNTs are all multi-wall CNTs and have a bamboo structure with a catalyst dot at the tip. The height of these PECVD grown CNTs and their tip diameters follow Gaussian distribution [107]. The stand deviation in heights and tip diameters of individual tubes could be approximate 6.3% and 4.1% [111]. Due to the extreme sensitivity of the Fowler-Nordheim tunneling process to small variation of geometries and physics parameters of emitter tips, active emission site density may be two orders less than the emitter density of the array [124]. Although CNT emitters have been simulated in 2D for many times, 3D simulations are still rare. Furthermore, 3D simulation result shows some effects have been grossly underestimated. For example, 2D simulation results show when an inter-tube distance over twice the CNT height, the screen effect are negligible [125], but in 3D simulation, the result is five times the CNT height [126].

In this chapter, we use 3D models to evaluate the effects of the parameters of a low density vertically aligned CNT array and a CNT emitter with a coaxial cylinder gate. Optimized values of the critical parameters are calculated, such as: CNT inter-tube gap, thickness of insulation layer, and resistance of the ballast resistor. Even through Fowler-Nordheim theory and classic electromagnetism have some inaccuracy in calculating the nanometer scale objects, they are still the most widely accepted simulation methods [33].

4.2 Field Emission non-Uniformity of an Emitter Array

To calculate the effects of the electric field shielding between CNT emitters, the electrical field strength of individual CNT was simulated by a 3D finite element method. CNTs are simulated using a cylinder with a hemispherical cap in a diode configuration. Figure 4-1A shows a cross section of the simulation model, and Figure 4-1B shows a simulation model of a 3x3 emitter array. A value of height H = 5µm and radius r =50 nm are set as reference sizes. Vertically aligned CNTs with uniform height *H* and radius *r* are placed on a flat substrate. To balance the effect of the screening and emitter density [125],

Figure 4-1: Diagram of simulation models: A. cross section of the simulation model; B. simulation model of CNT emitter in the center of emitter array; C. CNT on an edge of an emitter array; D. CNT at a corner of an emitter array; and E. single CNT not in an array.
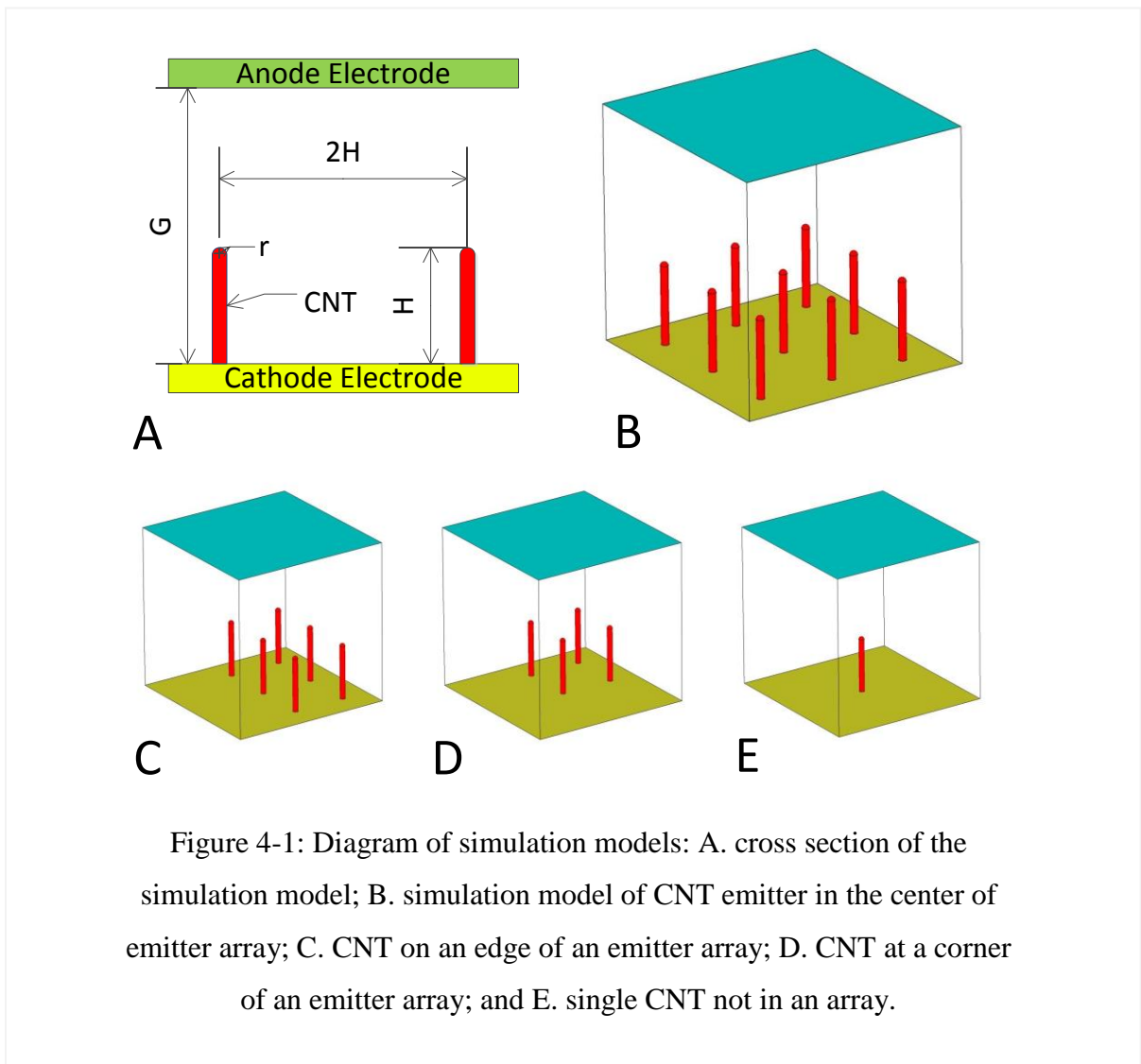
the inter-tube distance of the array is 10 μm, which is equal to twice the CNT height. In a plasma-enhanced chemical vapor deposition (PECVD) grown CNT array, the standard deviation in height and diameter of individual tubes could be approximate to be 6.3% and 4.1% [111]. We set the electric field strength of the center CNT tip as the reference value, when all the CNTs have the height and diameter equal to $H = 5\ \mu m$ and $r = 50\ nm$. Then, we keep the height and diameters of the surrounding CNTs unchanged, and just change the height and diameter of the center CNT. The local electric field strength at the center CNT tip with different height and diameter is calculated. The relationship between emission current density and local field strength can be described by a simplified Fowler-Nordheim (F-N) equation

$$J_{FN} = 1.56 \times 10^{-10} \frac{F_L^2}{\varphi}\ exp\left(-6.83 \times 10^9 \frac{\varphi^{3/2}}{F_L}\right) \tag{4.1}$$

where F_L is the local field strength at the CNT tip. Strength of the far-field F_F equals to the anode potential U divided by anode-cathode gap G, and the field enhancement factor β can be obtained by divide the local field F_L by far-field F_F. Emission current from the CNT can be calculated by $I=JA$, where A is the area of emission site, can be approximated by r^2, where r is the radius of the emitter tip apex [127]. Table 4-1 shows the normalized field strength and emission current of CNTs with different heights, diameters, and locations (row No. 3 is used as reference value). When the center CNT is 6% higher and 4% thinner than the reference size, the local field strength at the tip is 7% higher than the reference value. When the center CNT is 6% lower and 4% thicker than the reference size, the local field strength at the tip is 8% lower than the reference value. As a result, the non-uniformity of the CNT geometry can lead to a 15% variation of the local electrical field strength. The field enhancement factor of an emitter is equal to the local field strength divided by far-field

Table 4-1: normalized field strength and emission current of
CNT with different height, diameter, and location

CNT Location	No.	Height	Diameter	Local Field	Emission Current
Center of Array	1	94%	104%	92%	78%
	2	106%	104%	101%	114%
	3	100%	100%	100%	100%
	4	94%	96%	97%	83%
	5	106%	96%	107%	119%
Edge of Array	6	94%	104%	94%	84%
	7	100%	100%	100%	101%
	8	104%	96%	110%	135%
Corner of Array	9	94%	104%	95%	86%
	10	100%	100%	104%	117%
	11	104%	96%	112%	142%
Single CNT	12	100%	100%	109%	141%

strength, which is equal to the applied voltage divided by anode-cathode gap. Thus, a 15%

change in field strength reflects the field enhancement factor has a 15% variation. Due to the

extremely sensitivity of the emission current density to the local field strength, the 15%

variation of the field strength can lead to a 41% emission current variation (current difference

between row No.5 and row No.1 in Table 4-1). In addition of the effects of the variation of

the height and diameter, the effect of the location of a CNT is also simulated. We use four

different models to simulate i) a CNT at a cornet of an array (Figure 4-1B), ii) a CNT on an

edge of an array (Figure 4-1C), iii) a CNT at the center of an array (Figure 4-1D), and iv) a

single CNT (Figure 4-1E). When using the field strength and emission current of a centered

CNT as a reference value (row No. 3), and consider the variation of the CNT height and

diameter, the emission current of a thick and short CNT at the center of an array is 64%

lower than a high and thin CNT at a corner. These results indicate that the geometry and

location of a CNT affect its emission current significantly. The non-uniformity of a CNT array leads to a poor emission current uniformity.

4.3 Effect of a Ballast Resistor

4.3.1 Ballast Resistor for Single CNT

By employing a ballast resistor, the applied voltage is divided by the ballast resistor and transimpedance. The relationship between emission current I and applied voltage U can be approximated by a modified F-N equation. Figure 4-2 shows the electric field strength along the CNT axis is concentrated at the CNT tip. The far field (electric field strength over 10 times the emitter height from the cathode) is homogeneous and has a value that is close to the anode potential U divided by the anode-cathode gap G. From this simulation result, we choose 10 times the emitter height as a threshold to calculate the local field strength. As a

Figure 4-2: Simulation result of electric field strength distribution along the axis of individual CNT emitter. Electric field strength over 10 times the emitter height from the cathode is homogeneous.
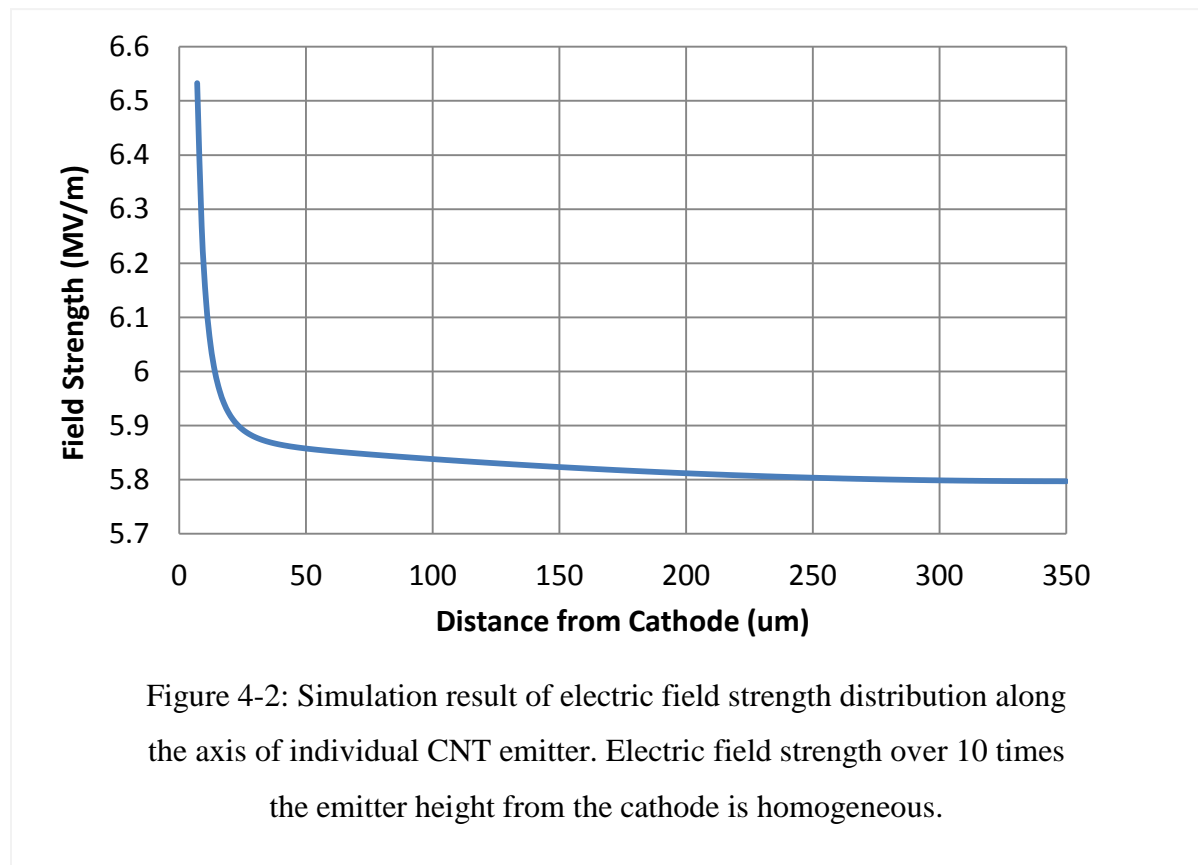
result, two equations are used to approximate the relationship between the emission current I and resistance R for different cathode-anode gap

$$I = r^2 1.56 \times 10^{-10} \frac{\left(\beta\left(\frac{U-IR}{G}\right)\right)^2}{\varphi} exp\left(-6.83 \times 10^9 \frac{\varphi^{\frac{3}{2}}}{\beta\left(\frac{U-IR}{G}\right)}\right) \tag{4.2}$$

$$I = r^2 1.56 \times 10^{-10} \frac{\left(\beta\left(\frac{U}{G}-\frac{IR}{10\times H}\right)\right)^2}{\varphi} exp\left(-6.83 \times 10^9 \frac{\varphi^{\frac{3}{2}}}{\beta\left(\frac{U}{G}-\frac{IR}{10\times H}\right)}\right) \tag{4.3}$$

where r is emitter radius, β is field enhancement factor, R is the resistance of the ballast resistor, G is anode-cathode gap, and H is the height of the emitter. The equation (4.2) and (4.3) are used for the situation that the cathode-anode gap smaller and bigger than 10 times the emitter height respectively. Under a given condition, namely, fixed anode potential and anode-cathode distance, by solving equation (4.2) or equation (4.3), the relationship between resistance, field enhancement factor, and emission current from an individual CNT can be found. When cathode-anode gap is smaller than ten times the CNT height, the solution curves of the equation 4.2 are shown in Figure 4-3. Equations of the trend lines of the curve of 0 MΩ, 50 MΩ and 100 MΩ are also shown in the figures as well. An emitter with no ballast resistor and subjected to a field enhancement factor (100%) that induces 4 µA current is chosen as a reference. In Figure 4-3A the curve of emitter without resistor shows that the emission current changes from less than 2 µA to about 8 µA when the field enhancement factor increases from 80% to 120% of the reference. By connecting a 100 MΩ resistor in serial, the current changes from 1.03 µA to 2.57 µA. In its trend line equation, the quadratic term coefficient is negative, thus the increasing of emission current with the increasing of the field enhancement factor is slower than the ones with smaller value of resistors. In addition, Figure 4-3B shows the effect of the resistor in a large variation range of field enhancement factor. In particularly, the field enhancement factor of an emitter is affected by many
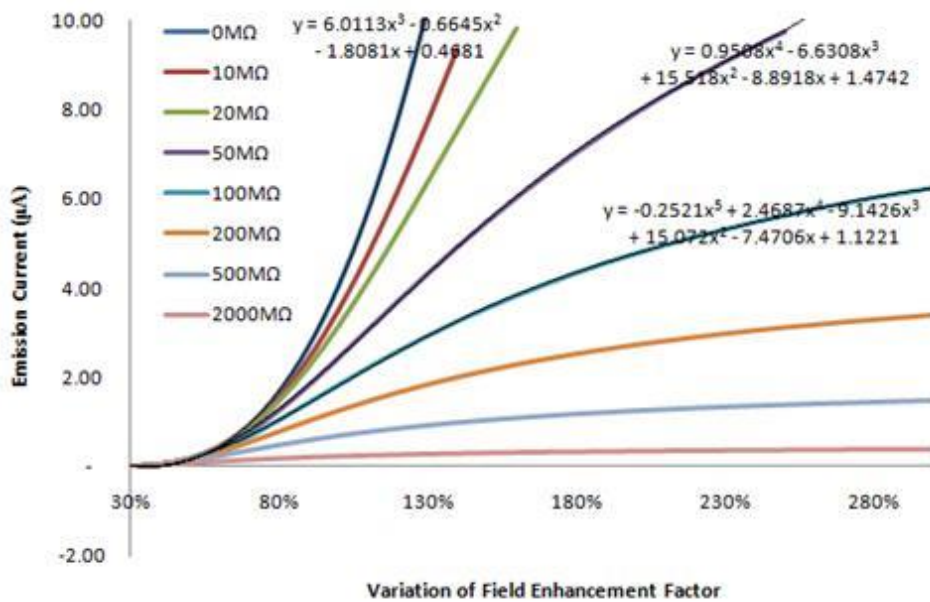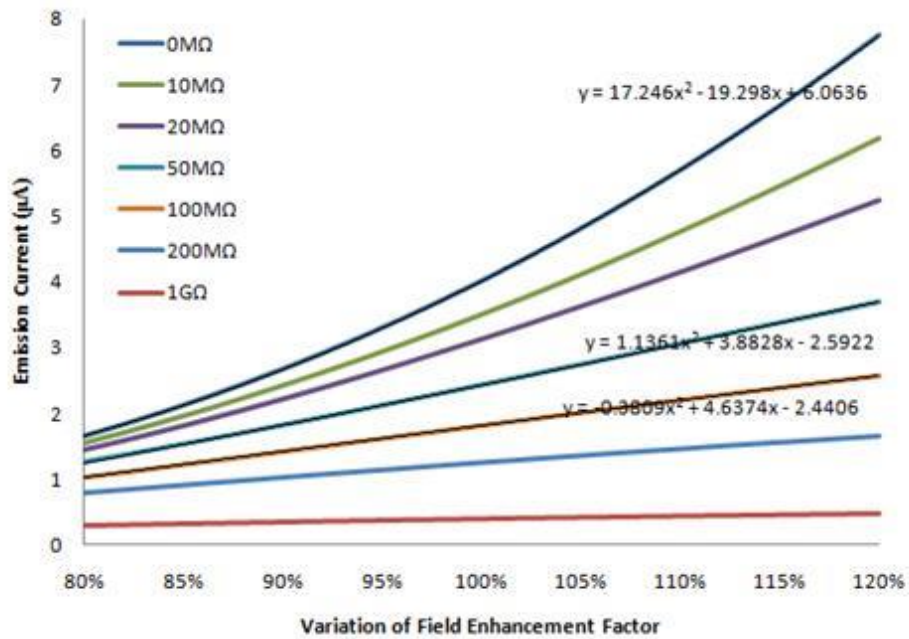
Figure 4-3: Simulation result of emission current versus field enhancement factor shows the effect of the ballast resistor on an individual CNT emitter. With a resistance between 50 MΩ and 100 MΩ, a ballast resistor can effectively limit the emission current of the optimized emitters

uncertainties, not only the geometry and location, but also many other factors such as residual gas and contamination. In these cases, one or few emitters in the array dominate the emission property, and a few atoms at the apex dominate the emitter. A big variation of field enhancement factor occurs and a discharge or micro-arc may destroy the device. Figure 4-3 shows without a resistor, by increasing the field enhancement factor to 130%, an emission current over 10 µA may occur, which is close to the maximum emission current of single CNT. But by import a resistor of 100 MΩ, the emitter can withstand an increase of over 300%. Thus, the resistors are function as fail-safe protectors.

In some applications, for example flat panel X-ray source, a high anode voltage is required, therefore the cathode-anode gap is at least several millimeters (over one thousand times the CNT height). In this case, equation (4.3) is used to evaluate the effect of the ballast resistor. Figure 4-4 shows the calculation result of equation (4.3). The field enhancement
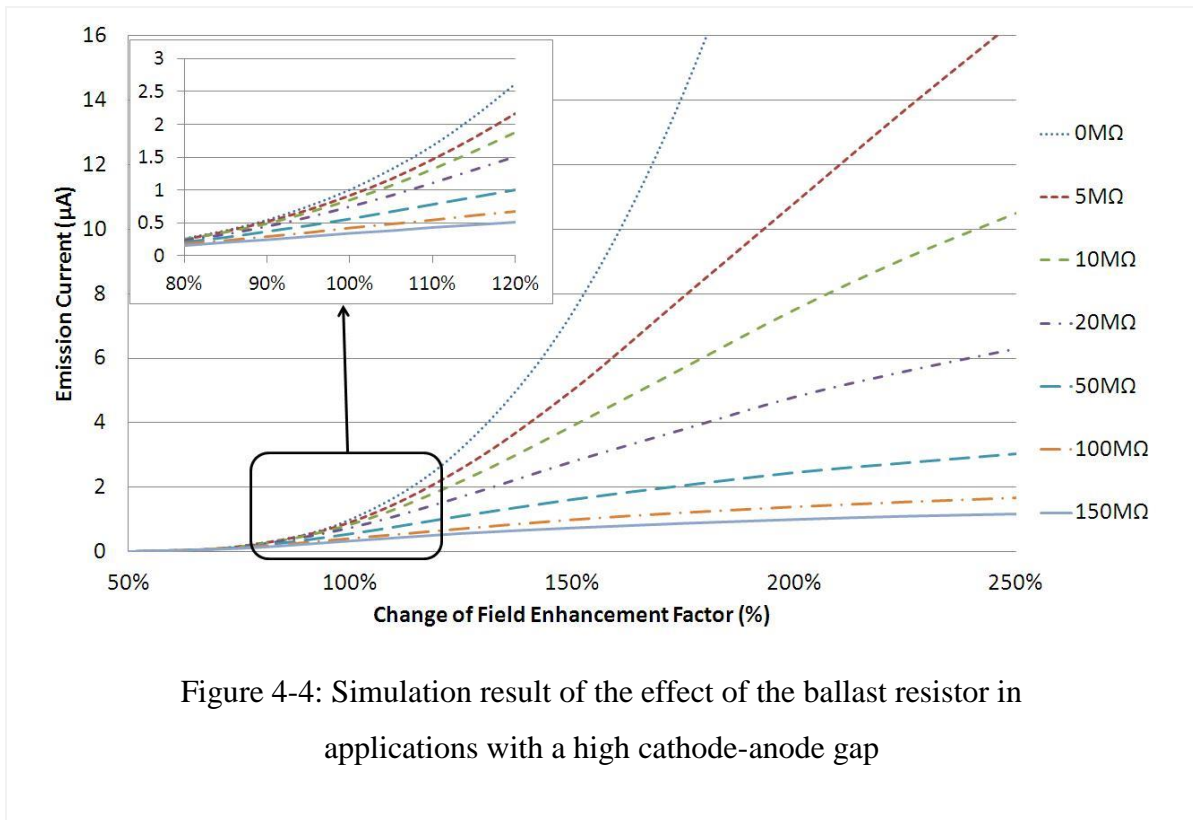
Figure 4-4: Simulation result of the effect of the ballast resistor in applications with a high cathode-anode gap

factor of an emitter without a ballast resistor which emits 1 µA current is set as a reference. Inset of Figure 4-4 shows, with a variation of ± 20% of field enhancement factor, the emission current has a change of 1003% (from 0.26µA to 2.61 µA). However when a 50 MΩ resistor is applied, the change of emission current is 476% (from 0.21 µA to 1 µA). As a result, the ballast resistor effectively reduces the emission current variation (from 1003% to 476%) caused by the emitter geometrical non-uniformity and increases the emission uniformity. Besides the geometrical non-uniformity, other factors may also affect the emission current. For example, gas molecules adsorbed on the emitter surface can change the local work function and lead to a significant emission current change. Furthermore, a positive ion bombardment during a field emission can make the surface rough or shorten the CNT, which lead to an emission current change as well. All this factors lead to a change of the field enhancement factor. An extreme condition with a 200% change of field enhancement factor is calculated, and the result is shown in Figure 4-4. The slope of the curves decreases with the increase of the resistance. As a result, the ballast resistor significantly reduced emission current non-uniformity. For example, without a ballast resistor, when the field enhancement factor increases by 80%, the emission current increases from 1 µA to 15.8 µA and the emitter will be destroyed. When a ballast resistor is employed, the emission current of an emitter, whose field enhancement factor is equal to the reference value, decreases from 1 µA (without resistor) to 0.01 µA (with a 50 MΩ resistor). However, the current changes only 3.02 µA (from 0.01 µA to 3.03 µA), when the field enhancement factor changes 200%. This result indicates the expense of a better uniformity is the decrease of total emission current. Higher resistance provides better emission uniformity but leads to lower total emission current and higher energy consumption. The optimization of the resistance is a trade-off between

performance (emission current) and stability (emission uniformity). We choose the resistance between 50 MΩ to 100 MΩ as an optimized value.

4.3.2 Ballast Resistor in an Emission Array

In addition to the above simulation of single CNT emitter, the effect of the resistor in an array is also simulated. To simplify the calculation, a 2D model is used. In our diode X-ray tube design, the cathode-target gap is 7mm and the voltage is up to 40 kV. The emitter is 5 um in height and 100 nm in diameter. Since the emitter height is smaller than 1/1000 of the cathode-target gap, a simulation with the actual cathode-target gap dimension is very difficult. Thus we set the cathode-anode gap to 100 um and the anode potential to 600 V to

Figure 4-5: Simulation model of a ballasted CNT in an emitter array (upper), simulation results (lower) show potential difference between the connection pad and surrounding area changes the electric field strength at the emitter tip significantly.
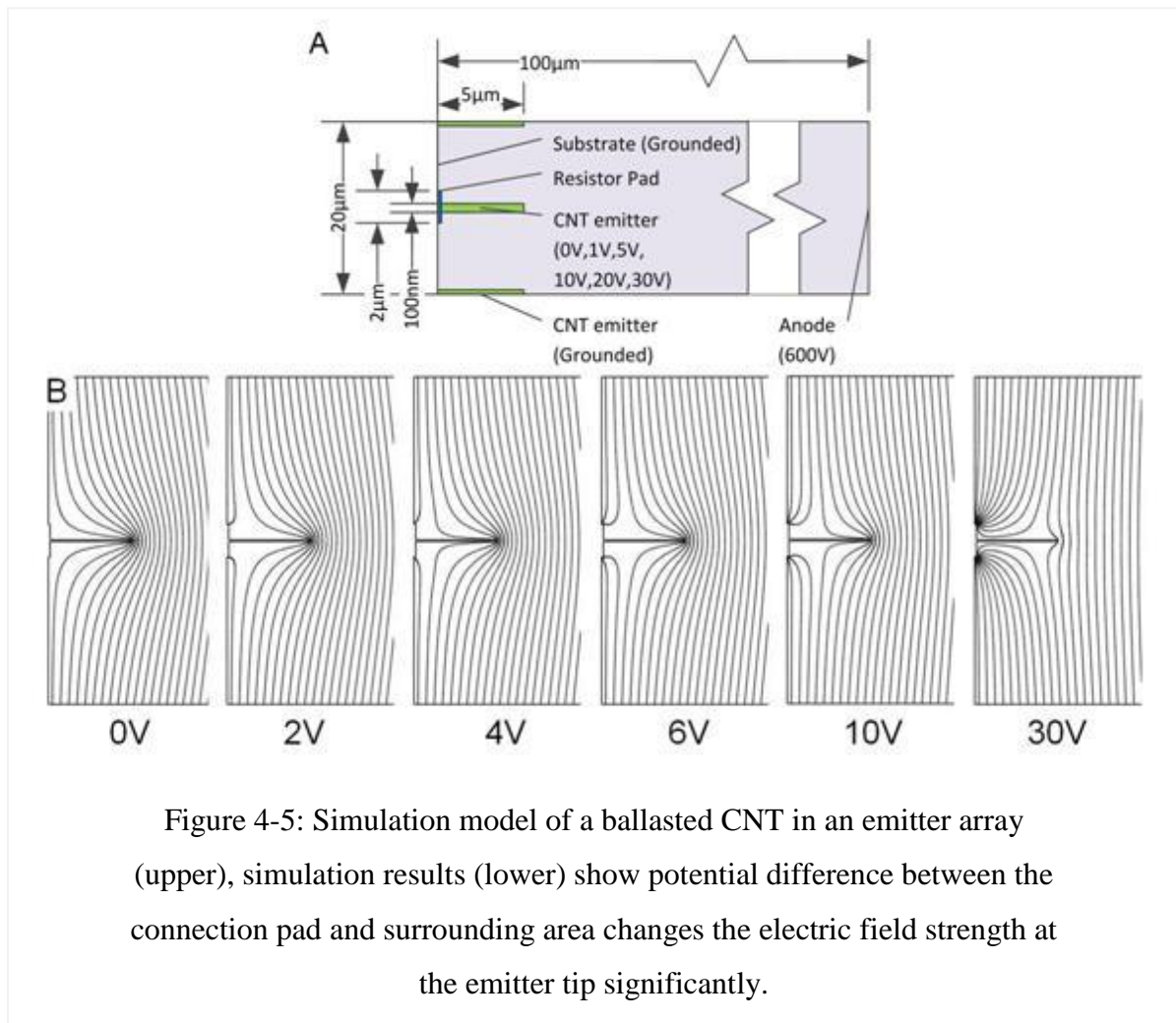
simplify the simulation model. The far field of the model is 6×10^4 V/cm, which is almost the same with that of our experimental setup (40 kV/7 mm=5.71×10^4 V/cm). As the far field strength remains unchanged, this simplification will not affect the local field at CNT tips. Figure 4-5A shows the dimension of the simulation model. We can assume the CNT tip potential equals to the voltage drop on the resistor considering the resistance of the CNT (several kilo-ohms) is much smaller than that of the resistor. The equi-potential lines of a single CNT emitter are shown in Figure 4-5B. Figure 4-5B also shows the electric field strength distribution around the CNT emitter is significantly affected by the potential difference between the CNT emitter and the substrate. We already know that an increase in emitted current from the CNT will increase the voltage drop on the resistor (equals to the resistance times the emission current). However, the increase in the CNT tip potential will cause the decrease in the field strength around CNT tip. For example, when the CNT tip potential equals 0V, 2V, 4V, 6V, and 10V, the field strengths at the CNT tip is 5.23×10^7 V/cm, 5.01×10^7 V/cm, 4.79×10^7 V/cm, 4.56×10^7 V/cm, and 4.12×10^7 V/cm respectively. So, when the CNT tip potential increases from 0 V to 2 V (0.33% of 600 V anode potential), the field strength decreases over 4.2% (from 5.23×10^7 V/cm to 5.01×10^7 V/cm). From the above equation (4.3), this 4.2% field strength decrease can lead to an over 15% emission current decrease due to the extreme sensitivity of the emission current to the field strength. In brief, a 25 nA increase in current brings on a 2 V potential change at the emitter tip, which leads to a 4.2% field strength change and eventually 15% emission current decrease. Consequently, the increase in emission current gets a negative feedback in the system thus produces a relatively stable emission current. In conclusion, the ballast resistor improves the stability and uniformity of emission current.

4.3.3 Ballast Resistor in a Cylinder Gated Emitter

The structure of a gated CNT emitter array is different from the emitter described above. The resistor layer is covered by an insulator layer, thus it do not affect the electrical field distribution. The emitter is simulated with a 2D axial symmetry model. The model diagram is shown in Figure 4-6 A and 4-6B. In this model, the CNT tip and gate electrode is 200 nm higher than the cathode surface. The CNT tip and gate electrode has the same height.
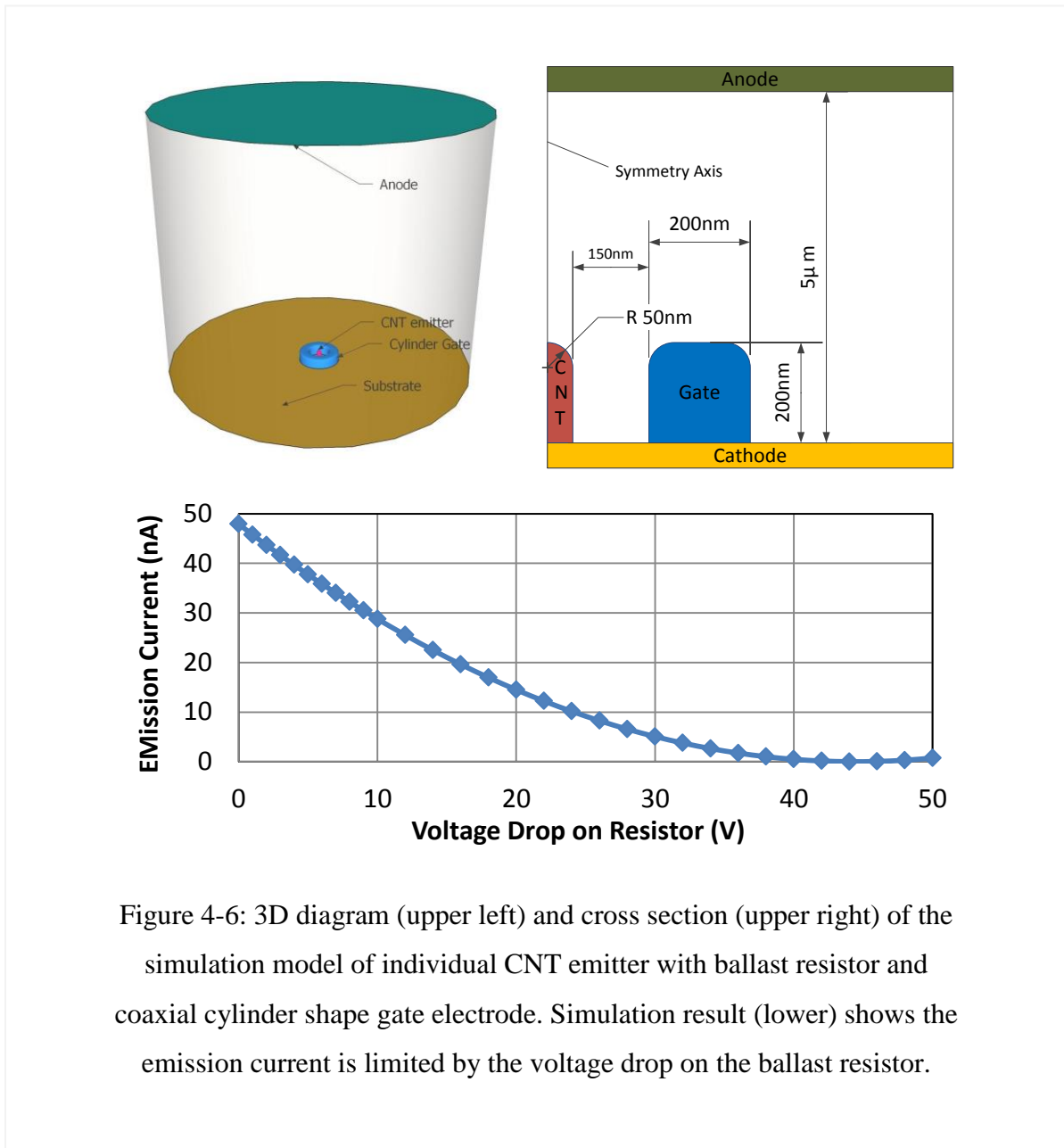
Figure 4-6: 3D diagram (upper left) and cross section (upper right) of the simulation model of individual CNT emitter with ballast resistor and coaxial cylinder shape gate electrode. Simulation result (lower) shows the emission current is limited by the voltage drop on the ballast resistor.

The gap between the side wall of CNT emitter and the gate is 175 nm. By applying a 50 V and 100 V voltages on the gate and anode respectively, the field strength at the emitter tip is 1.71×10^9 V/m. The electric field strength at the side wall is 9.71×10^8 V/m, just 57% of the field strength at the emitter apex. Therefore, the emission current from the CNT apex is dominating and the emission current from the side wall is negligible.

The effect of the ballast resistor is calculated by changing voltage drop on the ballast resistor. The field strength and emission current is then calculated with equation 4.1. An emission current versus voltage drop curve is shown in Figure 4-6C. As described above, the optimized resistance of the ballast resistor is 50 MΩ to 100 MΩ. We use a 100 MΩ resistor here for the calculation. When the emission current is 100 nA, the potential between the gate and CNT is 40V, and the corresponding field strength is 1.37×10^9 V/m. The current decreases to 39 nA, and causes the voltage drop on the resistor decreased. Then the emission current increases to 52 nA, and finally stabilized at about 50 nA. When the voltage of the emitter tip increases to 43 V, the emission current is decreased to 1% of the emission current of a CNT emitter without a ballast resistor. If the resistance is 100 MΩ, the corresponding emission current is 430 nA. This negative feedback feature can stabilize the emission current, and "shut down" the emitter when the current is higher than a safety level. The resistor is connected to the bottom of the emitter directly, thus, the delay of the wire is navigable. This direct connection gives the ballast resistor a very fast response. Therefore, the emitter has a fail-safe feature.

Due to the Fowler-Nordheim equation underestimates the emission current; the above simulation result can only qualitatively describe the field emission properties and the effects of the ballast resistors. The theoretical simulation results need to be experimentally proved.

4.4 Resistance and Dimension of Ballast Resistor

The resistance of the ballast resistor can be simply estimated by Pouillet's Law $R = \rho \dfrac{l}{\pi \, r_R{}^2}$, where R is the electrical resistance of a uniform specimen of the material, ρ is the electrical resistivity of the resistance material, l is the thickness of the material, r_R is the radius of the connection pad of the ballast resistor. The optimized resistance of the ballast resistor is between 50 MΩ and 100 MΩ. If the silicon resistance layer has a thickness of 500 nm, and the radius of the metal connection pad is 1μm, the resistance calculated by Pouillet's law is 101 MΩ. Due the tiny size of the connection pad, the resistance cannot be measured by a simple way. To get an accurate value, the resistance is simulated by a 2D axial symmetry model. Figure 4-7 shows the simulation model. The bottom electrode is ground, the top connection pad is set as a floating potential with a total current of 1 μA. The simulated result shows that the voltage of the connection pad is 67 V, when the emission current is 1μA. The
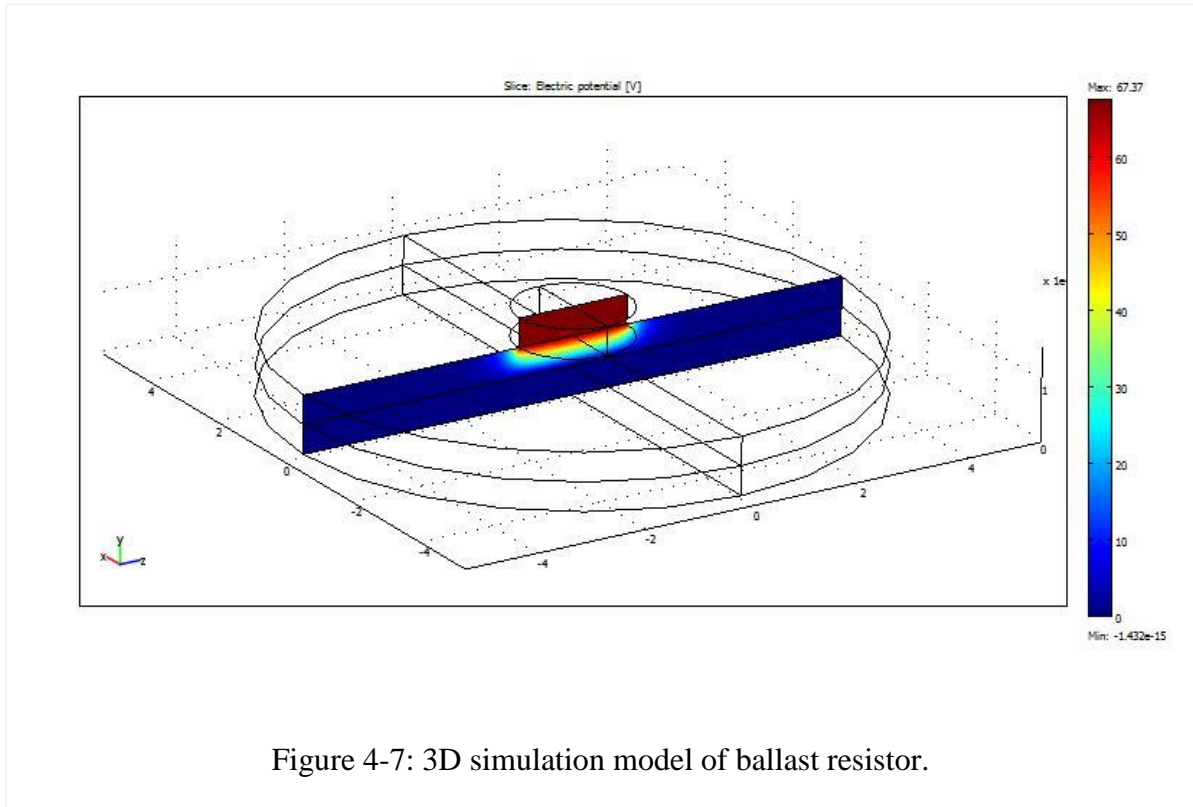
Figure 4-7: 3D simulation model of ballast resistor.

average electric field strength over the resistance layer is 1.34×10^8 V/m. Breakdown field of silicon is 3×10^7 V/m. When the electric field strength inside the resistance layer achieves the breakdown value, the quantity of electron-hole pair increases and, in an extreme condition, impact ionization or avalanche breakdown occurs. This increase of charge carrier leads to the decrease of both the resistance and the voltage drop on the resistor. As a result, the resistor layer is not functional at this field strength. The electric field equals to the resistivity times the current density ($E = \rho J$). By increasing the diameter and thickness of the resistor, the current density inside the resistor is lowered. Simulation results indicates, for a ballast resistor with a thickness of 2.5 μm silicon resistance layer, and 1.8 μm radius, the resistance is 63 MΩ. At an emission current of 1 μA per CNT, the voltage drop is 63 V, thus, the electric field strength is 2.5×10^7 V/m, which is lower than the breakdown filed of silicon. These parameters make the ballast resistor can withstand an emission current of 1 μA, the suggested maximum current of individual CNT [119].

4.5 Efficiency of Coaxial Cylinder Gate

A cylinder gated CNT emitter consists of a vertically aligned CNT inner conductor as the emitter, a conformal insulator layer coated on the CNT; and a cylinder shape gate electrode which is coaxial to the CNT emitter. The emitter and the gate are well integrated on the substrate as a cathode component, and an anode electrode with a several kilo-volts high voltage is placed several millimeters apart from the cathode. The CNT emitter, coaxial gate and high voltage anode forms a triode X-ray tube. Compare to previous designs [99, 100, 102, 128], this structure has two significant advantages. First, the CNT emitter is firmly fixed in the cylinder shape insulation layer and gate electrode, therefore, the emitter pull out caused by substrate melting is avoided. Second, the coaxial structure is axial symmetric, thus, the
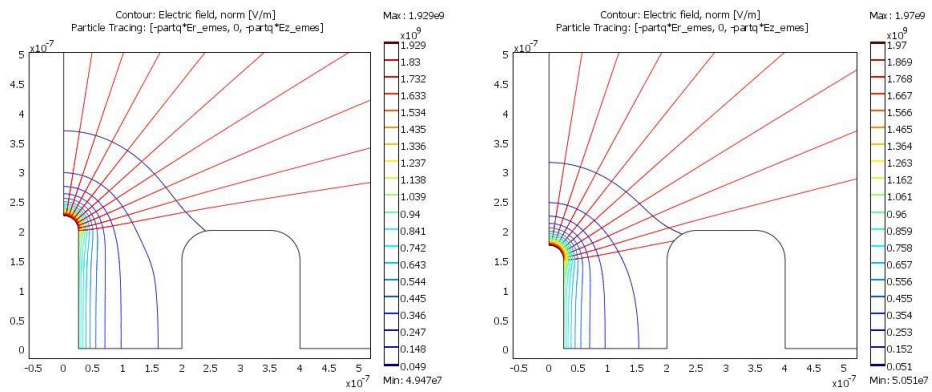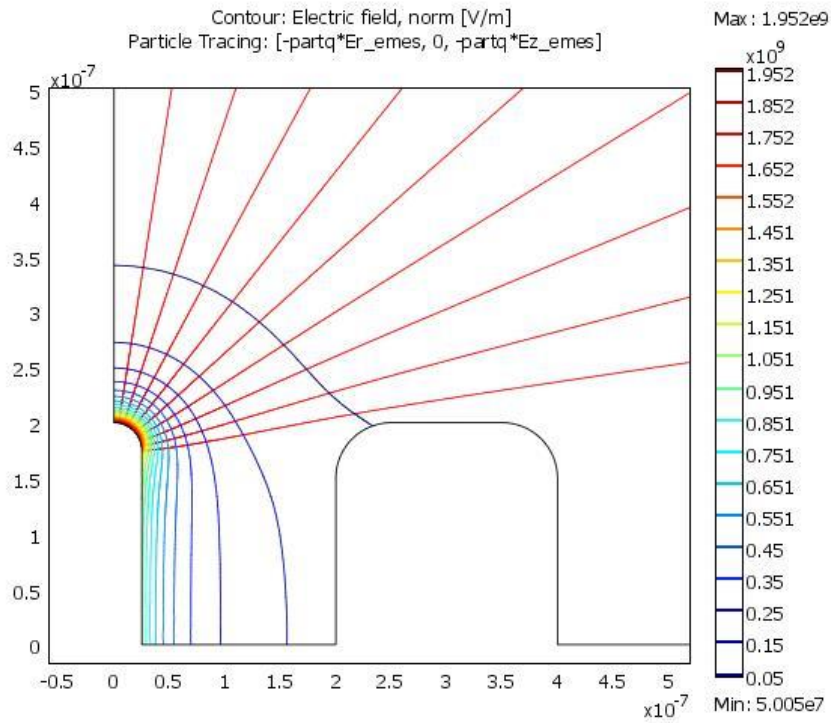
Figure 4-8: 2D axial symmetry of electric field strength at the emitter apex and the transmission efficiency of a CNT emitter with a coaxial cylinder shape gate electrode (upper). When the CNT is higher than the gate (lower left), the field strength is low; when the CNT is higher than the gate (lower right), the transmission efficiency is low.

emitter and the gate electrode are self-centered and self-aligned. Emission current transmission efficiency is an important property of triode field emitters [129, 130]. To calculate the transmission efficiency, a 2D axial symmetry model is used. In the simulation model, the radius of the CNT is 25nm; the top for gate and the tip of emitter are at the same height. The emitter-gate gap is 175nm; gate thickness is 200nm; the gate voltage is 50V; and the anode voltage is 100 V. The local field enhancement is basically focused on the top of CNT tip and the field strength is 1.71×10^9 V/m. Figure 4-8A shows the electric field distribution and electron trajectories of the coaxial gate based triode emitter. Simulation results show that when the emitter height is lowered for 25 nm, the field strength of the emitter apex increases 1%, but more electrons are collected by the gate electrode. On the other hand, when the emitter is 25 nm higher than the top surface of the gate electrode, less electrons are attracted by the gate, but the field strength of the emitter apex decreases 2%. Figure 4-8B and 4-8C shows that a emitter tip higher than the gate have a high efficiency, but a low emission current; in contrast, a emitter tip lower than the gate have a high emission current but a low efficiency. In conclusion, to get the best performance and a simple fabrication process, the emitter tip and the gate electrode should have the same height. In Spindt cathode and emitter structures analogous to this coaxial gated emitters, less than 1% emitted electrons are collected by the get electrode [131, 132]. Therefore, the transmission efficiency is over 99%, much higher than that of a gated thin film emitter (80%) [133].

4.6 Chapter Summary

Height and tip diameter of vertically aligned CNT array grown by PECVD follows Gaussian distribution. This geometry non-uniformity leads to a significant non-uniformity of electric field strength and emission current. Some optimized CNTs dominate the total

emission current of an emitter array. A ballast resistor in serial with a CNT emitter works as a current limiter, and has the capability to prevent the emitter from over current. The effect of the ballast resistor is simulated and theoretically proof that it has the capability of improving the emission uniformity. As a result, the stability of the emitter array is also improved. In addition, the effect of the ballast resistor in an emitter with a coaxial gate electrode, the geometry of the resistivity layer, and transmission efficiency of coaxial cylinder gate are also calculated.

Chapter 5

Fabrication Process of Field Emission Cathode

5.1 Introduction

The goal of this project is to fabricate field emission cathodes for some special X-ray applications. Electronic brachytherapy requires tiny X-ray tubes [134], radiation sterilization needs a flat panel X-ray source [20], and stationary computer tomography desires a high speed pulse X-ray beam array [135, 136]. Diode structure works well for tiny X-ray tube and flat panel X-ray source, but triode structure is required for pulse X-ray beam array.

A field emission cathode for diode X-ray sources is an array of ballasted emitter. Each ballasted emitter consists of a CNT field emitter and a ballast resistor. On the other hand, triode X-ray source cathode is an array of gated ballasted emitter, which consists of a CNT emitter, a ballast resistor, and a coaxial cylinder gate electrode. In this chapter, the fabrication processes of these components, namely, CNT emitter, ballast resistor, and cylinder gate, are described. Due to the limitation of the fabrication facility we can access, the fabrication has not achieved the desired best results. The optimized fabrication process is introduced at the end of this chapter for future works.

5.2 Fabrication Process of the Components

5.2.1 Carbon Nanotube Synthesis

Carbon nanotube has remarkable high electrical conductivity, high melting point, low surface diffusion, and high mechanical strength. Carbon based field emitter can work stably in a vacuum with a pressure of 1×10^7 Torr [45, 60]. Therefore, carbon nanotube is one of the best candidates of field emission material. High density vertically aligned CNT array can be synthesized by CVD [137], water-assisted chemical vapor deposition [138], thermal chemical

vapor deposition [139], and PECVD [107]. In high density CNT arrays, vertical alignment of CNTs relies on a crowding effect and maximizes van der Waal's interactions between the side wall of neighboring CNTs [140, 141]. When the CNT bundle diameter decrease to micrometer scale, the crowding effect is not sufficient to keep the CNTs well aligned [68]. In a low density CNT array, CNTs are far apart from neighbors and considered as free standing CNTs. In a free standing CNT array, due to the lack of supporting, CNTs tend to bending during the growth process. Therefore, some external forces are needed to grow free standing CNTs. Since CNTs are all electrically conductive, a growing CNT under an electric field have a tendency to align with the electric field. Electric fields can orient CNTs owing to their large and highly anisotropic polarizability [142]. In the literature, dc-PECVD is the only method to grow free standing CNTs [91]. Due to the low working temperature, CNTs grown by PECVD are all multi-wall CNTs. Even though, theoretically, free standing single wall CNT has much lower turn-on voltage and much better performance than multi wall CNTs, low density single wall or double wall CNT array has not been reported. By far, low density vertically aligned multi wall CNT array is the only choice for our device.

The results of CNT synthesis process can be affected by many factors, such as the catalyst materials, the thickness and size of the catalyst dots, the deposition temperature, the plasma expose time, the applied bias voltage, and the gas-flow ratio. The synthesis process has two steps, i.e. i) prepare the substrate by deposit patterned catalyst dots, and ii) grow CNT on the catalyst dots by PECVD. We outsource the CNT growth to NanoLab Inc. (Waltham, Massachusetts, USA). Therefore we can focus on the catalyst deposition. In our device design, inter-tube distance is an important factor and the CNT must grow on the connection pad of ballast resistors, so the location of CNTs on the substrate surface is

critical. Because the CNTs grow only from the catalyst dots, the sites of catalyst dots determine spatial location of CNTs. Therefore, preparation of catalytic dots is very important on synthesizing low density vertically aligned CNT arrays. The process of preparing catalyst dots for growing CNTs is a standard lift-off procedure. The size of the catalyst dots is less than one micro-meter; therefore, conventional photo-lithography is not suitable. First, a layer of electron-beam resist is spun on the substrate. Second, the resist is patterned by electron-beam lithography to form a catalyst dots array. Third, a layer of nickel is deposited on the patterned e-beam resist. Finally, the resist is removed and leave the catalyst dots on the substrate.

To grow a single isolated CNT from a single catalyst dot, the size of the dot is critical. Before CNT is grown, the substrate is heated up to about 1000 K [107, 143, 144]. The catalyst dots coalesce to form catalyst droplets, one CNT per droplet [143]. If the
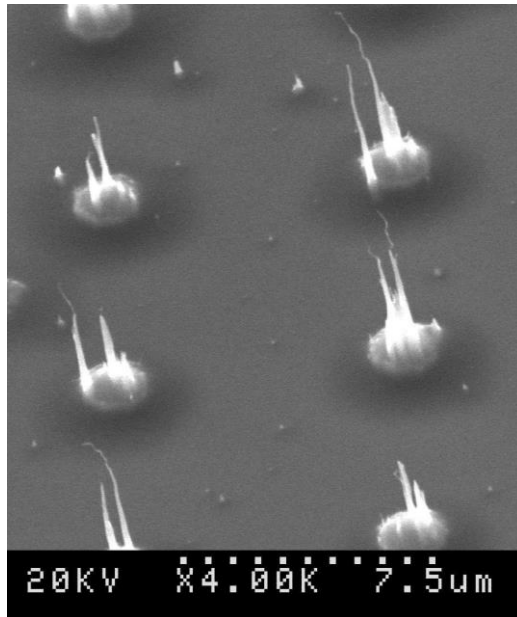
Figure 5-1: Multiple short carbon cone and short CNT
grown on connection pads. This result indicate the catalyst
nucleation process is critical

diameter of the catalyst dots is bigger than 350 nm [143] or 300 nm [107], multiple catalyst droplets are formed; thus multiple CNTs are grown from one catalyst dot. In these articles, they use a several nanometer buffer layer between the catalyst dots and the substrate, and their catalyst layer is range from 7 nm to 15 nm. In our fabrication process, when we make catalyst dots with 200 nm diameter and 35 nm thickness, multiple carbon nanocones are formed on single site (shown in Figure 5-1). This result lead to two conflicting conclusions: short cone is caused by insufficient catalyst, but multiple growths mean too much catalyst on one site. By changing the size of the catalyst dots, we figure out that the nucleation process is also critical to produce single CNT on a catalyst dots. However, some details of this process are still not clear. Finally, we find that the catalyst size of 100 nm diameter and 75 nm thickness is a working parameter. In a standard lift-off process, thickness of the resist is at least three times thicker than the deposited layer. The thickness of the catalyst layer is
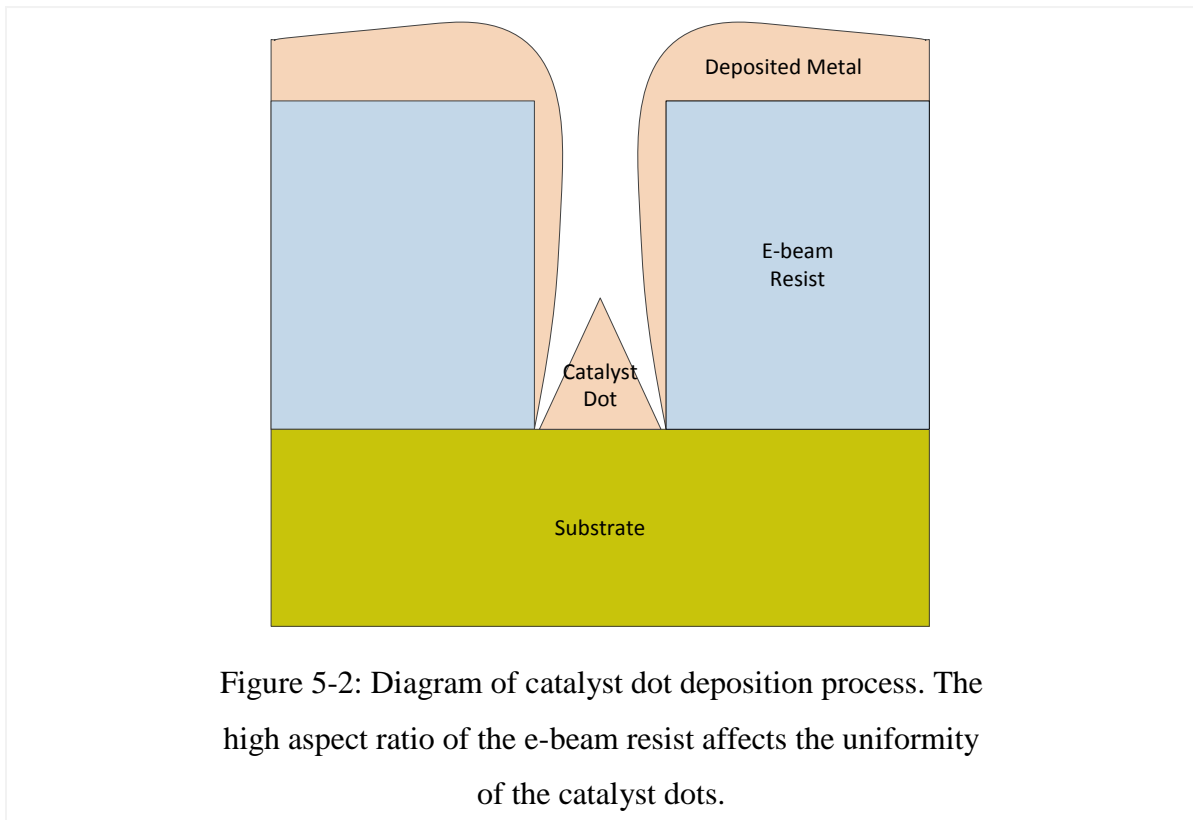
Figure 5-2: Diagram of catalyst dot deposition process. The high aspect ratio of the e-beam resist affects the uniformity of the catalyst dots.

75 nm, thus, the e-beam resist layer is 225 nm. Since the diameter of the catalyst dots is 100 nm, the aspect ratio of the pattern is 2.25. Figure 5-2 shows a cross section diagram of the catalyst dot pattern. During the deposition of the catalyst, the metal is deposited not only on the bottom of the pattern well, but also on the side wall of the well. Therefore, the opening of the well shrinks and affects the accuracy and uniformity of the catalyst dot size. An emission array consists of several thousand emitters, the size of the catalyst dots is critical to the CNT height and diameter. To get a high uniformity of the emission current and emitter dimension, a highly uniform catalyst dots array is necessary. To improve the uniformity of the catalyst dot size, more study on the nucleation process is necessary.

5.2.2 Fabrication Process of Ballast Resistor

As described in Chapter 3, we adopt a vertical resistor structure and employ a connection pad structure to form the ballast resistor. The fabrication process is straightforward. First, a thin film of metal is deposited on a non-conductive substrate to form a bottom electrode. Second, a layer of poly-silicon is deposited on the electrode layer. Third, a connection pad array is deposited and patterned on the resistive layer. After making the ballast resistor, a CNT catalyst dot array need to be deposited on top of the connection pads. Due to the thickness of connection pad is close to thickness of the e-beam resist, the connection pad can affect the uniformity of the catalyst dot size.

The following description discusses the process of deposition and patterning of the connection pad and CNT catalyst dots. There are two methods to fabricate this structure: (i) deposit connection pad by lift-off and then deposit catalyst dots by lift-off; and (ii) deposit a connection layer without patterning, deposit catalyst dots by lift-off, then pattern the connection pad by wet etching. The problem of the first method is that, after lifting off the

connection pads, the surface of the sample is no longer flat, and the thickness of the e-beam resist on the connection pad is not uniform. This phenomenon is similar to the existence of edge-dead at wafers edge during the photoresist spin-coating. This thickness non-uniformity of the e-beam resist can affect the size of the catalyst dots. Due to the critical nature of the CNT catalyst size, this process may lead to a poor uniformity of CNTs. On the other hand, if the connection layer is deposited without patterning, the e-beam resist layer is perfectly flat, and the catalyst dots can achieve their best uniformity. After the catalyst dots are lifted-off, a layer of e-beam resist on the connection layer is patterned. Next, the wafer is immersed in a chrome etchant and the connection pad is obtained. The problem of this process is that the undercut of wet etching makes the pattern dimensions poorly defined. Furthermore, the edge is not as smooth as that of a lift-off process. As a result, the size uniformity of the connection pad is not as good as the former process. When comparing these two processes, the second one has better CNT uniformity. Thus we adopt the second process for the fabrication.

5.2.3 Fabrication process of Cylinder Gate

The cylinder gate is fabricated on top of the ballasted low density vertically aligned CNT array. First, a thin layer of insulator is deposited on the substrate. To get a uniform emitter-gate gap, a conformal layer is desired. Simulation result in section 4.3.3 shows that the field strength at the side wall of the emitter is very high; therefore a high dielectric strength of the insulator layer is desired. Several deposition processes can be used to deposit dielectric thin film, however, the quality of the deposited film and working conditions are different. Table 5-1 lists some dielectric thin film deposition methods. Among these methods PECVD and sputtering deposited SiO_2 and atomic layer deposition (ALD) deposited Al_2O_3

Table 5-1: Comparison of silicon dioxide deposition methods

Deposition method	Temperature (°C)	Composition	Step coverage	Dielectric constant
PECVD	200	$SiO_{1.9}(H)$	non-conformal	4.9
ALD	200-300	SiO_2	conformal	N/A
CVD SiH_4+O_2	450	SiO_2 (H)	non-conformal	4.3
CVD from TEOS	700	SiO_2	conformal	4.0
Sputtering	Low Temperature	SiO_2	conformal	3.9
e-Beam Evaporation	Low Temperature	SiO_2	non-conformal	5

on CNT have been demonstrated and give good results [145, 146]. ALD is a self-limiting, sequential surface chemistry that deposits conformal thin-films of materials onto substrates. ALD deposited film thickness depends only on the number of reaction cycles, which makes the thickness control accurate and simple, furthermore, the film is defect free [147]. Therefore, ALD film has the best quality of the insulator layer. However, the slowness is the major limitation of the ALD. On the other hand, PECVD has high deposition rate and the deposition on the CNT side wall is uniform. Since ALD facility is not accessible for our fabrication, we use PECVD to deposit the insulator layer. Next, a layer of metal is deposited as the gate electrode by electron-beam evaporator. Since the insulator layer has a uniform thickness, the emitter tips are located at the center of the cylinder shape gate. The fabrication process is self-centered.

After the gate electrode is deposited, a supporting layer is deposited, and the sample is polished. In this step, caps on CNT emitters are removed and the CNT apexes are exposed. Then, the insulator layer between the emitter tip and the gate electrode is removed by dry etch or wet etch. The polishing process makes the top surface of the sample flat, therefore,
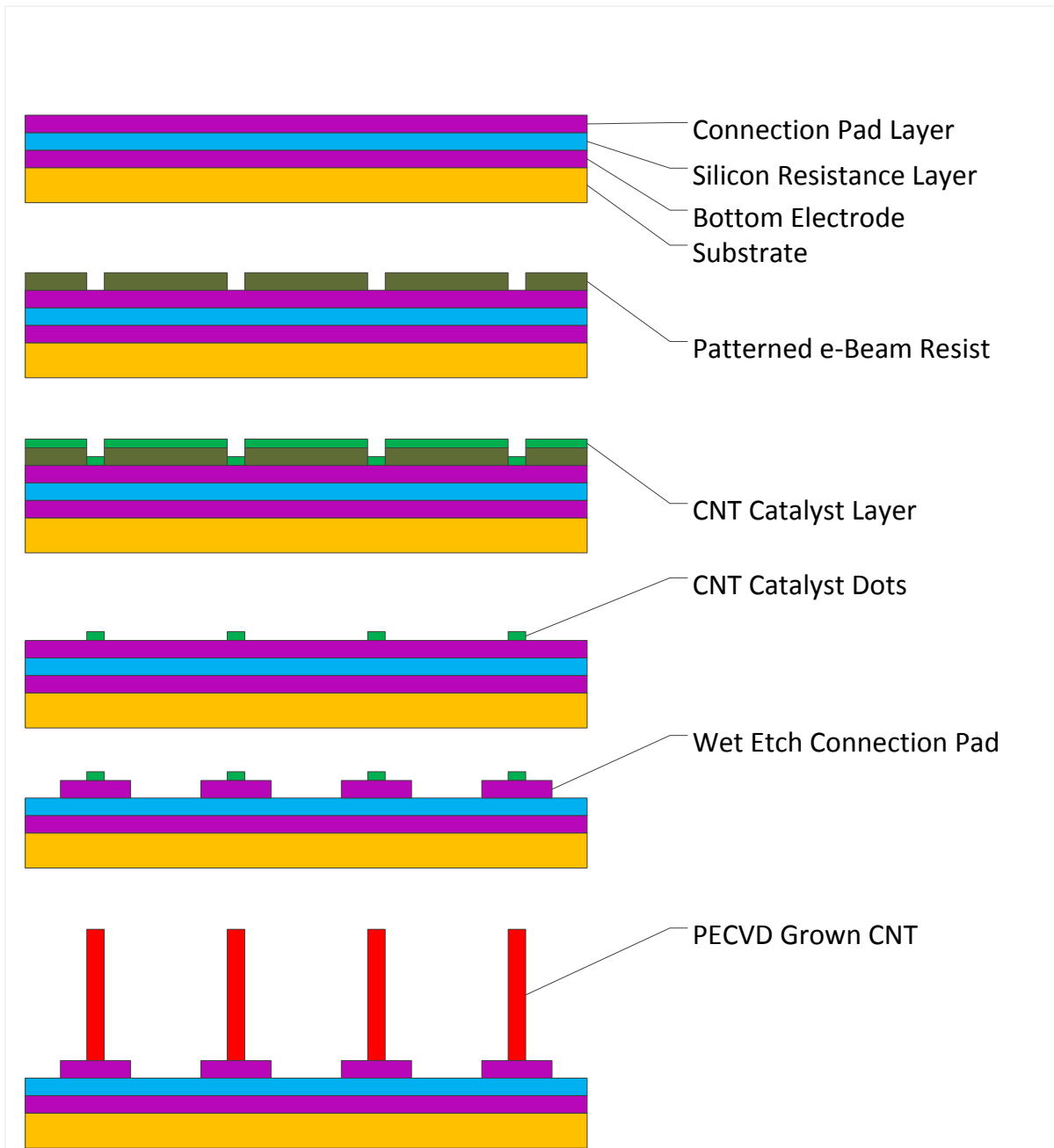
Figure 5-3: Step-by-step fabrication process of non-gated CNT emitter array. 1. 200nm chrome, 500nm poly-silicon, 20nm chrome are deposited on the substrate; 2. e-beam resist is coated and patterned on the substrate; 3. CNT catalyst layer is deposited on the resist; 4. e-beam resist is removed to form catalyst dots; 5. top metal layer is etched to form connection pad; 6. CNT is grown from the catalyst dots by PECVD.
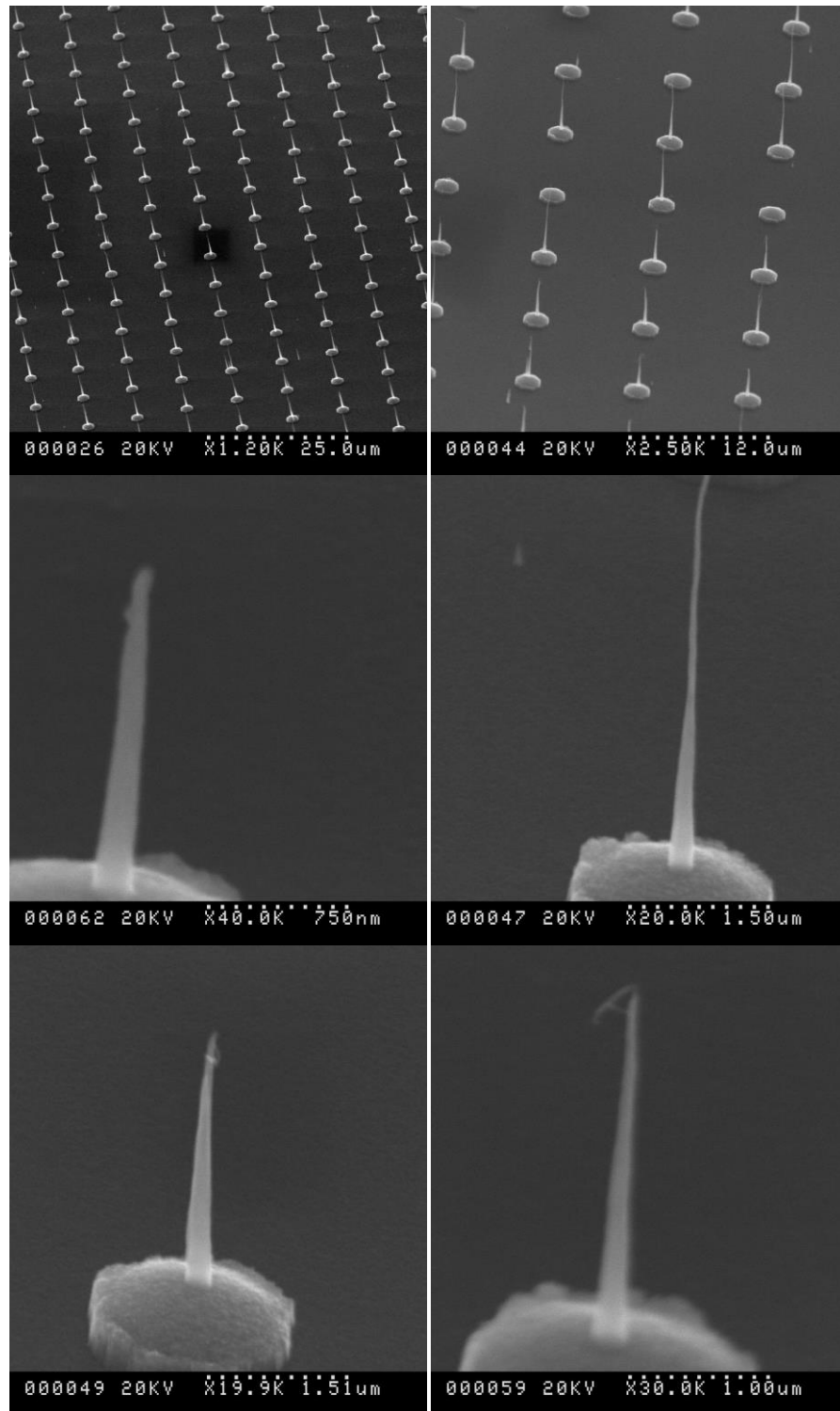
Figure 5-4: SEM images of free standing vertically aligned CNT grown on connection pad. In an emitter array, the height of the CNTs is not uniform. Furthermore, the CNT tips have all kinds of shape.

the CNT tip and the gate electrode has the same height. As a result, the emitter tips and the gate electrodes are self-aligned.

5.3 Non-gated Field Emitter

Tiny X-ray tube for electronic brachytherapy and flat panel X-ray source for radiation sterilization do not need a gate electrode to switch the X-ray beam. A simplified CNT emitter array with ballast resistors and a diode configuration is sufficient for these applications. Each emitter consists of a ballast resistor and a vertically aligned CNT. The fabrication process has been described above. Since the emitter do not need to be addressable, the substrate is used as the cathode electrode and the bottom electrode layer do not need to be patterned. The main propose of the bottom electrode is to work as a buffer layer to avoid the doping materials in the substrate diffuse into the resistor layer and lead to a resistance decrease. Figure 5-3 shows the step by step fabrication process of these field emission cathodes. Figure 5-4 show some SEM images of the emitter. In the CNT array, some defects can be seen and the shape and height of the CNT tips are vary. Even ballast resistor has the capability of overcome the emitter tip non-uniformity; a better uniformity is still desired. More studies on the CNT synthesis process are needed. In this fabrication process, electron beam lithography is employed to pattern the CNT catalyst dots. Due to the high cost, electron beam lithography is not suitable for mass produce. Nano-imprint is an alternative to the electron beam lithography to reduce the cost. Another concern of this fabrication process is making several thousand CNTs uniform is still a challenge.

5.4 Cylinder Gated Field Emitter

Field emission cathode array for addressable multiple beam X-ray source needs a set of row electrodes and column electrodes. The cylinder gate is fabricated on the
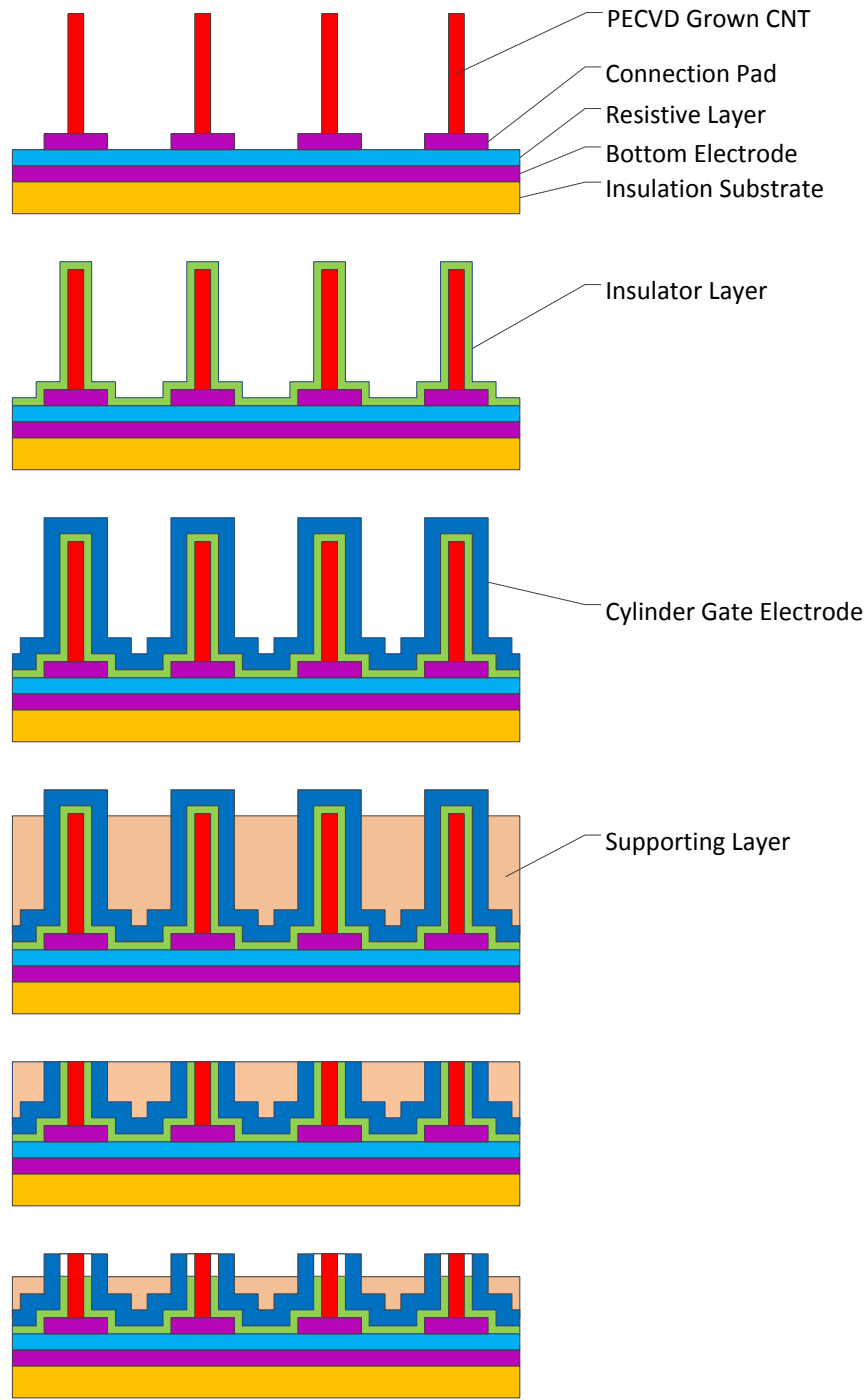
Figure 5-5: Step-by-step fabrication process of coaxial cylinder shape gate electrode on ballasted CNT arrays: 1. PECVD grown CNT; 2. deposit a conformal insulator layer; 3. deposit a layer of metal as gate electrode; 4. deposit a layer of supporting material; 5. expose the CNT tip by polish; and 6. remove insulator between CNT and the gate by dry etch
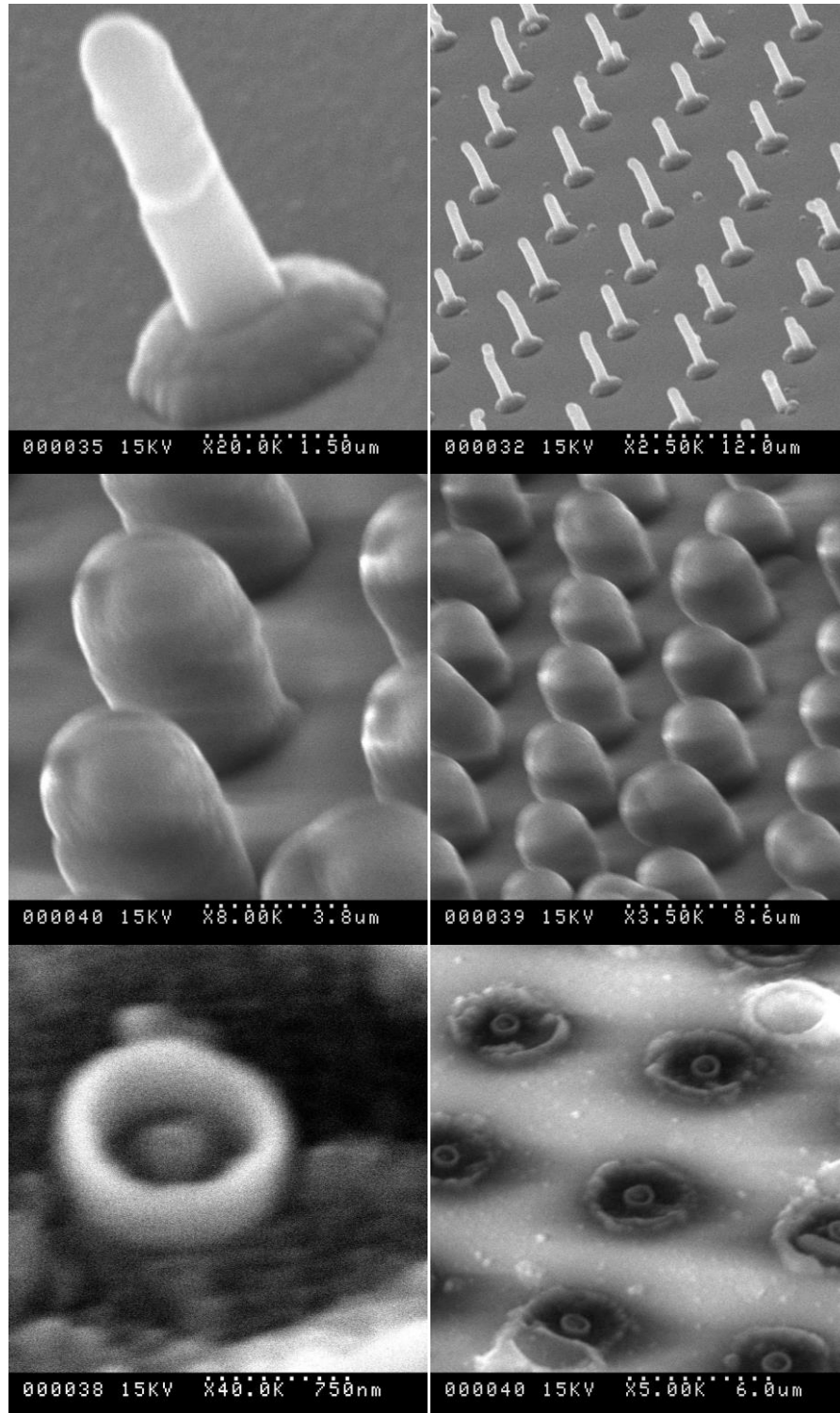
Figure 5-6: SEM images of the fabrication process of the gated emitter. CNT coated with insulator layer and metal electrode (upper); deposit supporting layer (middle); and CNT emitter with coaxial cylinder shape gate electrode (lower).
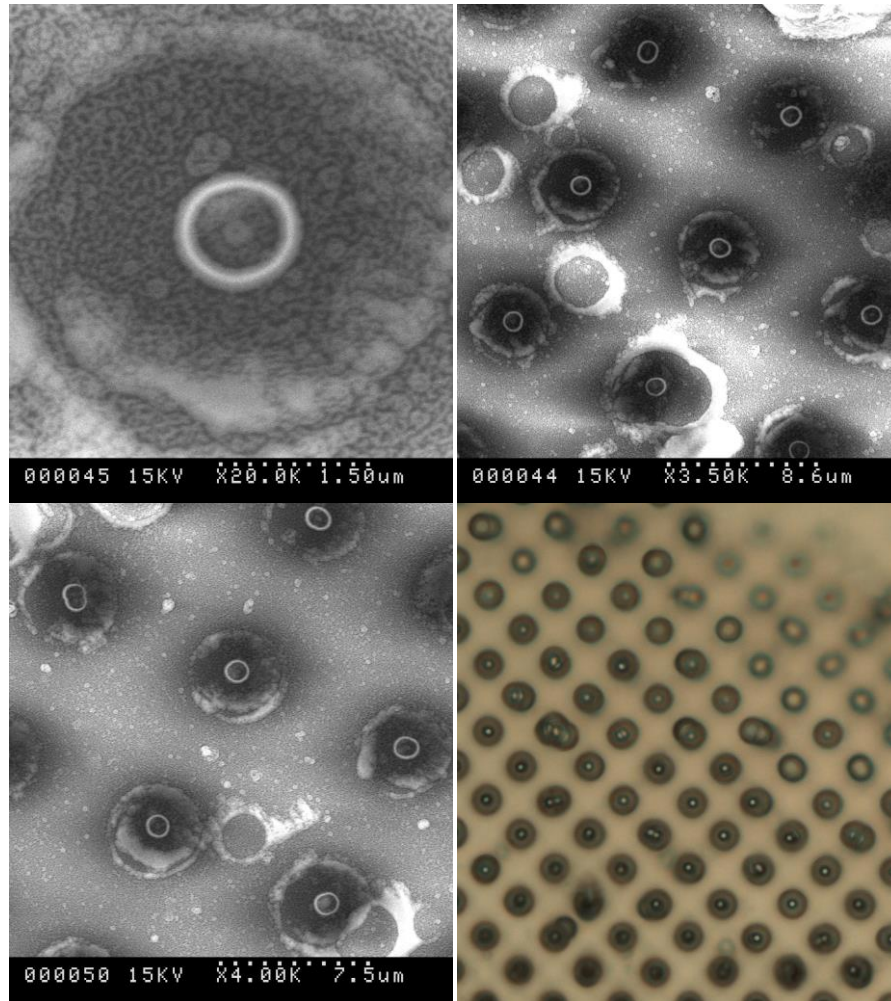
Figure 5-7: SEM images and optical image (lower right) of top view of gated CNT emitters. Some defects can be seen in these images.

abovementioned CNT field emitter array. However, the substrate need to be insulated or insulator coated silicon wafer. The PECVD growth process requires a conductive substrate to avoid micro-arc destroy the sample. So the bottom electrodes need to be patterned after CNTs are grown. Figure 5-5 shows a diagram of step by step fabrication process of the cylinder gate. First, a conformal layer of insulator is deposited on the CNT emitter array by ADL, PECVD, or sputtering. Then, a thin metal film is coated on the insulator to form the cylinder shape gate. Next, a supporting layer is deposited on the gate electrode. The next
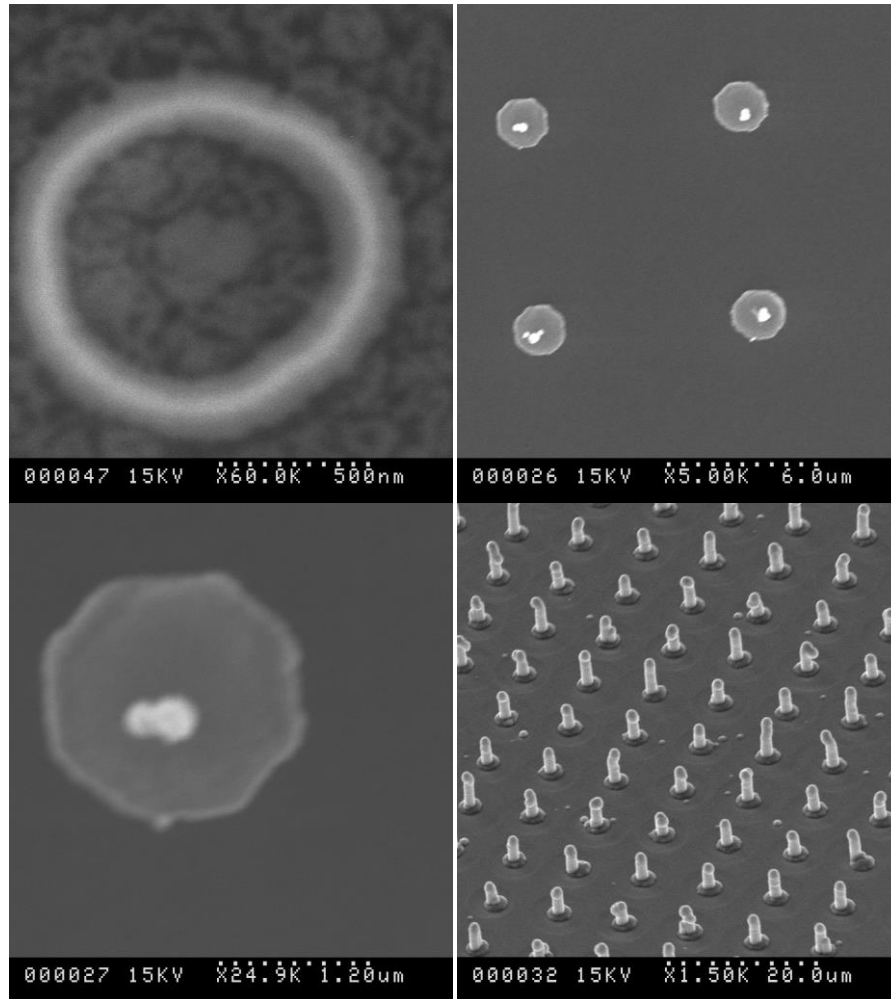
Figure 5-8: SEM images show defects of CNTs and gate electrodes. Multiple
CNTs are grown on individual connection pad lead to defects of gate electrodes.

steps are polish and etch the sample to expose the emitter tip and the gate electrode. SEM

images of these steps are shown in Figure 5-6. Figure 5-7 shows top view of SEM and optical

images of the emitters. In these top view images, the gate electrodes are not prefect cycle.

We believe this is caused by the defects of the CNTs. Figure 5-8 shows some defects of the

CNTs and coated CNTs. Some connection pads has multiple CNTs. Making a defect free

CNT array which consists several thousand CNTs is not feasible with an entry level

79

prototype fabrication facilities. We hope a high-end fabrication facilities may help us to make defect free CNT arrays.

5.5 Chapter Summary

In this chapter, the fabrication process of both non-gated emitter and gated emitter are discussed in detail. The non-gated CNT emitter consists of a ballast resistor array and a vertically aligned CNT array grown on top of the ballast resistors. The gated emitters consist of the non-gated CNT emitter and a cylinder shape gate electrode. The fabrication process of the gate electrode is self-aligned and self-centered. The fabrication process is straightforward, but the uniformity of CNTs needs some improvements.

Chapter 6
Electron Emission Properties of CNT Emitters

6.1 Field Emission from Ballasted CNT Array

Non-gated CNT array emitter can be used in tiny X-ray tube or flat-panel X-ray source with diode structure. The samples are tested with a simple diode configuration. The CNT sample is connected to the ground as a cathode. A silicon wafer is connected to a power supply to work as an anode. A 50 µm Polytetrafluoroethylene (PTFE) film is sandwiched between the cathode and anode. The emitter array has 2,121 CNTs in a 0.2 mm² octagon area. The CNTs are 10 µm apart and about 5 µm in height. The gap between CNT tip and the anode is about 45 µm. The sample is tested in a vacuum chamber with base pressure lower than 5×10^{-8} Torr.

Initially, current versus voltage characteristic of the as fabricated sample is tested. The I/V curve and F-N plot is shown in Figure 6-1. The F-N plot consists of two segments, i.e. high voltage segment (i) and low voltage segment (ii). The slope and intercept of the segments are S(i)=-3×10^7, I(i)=-49, S(ii) =-4×10^6, I(ii)=-53. From the Fowler-Nordheim theory, we get the field enhancement factor of β(i)= 2319, β(ii)= 17,398, and the effective emission area is A(i)=2.93 nm² A(ii)= 0.00096 nm². These tiny emission areas and low emission currents indicate the emission current corresponding to the segment (ii) is from single or a few emitters. With the voltage increase, more emitters are active and contribute to the total emission current.

The sample is then annealed for 100 hours at anode voltage 400 V. The current has a significant decrease in the first 9 hours and becomes stable in the rest 90 hours. The emission current is at sub-nano-amps scale. Then a 500 V annealing process is run for 30 hours and the
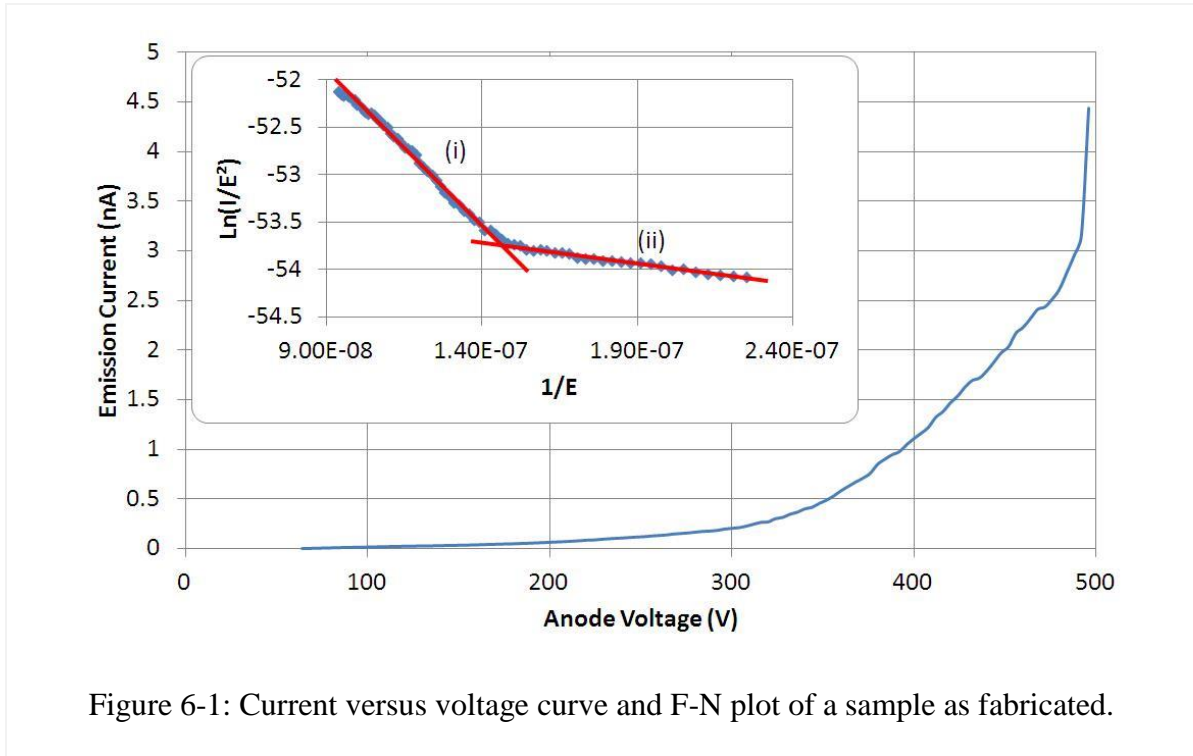
Figure 6-1: Current versus voltage curve and F-N plot of a sample as fabricated.
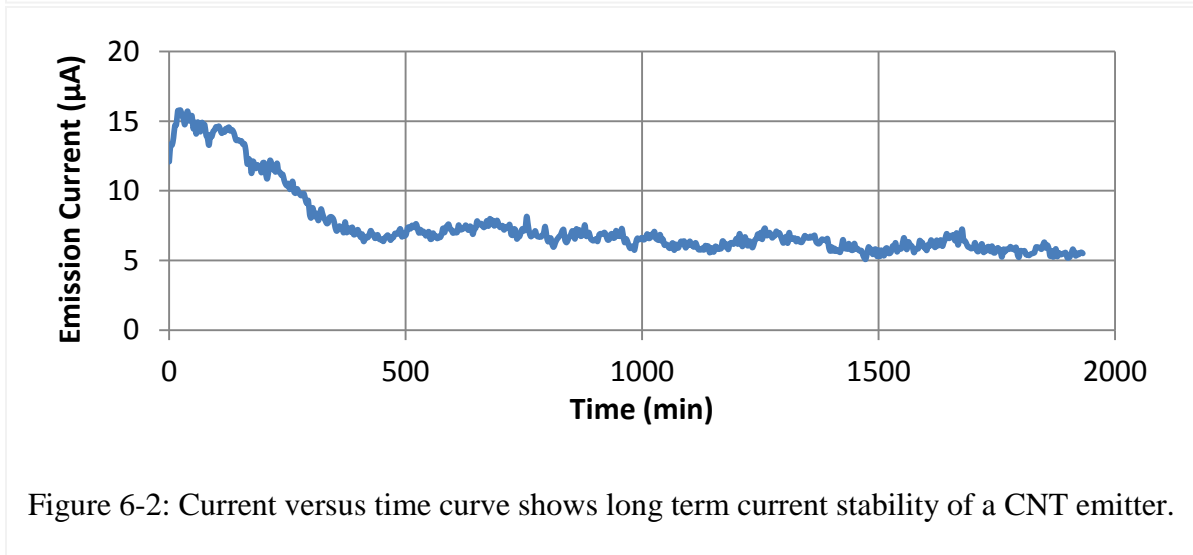
Figure 6-2: Current versus time curve shows long term current stability of a CNT emitter.

emission current range from 5 µA to 8 µA. Figure 6-2 shows the long term current stability

curve. The current verses voltage characteristic before and after the 500 V annealing process

are measured and shown in Figure 6-3. F-N plot and corresponding slope and intercept are

shown in the inset of Figure 6-3. Before the annealing, the field enhancement factor $\beta = 869$,

and the effective emission area $A = 3.4$ µm². After the annealing, the field enhancement
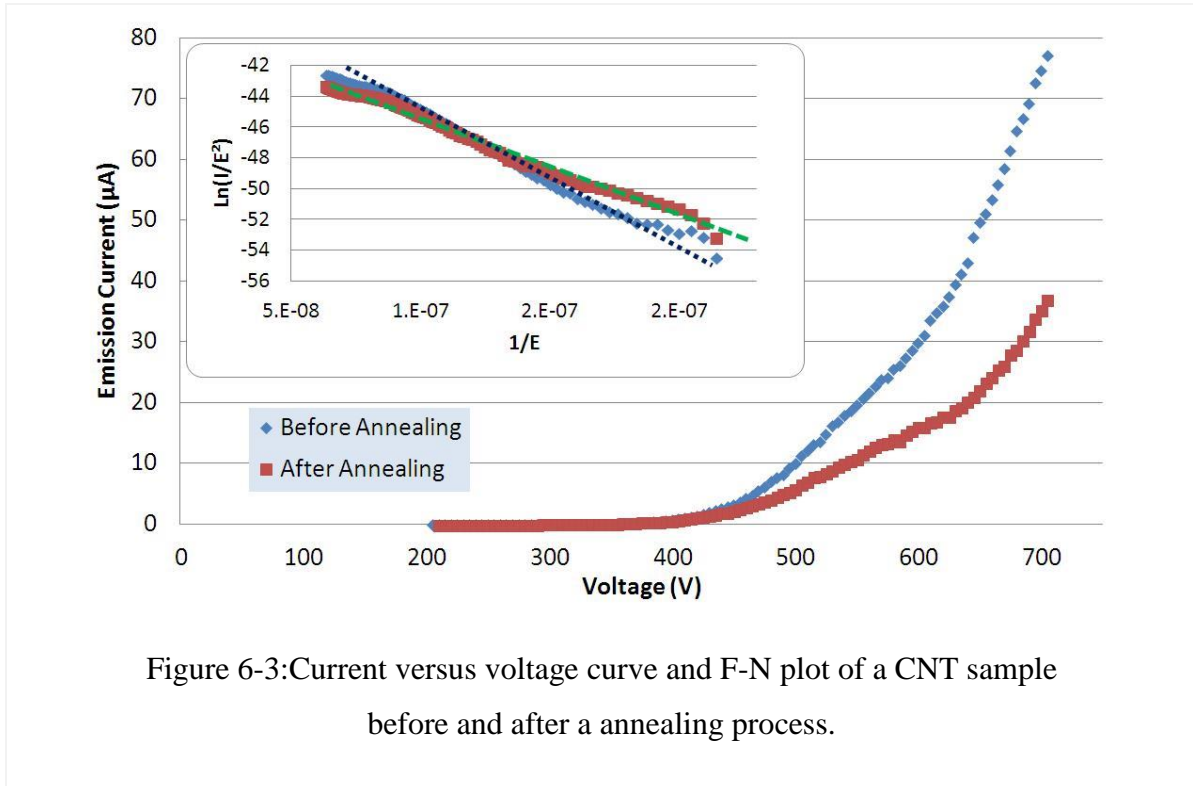
Figure 6-3:Current versus voltage curve and F-N plot of a CNT sample
before and after a annealing process.

factor $\beta = 1160$, and the effective emission area A = 0.26 μm^2. Even though the Fowler-Nordheim theory is not accurate enough to quantitatively calculate the emission area, it is still can be used to qualitatively analyses the emitter performance. In the first several hours of the 400 V 100 hours annealing process, gas molecules absorbed on the emitter is removed. Thus, the emitter surface are cleaned and smoothed.

After the emitter is annealed, the emission current decreases significantly. The effective emission area decreases from several square micrometers to less than one square micrometer. The average emission current is 37 nA per CNT. Suppose the ballast resistor is 60 MΩ, voltage drop on the ballast resistor is 2.2 V, less than 0.3% of the anode voltage (700 V). Therefore, the effect of the ballast resistor at this current level is negligible. During the 30 hours 500 V annealing process, the emission current of 700 V decrease from 77 uA to 37 uA. This decrease indicates some of the emission sites are degraded and effective emission area decreased or the surface cleaning process decreases the field enhancement factor.
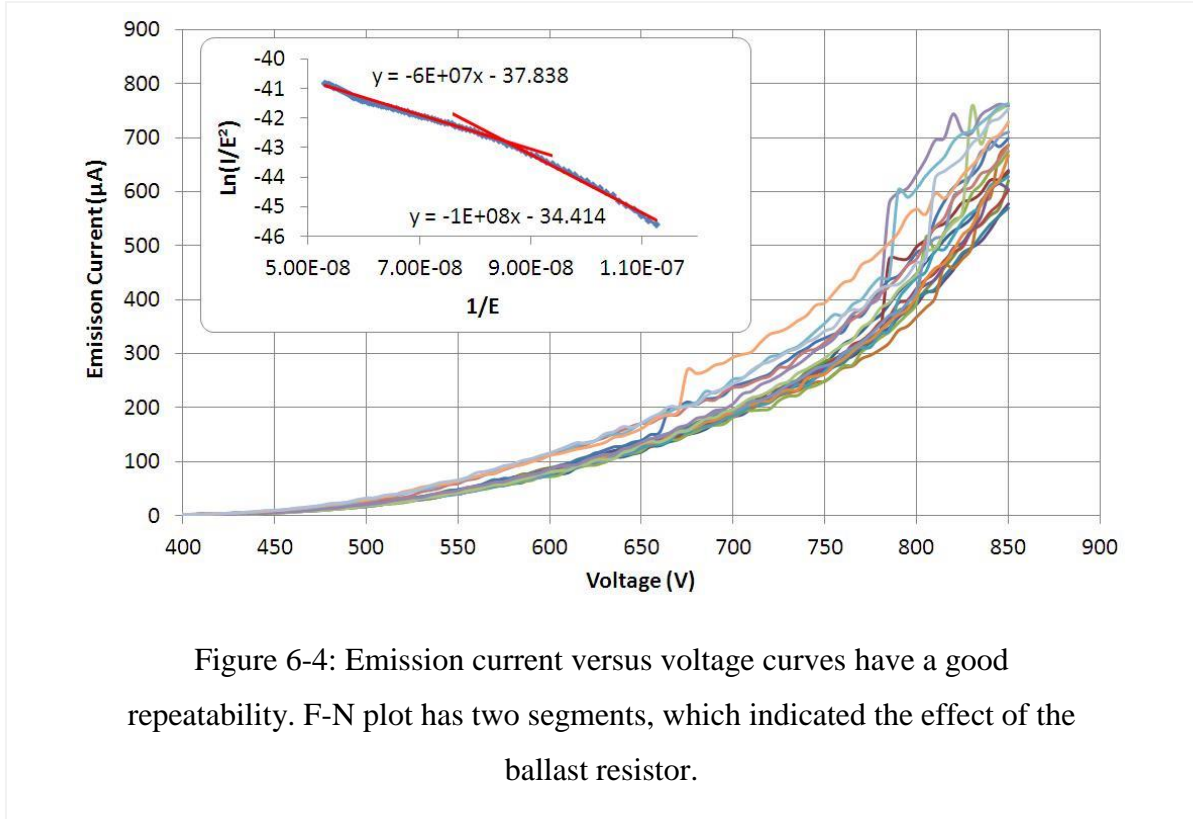
Figure 6-4: Emission current versus voltage curves have a good repeatability. F-N plot has two segments, which indicated the effect of the ballast resistor.

By increase the anode voltage to 850 V, the maximum emission current increase to over 750 μA. Figure 6-4 shows the emission current has a good repeatability. Inset of Figure 6-4 shows the F-N plot of average current has two segments. The high voltage segment has a higher field enhancement factor and a smaller emission area than the low voltage segment. The junction of these two segments at 550 V and the corresponding current is 48 μA. Even though the F-N pot bending may caused by many factors, we believe this bending and the slope decreasing is related to the existing of the ballast resistor [148]. For the high voltage segment, filed enhancement factor is β=695, and effective emission area is A= 83 μm². Average emission area is 0.04 μm²/CNT. Average emission current is 0.32 μA/CNT at 850 V. Given a ballast resistance of 60 MΩ, the voltage drop on the ballast resistor is 19 V. Refer to our early simulation result, we believe voltage drop is high enough to limit the emission current and avoid of the emitter over current.

In briefly, the above experiments indicate the ballasted CNT emitter array can provide an overall emission current over 750 µA with a good repeatability and stability. The current density of the sample is 300 mA/cm².

6.2 Self Heating Schottky Emission from CNT Array

Schottky emission has largely replaced earlier electron source technologies and become predominant in today's focused electron beam equipment. When compared with cold field emission, Schottky emission is more stable, has lower noise and is easier to operate as its vacuum requirement is less stringent (10^{-9} Torr). When compared with thermionic emission, Schottky emission has up to 100 times smaller source size, up to 10 times more brightness and longer lifetime. Conventional Schottky emitters consist of a needle shape emitter mounted on a filament. An extra current is needed to heat the emitter to a temperature of 1800 K. Although robust metal based Schottky emitter is widely used and field emission from carbon nanotube (CNT) is widely studied, studies of CNT based Schottky emitter are still rare.

During a study of CNT field emission failure, a temperature of 2,000 K is measured using an energy spectroscopy at an emission current of 1 uA [86]. Even though CNT can work stably in this working condition, the emission current cannot exceed 10 uA [116]. To get a high emission current, an emitter array is desired. Due to the non-uniformity of vertically aligned CNT arrays [69, 91, 107], emission currents are dominated by a small amount of emitters [124, 149, 150]. When the emitter array works in a high current regime, the optimized CNTs are burned and lead to the degradation of the emitter array. As a result, a high emission current density and high temperature of a CNT array is not achievable. Ballast resistor can improve the emission uniformity by limit the emission current of the optimized

emitters. As a result, a uniform emission current from an emitter array can be achieved. This high emission current can lead to a high temperature and change the emission property.

The experimental setup is the same as the above mentioned diode structure field emission experiment. A picoammeter is used to measure the emission current. A DC voltage is applied in either a scanning mode (stepped voltage) or a constant mode. In the scanning mode, the voltage (range from 400 V to 800 V) increases by a specific value every 5s and the current of each voltage is measured to obtain a current versus voltage curve. On the other hand, the constant mode is used for both heating purposes and characterizing the emission stability. The experiments are preformed after a 60 hr initial annealing process at 400 V to remove the residue gas molecules from the emitter surface.

The first observation of the effect of the temperature is that the emission current decrease follows a temperature decrease. First, a constant 800 V voltage is applied for 800 s

Figure 6-5: Emission current after the sample is heated up is higher than the current when the sample is cooled down. Inset shows the current-voltage curve between 600 to 700V of each round. In the F-N plot, the bend of the curves show the effect of the ballast resistor layer.
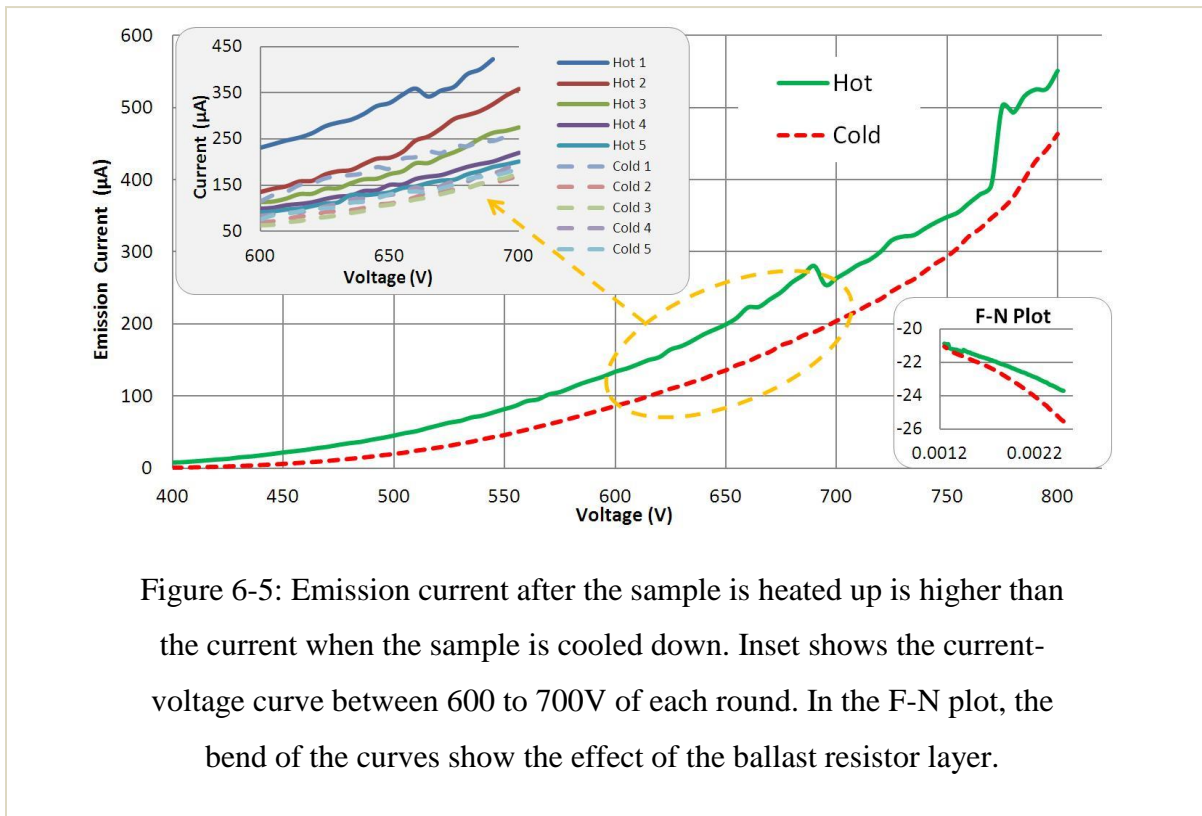
to heat up the sample. Then, a scanning voltage of 400 V to 800 V is subsequently applied for five rounds. When the sample is allowed to cool down to room temperature, scanning voltages of 400 V to 800 V are reapplied for five rounds. The I/V and F-N plots of the average emission current are shown in Figure 6-5. Inset of Figure 6-5 shows the I/V curve of each round of the experiment. Since 400 V to 800 V scanning voltage generates lower heat than that of an 800 V constant voltage, the temperature of the sample decreases during the scanning voltage. As a result, the emission current of the hot sample decreases from round to round. The emission current of the round 4 and round 5 of the hot sample is the same as the current of cold sample indicate higher current of the first two round of hot sample is caused by a higher temperature.

In a following experiment, a constant 800 V voltage is applied for 30 min. Figure 6-6 shows the current versus time curve of this experiment. The emission current is increased from 560 uA to 640 uA at 507 s. After 1,250 s, the emission current starts to increase and finally reaches 1.87 mA at 1,800 s. The test is stopped at this point to avoid a micro-arc

Figure 6-6: Emission current increase to 1.8mA under a
constant voltage in 30 minutes
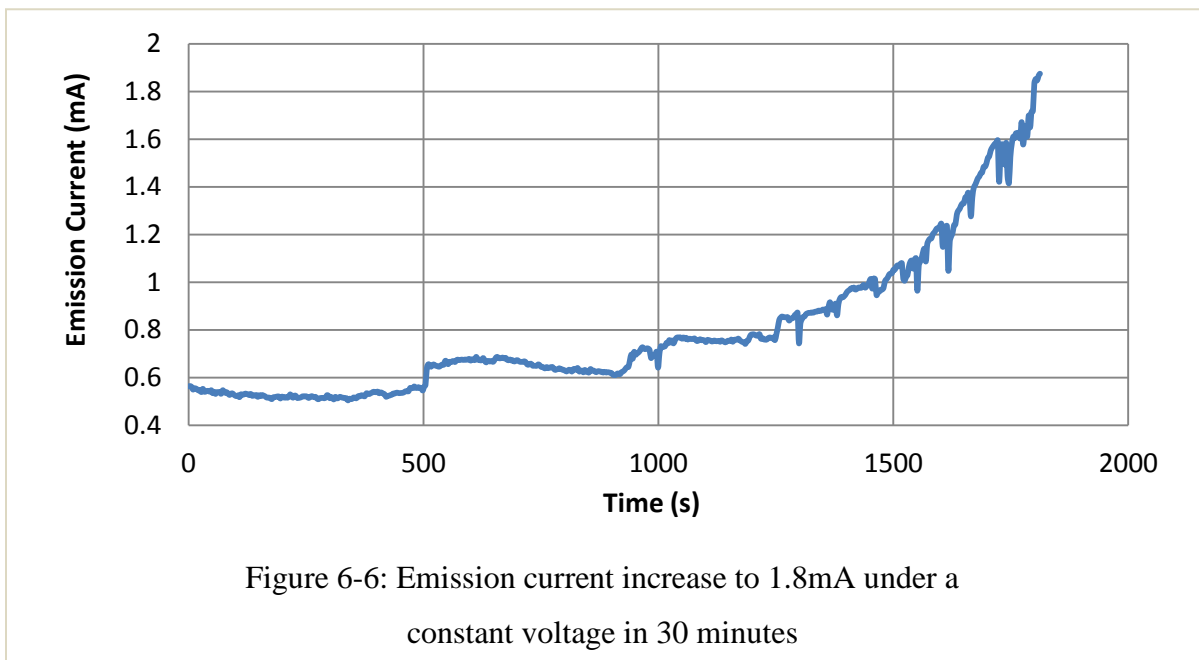
discharge caused by the thermal runaway. In this experiment, the emission current has no big change in the first 1,250s, but then increases from 800 μA to 1,870 μA in 600 seconds.

After the 30 min 800 V constant voltage experiment, a 400 V to 800 V scanning voltage is applied. The emission current achieves 1.6 mA, and decrease from round to round. This indicates the emitter array can withstand the current of 0.9 uA/ CNT during the Schottky emission. The average current versus voltage is shown in Figure 6-7A. Inset (i) and (ii) of
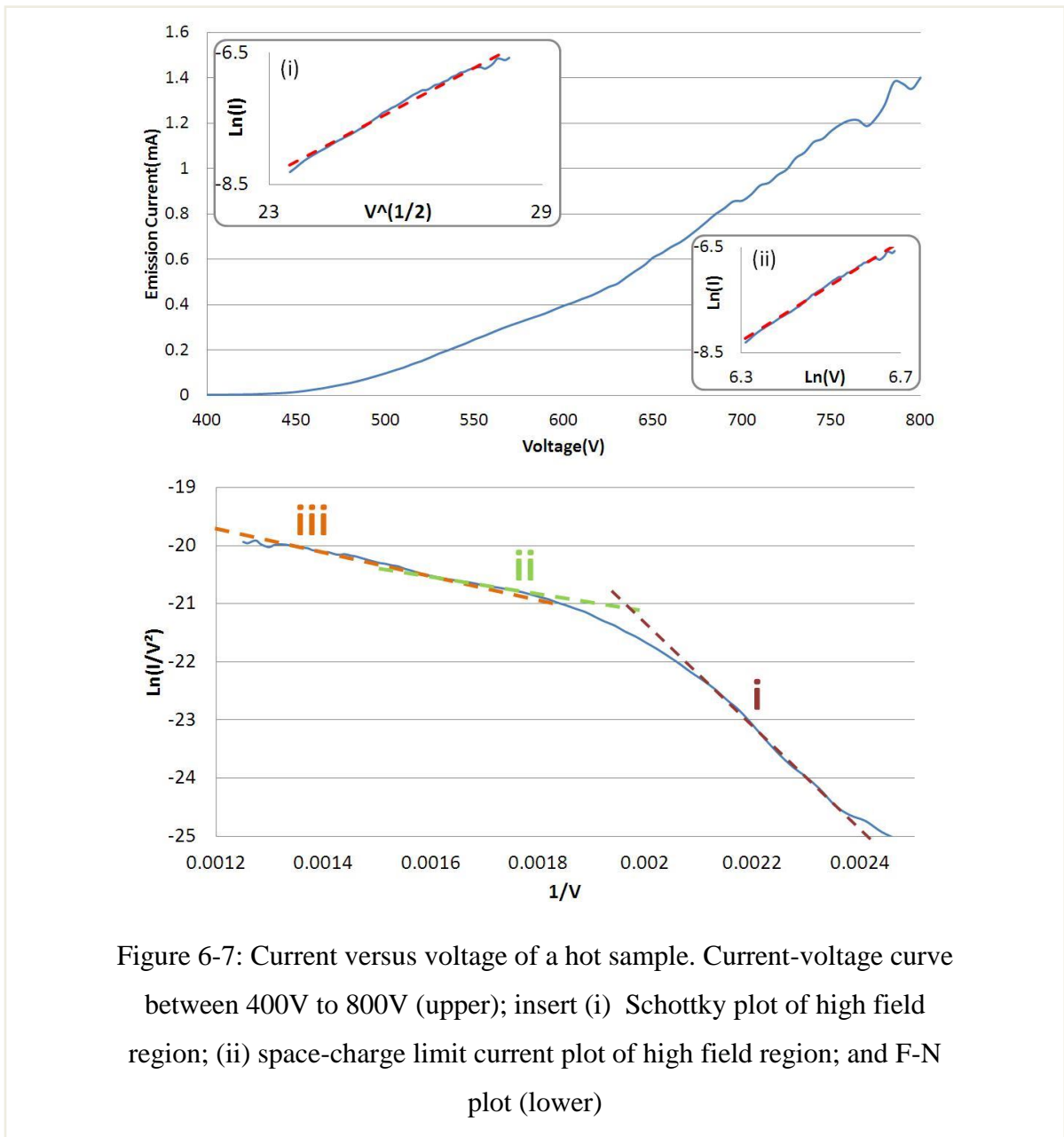
Figure 6-7: Current versus voltage of a hot sample. Current-voltage curve between 400V to 800V (upper); insert (i) Schottky plot of high field region; (ii) space-charge limit current plot of high field region; and F-N plot (lower)

Figure 6-7A show the high field regions of Schottky plot and space-charge limited current plot respectively. These two plots are close to a straight line indicate the emission in the high field regain are Schottky emission. The F-N plot of average current is shown in Figure 6-7B. The F-N plot consists of three segments. The low voltage (segment i) has the steepest slope. At a higher voltage and current (segment ii), the slope of the curve is decreased as the emission current is limited by the ballast resistor [148]. With an increase in voltage and
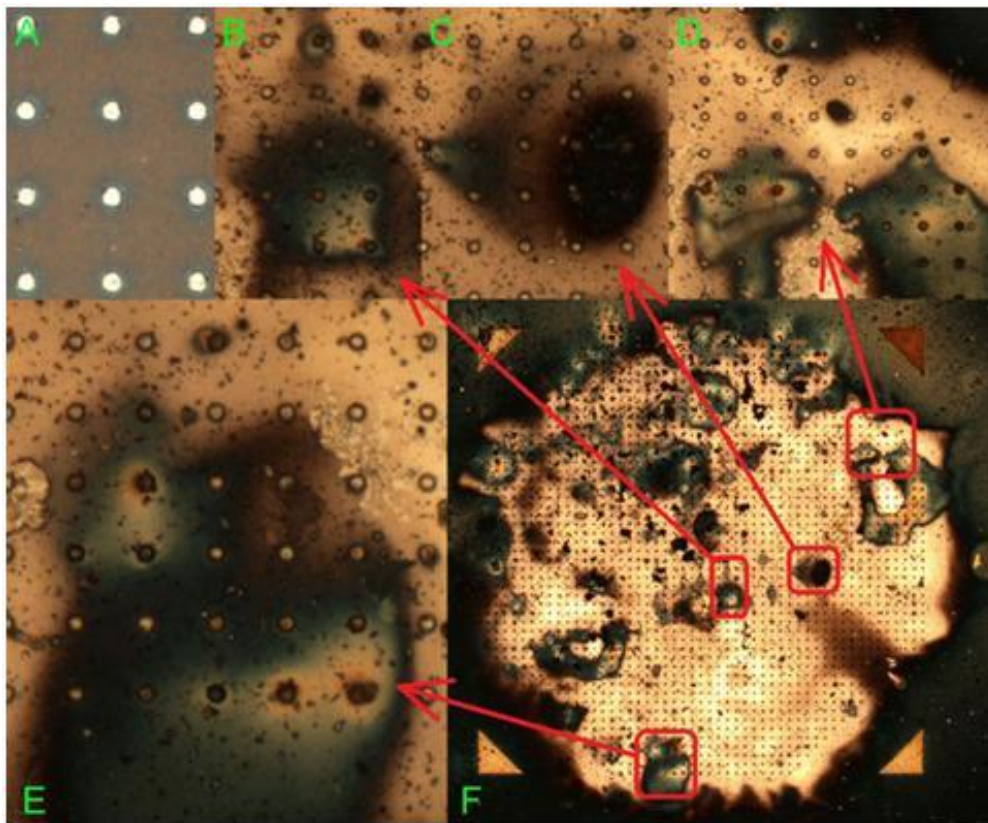
Figure 6-8: Optical image of the sample before and after emission test; A) before emission test, the sample has a even dark brown color and the bright spots are the resistor pad, the diameter of the pad is 2μm in diameter and has 10 μm gap; B-F) emission area changes to yellow in most areas and some of the areas are in very dark color show the FE sites which have a higher emission current.

current (segment iii), the slope of F-N curve becomes steeper than that of segment ii and has a good agreement with the study of high temperature single CNT emitter [86]. This indicates the emission is in Schottky emission regime.

The temperature of the emitter can be calculated by solving Richardson equation

$$J = AT^2 e^{\frac{-\varphi + \sqrt{e^3 F/4\pi\varepsilon_0}}{k_B T}} \tag{6.1}$$

where J is current density, A is a constant equals to 1.2×10^6, T is temperature, φ is work function, F is electrical field, ε_o is the electric constant, and k_B is the Boltzmann constant. In our experiment, the cathode-anode gap is 50 μm, voltage is 800 V and the current is 1.87 mA. The area of the sample is 0.2 mm², therefore, the current density is about 900 mA/cm². Since the CNT gap is about twice the CNT height, screening effect of the CNT array is negligible. We use the aspect ratio of the CNT as the field enhancement factor. From the SEM images, the diameter of CNT tips is about 25 nm to 30 nm and the height is about 5 μm. Thus, the field enhancement factor is between 150 and 200, we get the temperature is between 1690 K and 1840 K. This result has a good agreement with a measurement of the temperature of a single CNT emitter with an emission current of 1 μA [86].

Optical images of the sample before and after the experiments are shown in Figure 6-8. The color change of the sample shows a trace of high temperature. We believe the color change is related to the temperature change, and the uniformity of the color reflects the uniformity of the emission current. The color change occurs across most of the sample area indicates that most of the CNTs are involved in the emission. Area with a dark brown color (Figure 6-8C) indicates dominant emitters that contribute more current than other areas. Areas with gray color (Figure 6-8B, 6-8D, and 6-8E) indicate lower emission current than the

other areas. From the optical image shown in Figure 6-8F, we estimate that about 90% area of the sample changes to yellow, thus, 90% of the CNTs contribute to the emission. When compared to a non-ballasted CNT array that has just 10% of CNT involved in emission [124], the ballast resistor of our emitter cathode can effectively improve the emission uniformity, and thereby leads to a much higher total emission current. Figure 6-9 shows some SEM images of the sample after a high current Schottky emission. CNTs are shortened (Figure 6-9A to 6-9C), removed (Figure 6-9D) and splitted (Figure 6-9F). In Figure 6-9D and 6-9E, the substrate is damaged. We believe the CNT split and substrate damage is caused by electric micro-arc or ion bombardment. Since most of the emitter damages are CNT
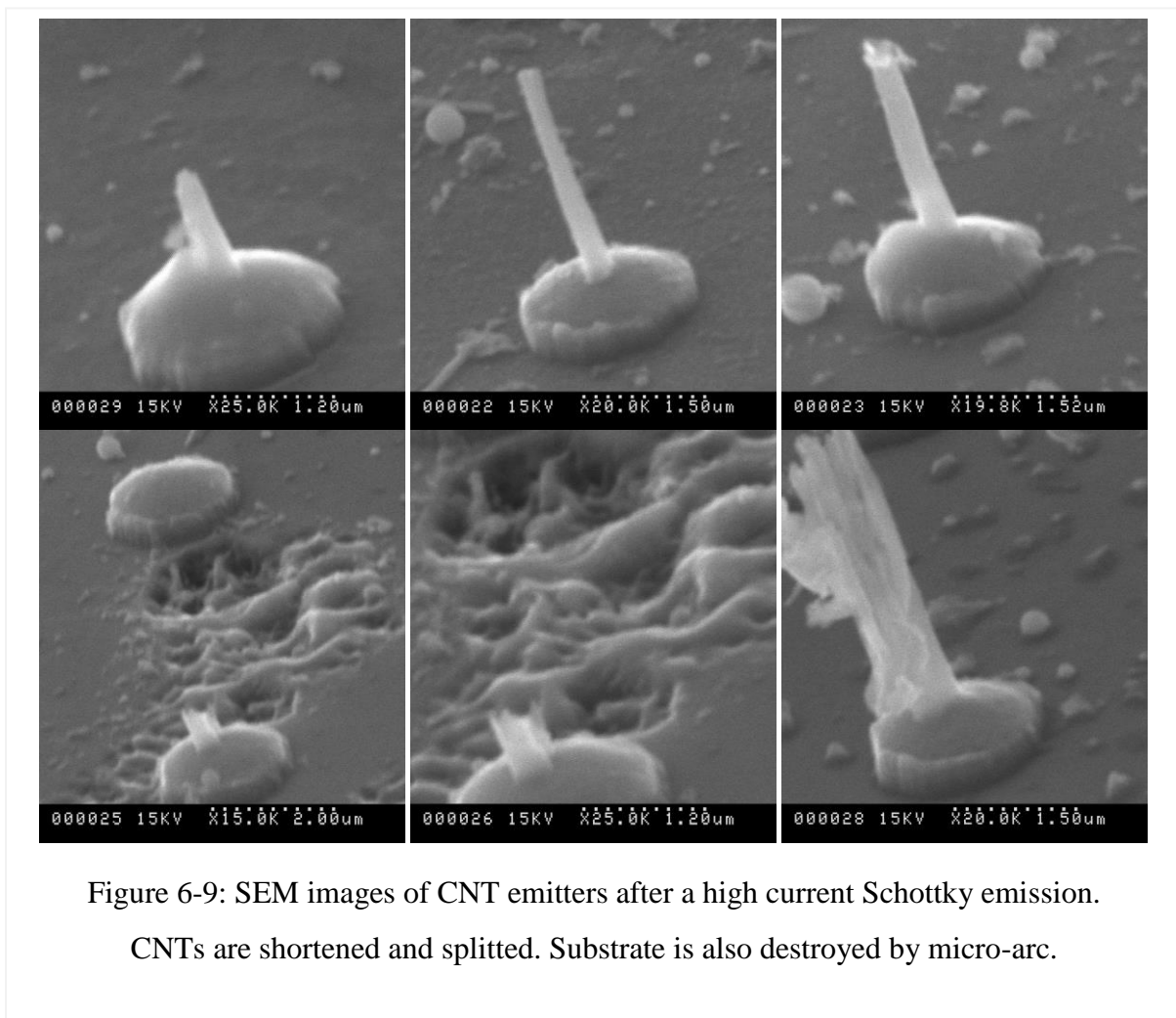
Figure 6-9: SEM images of CNT emitters after a high current Schottky emission. CNTs are shortened and splitted. Substrate is also destroyed by micro-arc.

shorten, and the emitters are not removed from the bottom, we believe the substrate melting of the emitter is avoided. Average emission current is 0.9 µA/CNT, which is higher than the average emission current of an emitter array have been reported in the literature. Although the CNT samples still can provide an emission current about 1.6mA after the Schottky emission experiment, some CNT emitters are destroyed. Therefore, lifetime of the CNT emitter in the Schottky emission regime is at minute scale. We believe better vacuum may solve this problem, but more studies of improving the emitter lifetime are needed.

6.3 Field Emission from Gated Ballasted CNT Array

Gated field emission cathode has many applications, for example, field emission display, travel wave tube, and addressable X-ray beam array for stationary CT scanner. These devices equip an addressable gated emission cathode array or a single gated emission cathode. A triode structure is adopted. The device consists of a grounded cathode, an anode connected to a high voltage, and a gate electrode. Compare to the mesh gate of thin film emitters, which has a gate-emitter gap of 100 µm and gate voltage over one thousand volts, the cylinder shape gate has a sub-micron gate-emitter gap, therefore, the gate voltage is lower than 100 volts. It has been reported that with a gate-emitter gap of 80 nm, the gate voltage is just 10 V [44]. This voltage is compatible to CMOS circuit; therefore, the control circuit of the device can be simplified and minimized significantly.

The sample is tested in a vacuum chamber with a base pressure of 3×10^{-8} Torr. A 6 µm thick silver foil anode is mounted few millimeters apart from the sample and a 1000 V voltage is applied. A sweep voltage is applied on the gate electrode to generate an emission current. The CNT emitter is grounded through a picoammeter to measure the emission current. The current versus gate voltage curve is shown in Figure 6-10. In the first round, the
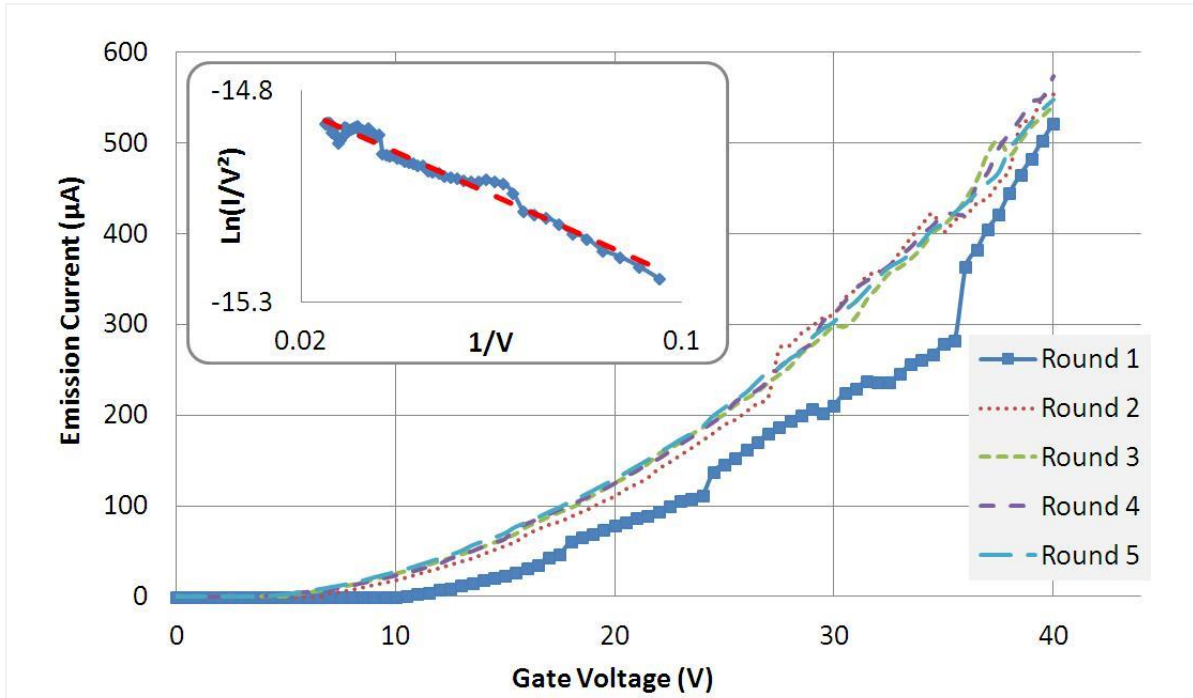
Figure 6-10: Emission current versus gate voltage. Insert shows the F-N plot
of the average current.

emission current achieves 521 uA at 40 V. In the following rounds, the emission currents,

range from 540 uA to 570 uA at 40 V, are higher than that of the first round. We believe this

current increase is caused by the annealing process during the first round and the removal of

the residual gas molecular from the emitters. In the following rounds, the emission current

has a good repeatability indicates the emitter array has a good stability under this working

condition. The Fowler−Nordheim plot of the average emission current is shown in the inset

of Figure 6-10.

Due to the existence of the ballast resistor, the emission current lead to a voltage

increase at the emitter tip. As a result, the effective voltage between the emitter tip and the

gate electrode decreases. From the fabrication parameter, the resistance of the ballast resistor

under each CNT emitter is about 50 MΩ. The emitter array has 2,121 emitters and the total

emission current is about 550 uA. The average current is 0.26 uA/CNT. The voltage drop on
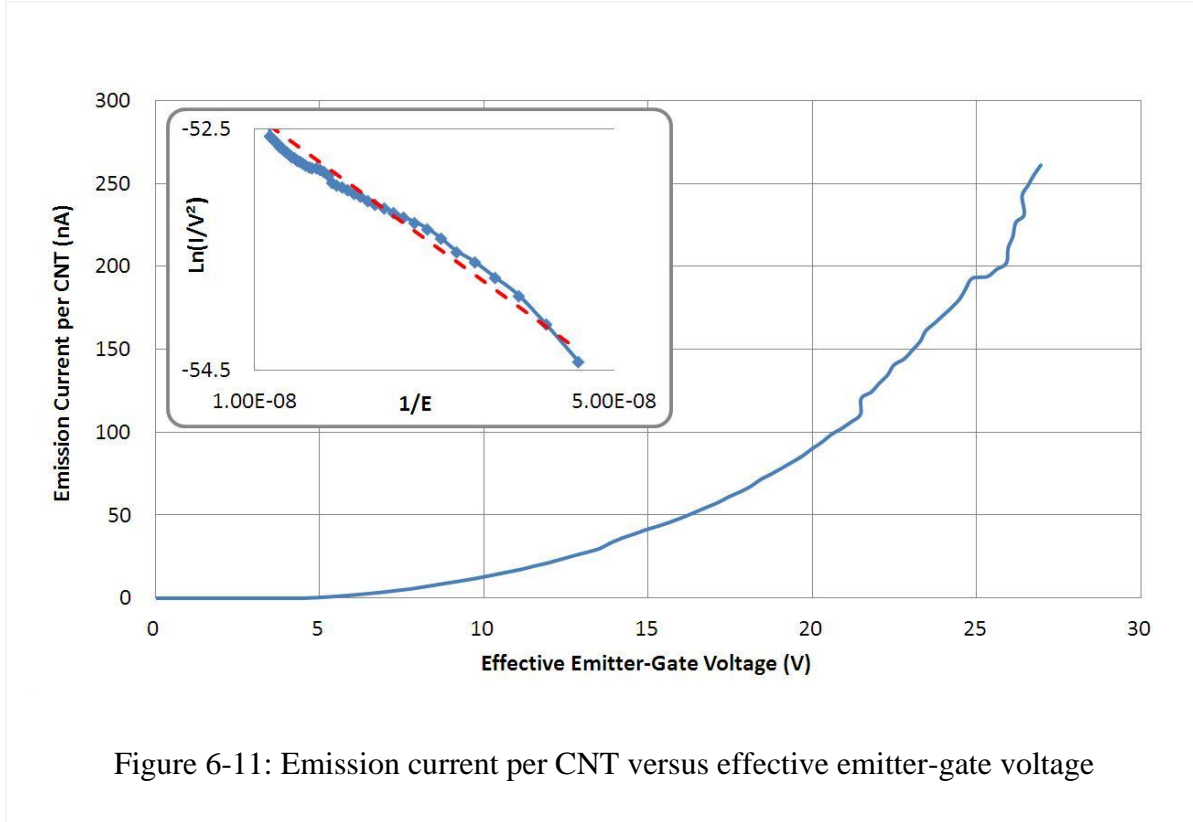
Figure 6-11: Emission current per CNT versus effective emitter-gate voltage

the ballast resistor is about 13 V. Thus, the effective voltage, the voltage between the emitter

tip and the gate electrode, equals gate voltage subtract the voltage drop on the ballast resistor.

The emission current versus the effective voltage curve and the corresponding F-N plot are

shown in Figure 6-11. F-N plot of high voltage segment is shown in the inset of Figure 6-11.

The slope and intercept of the trend line of the F-N curve (red dash line in inset of Figure 6-

11) is 5×10^7 and -51.84. From the F-N theory, the field enhancement factor β of individual

CNT is 1392 and the average effective emission area of individual CNT is 0.47 nm².

Therefore, the radius of the emitter apex is 0.7 nm. The field enhancement factor of the entire

CNT array emitter is $\beta = 696$. This value has a good agreement with the non-gated CNT

emitter array. Therefore, we believe the CNT emitters have the same field emission

properties in a diode configuration or in a triode configuration. Figure 6-12 shows a current

versus time curve of a long term stability experiment. The sample has not been annealed

94

before the experiment. Inset of Figure 6-12 shows the emission current during the first two hours. In the first ten minutes, the emission current has a slight increase. After ten minutes,
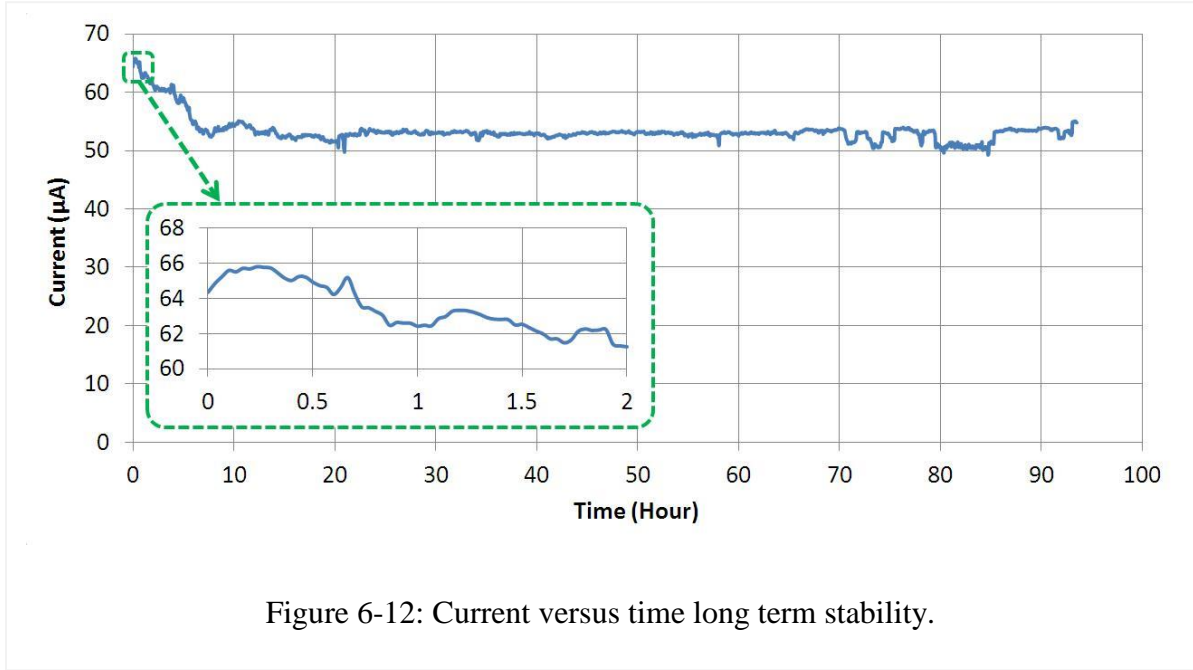
Figure 6-12: Current versus time long term stability.

the current decreases from 66 µA to 52 µA and becomes stable after 10 hours. The fluctuation of the emission current between 30 hours to 50 hours is 3.2% (range from 51.7 µA to 53.4 µA).   In previous achievements, CNT emitters show 5% emission current fluctuation under constant voltage mode [151], or 13% voltage increase under constant current mode [152]. When compared to these results, our CNT emitter has a lower fluctuation and better long term stability.

In our fabrication process, the emitter-gate gap is determined by the thickness of the silicon dioxide insulator layer. The insulator layer is deposited by PECVD. In a certain working condition, the thickness of the silicon dioxide layer is proportional to the deposition time. With a slow deposition rate and an over ten minute deposition time, the insulator layer has a good quality and the thickness can be controlled at nano-meter scale. From Figure 5-6F, we can see the diameter of the cylinder shape gate is about 800 nm, and the emitter-gate

gap ranges from 200 nm to 300 nm. This emitter-gate gap is much smaller than that of the gated CNT film emitter and the Spindt cathode. As a result, the control voltage of our emitter is much lower than that of other gated CNT field emitters.

6.4 Chapter Summary

In this chapter, field emission of gated and non-gated CNT emitter array has been described. Field emission current density and stability is measured. The emission current about 600 µA is obtained from both the gated emission cathode and non-gated emission cathode. Even though the desired emission current (1 µA/CNT) is not achieved, the results of our samples (0.3 µA/CNT) are much higher than other CNT emitter arrays. When the emission current is higher than a threshold value, Joule heating generated on the CNT increases the emitter temperature and changes the emission into Schottky emission regime. The emission current achieves 0.9 µA/CNT. All the above experiment results approves the ballast resistor can improve the emission current uniformity and stability significantly. The cylinder shape gate electrode shows good performance as well.

Chapter 7
PMMA based Field Emission Microscope

7.1 Introduction

To study the distribution of the emitted electrons and the emission uniformity, Field emission microscopy (FEM) is adopted. We studied the structures of conventional FEMs and found it is not suitable for field emission arrays. Therefore, we designed a new FEM to investigate the field emission property of field emission arrays.

FEM has been used to investigate molecular surface structures and their electronic properties on the basis of the difference in work function of the various crystal facets on the surface [153]. Theoretical and experimental studies show FEM can achieve a resolution as high as 0.3 nm approximately, and has the capability of showing images of individual atoms at the cathode tip [154-156]. A conventional FEM consists of a conducting fluorescent screen anode and a cathode with a sharp tip. Although a conventional FEMs' cathode-anode gap of 5 cm to 8 cm leads to a spatial magnification about 10^5 to 10^6, the conventional FEM suffers from two shortcomings. Firstly, fine structure is not visible on a fluorescent screen, because of the lack of homogeneity of the screen [157], which inhibits the observation of small differences in light intensity. Secondly, the fluorescent screen has low phosphor efficiency and low sensitivity to low energy electron beams, because a large fraction of the beam energy is lost outside the phosphor [109].

In contrast to a fluorescent screen, Poly (methyl methacrylate) (PMMA) is highly sensitive to electron beams and is widely used as an electron beam resist in electron beam lithography. Because the effect of electron beam to PMMA is accumulated over time, we used electron beam dose (Charge/Area) to describe the effect of an electron beam to a

PMMA film. A PMMA film has two interesting properties. Firstly, a PMMA thin film acts as a positive resist when exposed to a low electron beam dose (5-20 μC/cm² for 1 KeV beam) [158], but acts as a negative resist when it is exposed to a high dose (2000 μC/cm² for 1 KeV beam) [158, 159]. Thus, it is possible to record the spatial distribution of an electron beam as well as distinguish a wide range of dose intensity. Secondly, the PMMA film is more sensitive to low energy electron beams than to high-energy beams, because the electron energy deposition in PMMA is more efficient at low electron beam acceleration voltages [160]. In other words, by decreasing the cathode-anode voltage of the FEM, the amount of electrons required to record the field emission patterns on the PMMA film is decreased.

In most cases, field emitters used in conventional FEM has just one emission site. In an emission array, electron beams electron beams are dispersed. The high magnification makes the electron beams overlapped. As a result, FEM images from individual emission site cannot be distinguished. By using the new image recording material, the cathode-anode gap can be decreased to tens micro meter scales, the corresponding anode voltage and magnification are decreased. This low voltage FEM image shows many details of the electron beams that have not been reported before.

7.2 Field Emission Microscope Setup

The experimental setup adopts a simple diode configuration shown in Figure 7-1A. An 80 nm thick PMMA thin film is spin-coated onto a silicon substrate as the anode. A vertically aligned ZnO nanowire thin film grown on ITO coated glass substrate is used as the cathode. A 50μm thick PTFE spacer is sandwiched between the cathode and the anode. When compared to conventional FEMs, the cathode-anode gap of the experimental setup is reduced to 50μm to decrease the cathode-anode voltage and avoid the overlap of patterns of
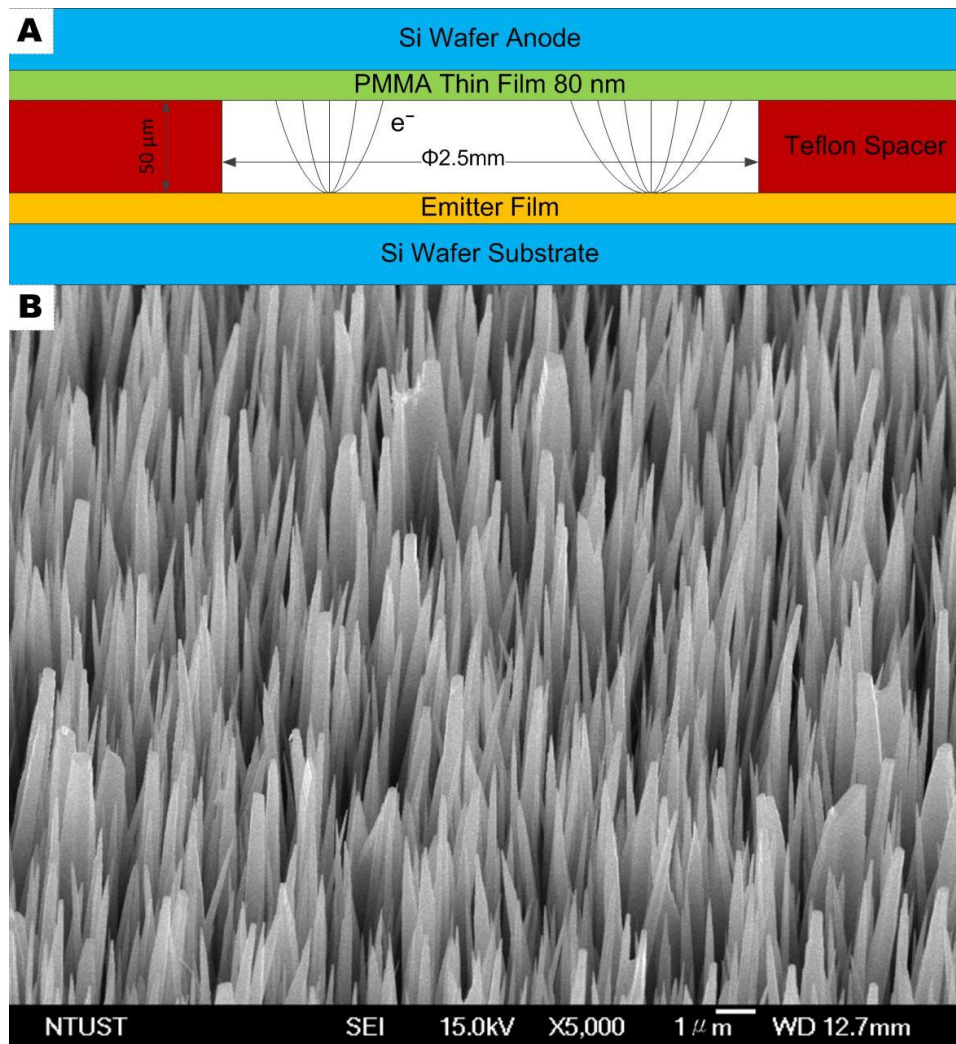
Figure 7-1: Diagram of FEM experimental setup (upper) and SEM
image of tested ZnO thin film cathode (lower)

adjacent emission sites. The sample is placed in a vacuum chamber with a pressure of 5×10^{-8}

Torr. A picoammeter is used to monitor the emission current. Figure 7-1B shows a SEM

image of the ZnO thin film cathode. First, the current versus voltage property of the sample is

measured (Figure 7-2). F-N plot of the sample is shown in inset of Figure 7-2. From the F-N

theory, the field enhancement factor is β=2320. Then a constant voltage is applied on the

anode for several hours to collect the FEM images.

99
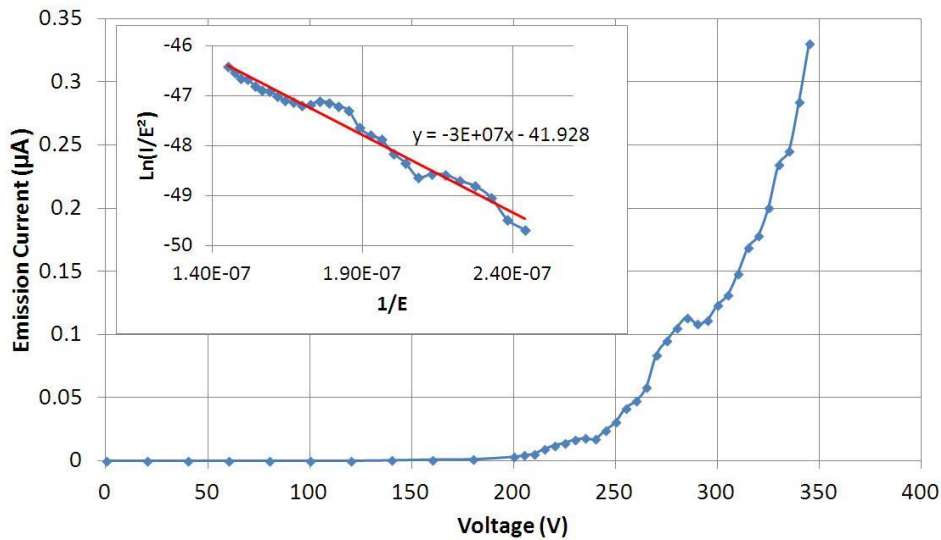
Figure 7-2: Current versus voltage curve and F-N plot of the FEM experiment

After exposure to field emission electron beams, the PMMA has three possible states: (i) unexposed original PMMA; (ii) PMMA that is exposed to low electron dose (positive resist); and (iii) PMMA that is exposed to high electron dose (negative resist). The development of PMMA involves two steps. The first step is to develop PMMA in a PMMA developer (3:1 IPA: MIBK) for 60 seconds, rinse in IPA for 30 second and then blow dry. This step removes the PMMA, which is exposed to low electron dose. The second step is immersing the developed PMMA in acetone to remove the unexposed PMMA while leaving the high dose exposed PMMA intact.

7.3 Field Emission Microscope Images

The exposed PMMA film is observed under an optical microscope before the exposed PMMA film is developed to remove the positive resist. Two defect sites on the PMMA film are clearly visible in Figure 7-3A. The defects have a one-to-one correspondence to emission sites on the thin film emitter [161]. These defects indicate that the emission current is
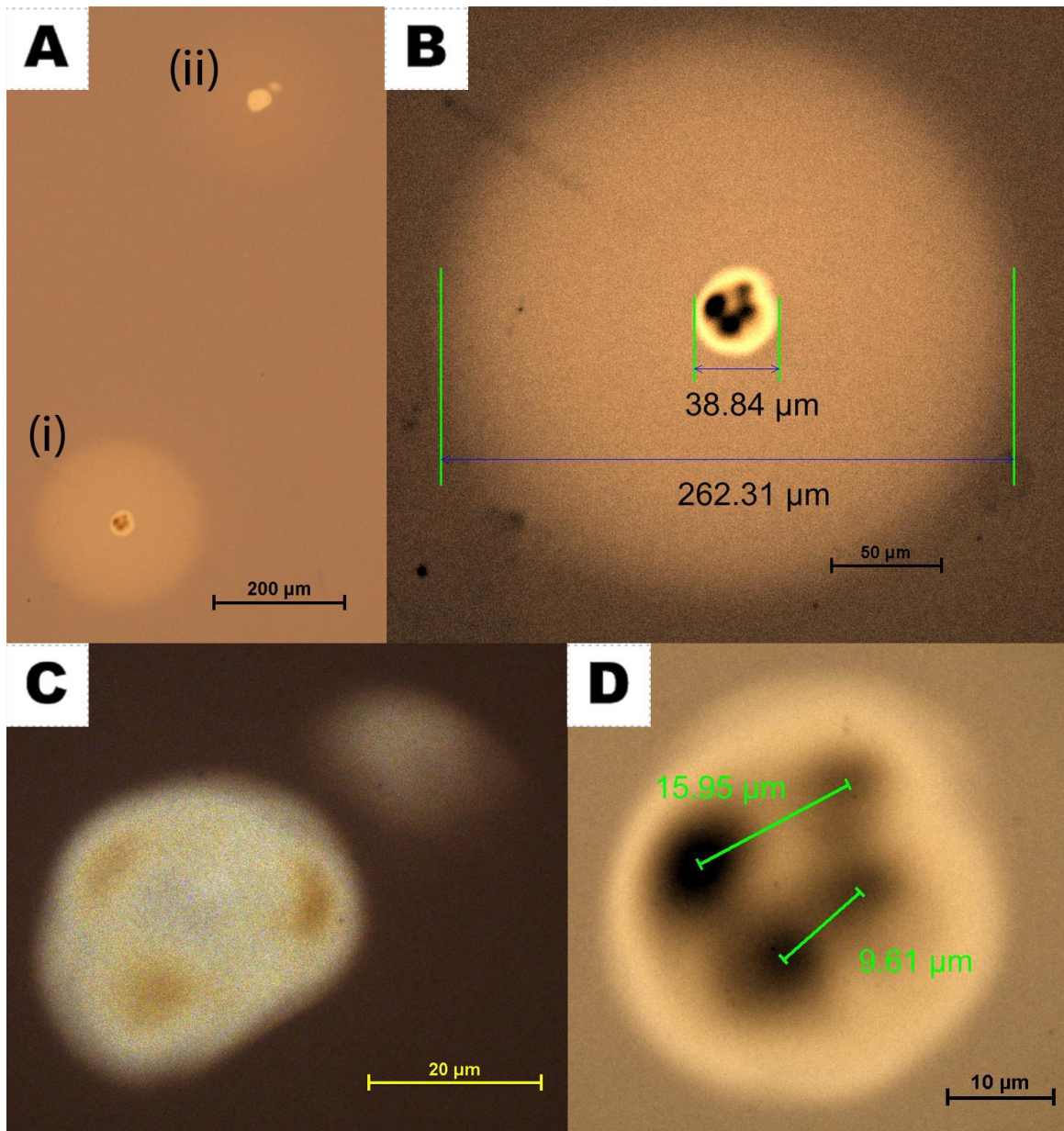
Figure 7-3: Optical image of the PMMA film before development. Two defect sites (i) and (ii) (upper left); expanded view of defect site (i) (upper right); expended view of defect site (ii) (lower left) and (i)'s (lower right) center rings showing some dark spots
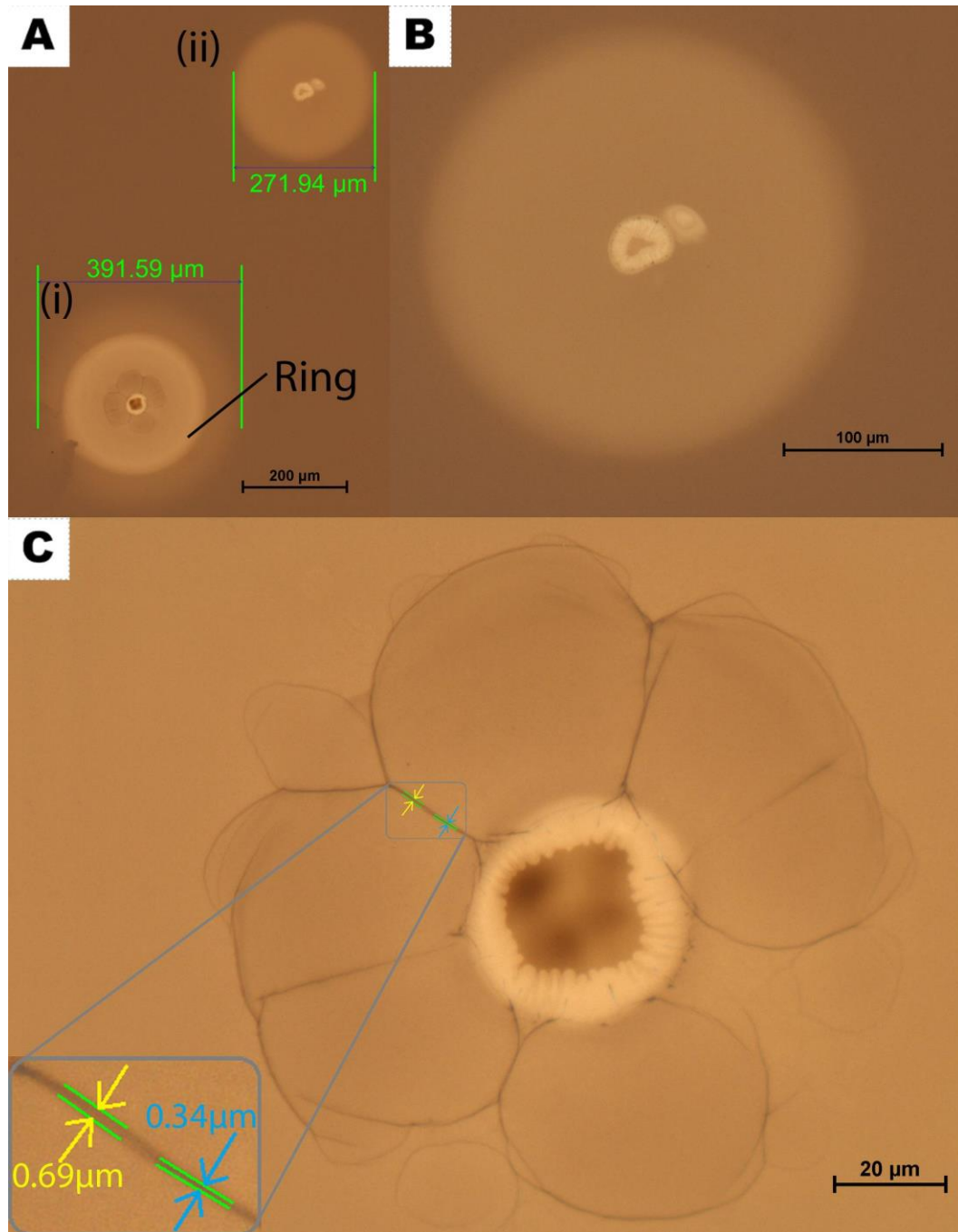
Figure 7-4: PMMA film after first development step. Large circular rings appear on each defect site, the diameters are about 391 μm and 272 μm (upper left); expanded view of site (ii) (upper right); expanded view of center ring of site (i) (lower), where images of six "petal" shape geometry appear; insert shows the width of the lines is between 0.34 μm and 0.69 μm.

contributed by two main emission sites. Figure 7-3B is a zoomed up view of defect site (i), which has two concentric rings: an inner ring about 39 μm in diameter, and an outer ring about 262 μm. Figure 7-3C is an expanded view of defect site (ii), which has two separate rings: one larger ring with three faint dark spots, and the other smaller ring. Figure 7-3D, a farther expanded view of the defect site (i), shows four dark spots. These dark spots are similar to the cloverleaf patterns that emerge in conventional field emission microscopy studies [162].

Figure 7-4 shows images of the PMMA film after the first development step that eliminates the positive resist. A large circular ring is observed around each defect site that was not as clearly observable before the development. The diameter of the defect sites (i) and (ii) are 391 μm and 272 μm respectively. The fact, that the radius of the circular defect sites is several times bigger than the 50 μm cathode-anode gap, indicates that the electron beam is widely emanative. A ring pattern with a diameter of ~260 μm is visible on the defect site (i). Similar ring patterns have been observed in carbon nanotube field emission [163-165]. In addition, Figure 7-4C clearly shows the outlines of six "petal" shape facets. The ZnO nanowire has a wurtzite structure, therefore we believe the six "petals" correspond to the six crystal facets below the top facet of the ZnO. Smaller "lobes" of the facets next to the main "petals" are also visible in Figure 7-4C. Inset of Figure 7-4C shows the width of the "petal" boundary is about 0.34-0.69 μm. These images of the crystal facets of ZnO emitter indicate that electrons are emitted not only from the center or top crystal facet of the emission site, but also the crystal facets neighboring to the center facet, and the emitted electron density at the boundary of the facets are significantly different from the center of the facets. The field emission pattern reflects the change of work function or electrical field strength of the

Figure 7-5: Qualitatively identify electron dose of defect (i). Dose test result of electron beam lithography facility (upper); and distinguish the dose of the defect (i) (lower); inset shows an image with enhanced contrast of the defect (i) after immersed in acetone, only center ring and part of the "petal" boundary are remained
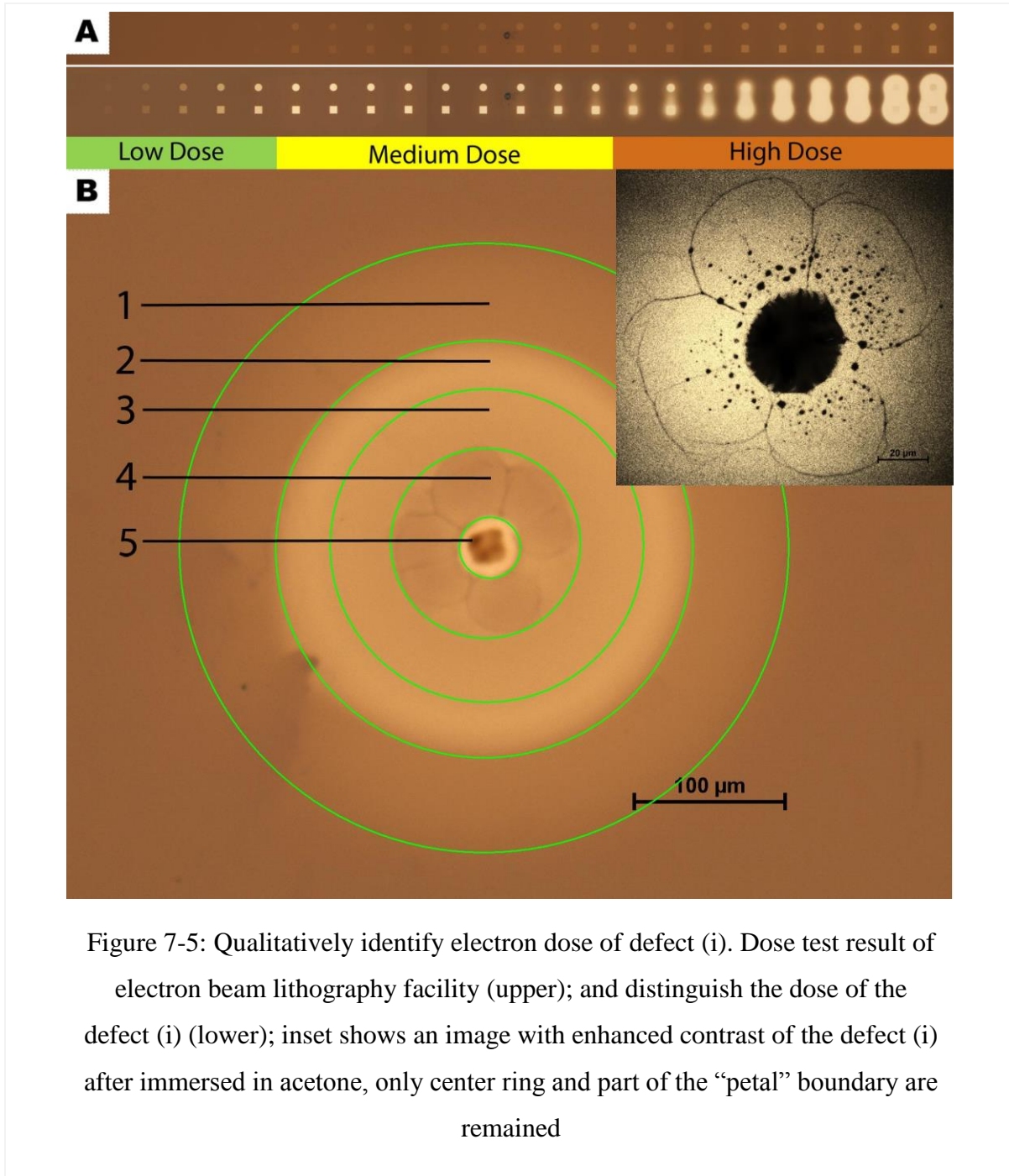
emission site, therefore, either or both of them have a remarkable change at facet boundaries.

The electron beam exposed and developed PMMA film is then immersed in acetone to remove the unexposed PMMA. Insert of Figure 7-5B shows a contrast enhanced image of the defect (i), in which only the center ring of the defects and part of the "petal" boundary are

remained. This indicates that only the PMMA at the center ring and the "petal" boundary are transformed into a negative resist. The other areas are not exposed to enough electron doses to perform this transformation. The "petal" boundaries are intermittent and not clear after immersion in acetone denoting the electron dose of the boundaries is higher than that of the center of the "petals" but lower than the center ring of the defect site. The dose at the center ring of the defect and the "petal" boundary is at least several tens of times higher than that of the other areas.

To qualitatively demonstrate the relationship between the exposure dose and optical images on PMMA film, a dose test is preformed in an electron beam lithography facility. A serial of patterns with an increasing dose is written on a PMMA film. Figure 7-5A shows the result of the dose test. The top row shows the PMMA film before the development stages, and the bottom row after. Before development, low dose patterns are not visible. With the increase of the dose, the patterns become more and more clear. After development, the low dose patterns emerge; medium dose patterns become clearer than before, and the boundary of high-dose patterns becomes blurred. Figure 7-5B shows the defect site (i), after removing low-dose exposed PMMA, consist of five concentric circular dose ranges. The dose of each ring correspond to the dose range 1 to 5 marked in the Figure 7-5A. The outermost ring receives the lowest dose (range 1) and the center ring receives the highest dose (range 5). However, the dose of the second outer ring (range 3) is higher than the next inner ring (range 2). We believe this is caused by the distortion of mapping the 3D structure into flat image. Further investigation is still needed to address it.

In the FEM image, the center area of the defects (i) has much higher electron does than the other defect areas; therefore, we used this size to calculate the magnification. The

diameter of the center ring of defect (i) is 38.84 μm and the effective emission site radius is 60 nm. Thus, the magnification of the center area of the FEM image is about 323.

In our experiments, the emission current is controlled at a very low level (below 1 nA), which can effectively avoid heating of the emission tip and decrease the density of emission sites. On the other hand, a low magnification can reduce the size of the images. As a result of the low emission site density and small image size, the overlap of the image is effectively avoided. Among our experiments, center ring over lapping is observed at an emission current close to one mA and the outer ring over lapping at a μA scale.

7.4 Discussion

In conventional FEM, the magnification (normally 10^5 to 10^6) is estimated by the ratio of tip-screen distance (5cm to 8cm) to tip apex radius (several tens nanometer) and is not affected by the applied anode-cathode voltage. In our experimental setup the cathode-anode gap is just 50 μm, thus the magnification at the center area is between several hundreds to few thousands. However, the image is a 2D mapping of a 3D structure and the distance from the emitter tip to the image center is much smaller than to the image edge, thus the magnification is not uniform. It is lower at the image center but higher at the image edge. A reconstruction algorithm is needed to calculate a local magnification relative to the center magnification and reconstruct the 3D geometry of the emission tip. On the other hand, in Figure 7-4C the width of the lines at the 'petal' boundary is 0.34 μm to 0.69 μm. Based on the estimated magnification, the actual size of the facet boundary is at sub-nanometer scale, close to the highest theoretical resolution (0.3 nm) of FEM [156].

The clear boundary of the "petal" indicates that most of the electrons have a certain emission angle to the facet, instead of in a random direction. In addition, there is a significant change at the boundary of the crystal facets of either work function or electric field strength.

Since the emitters in the cathode film have a similar height and dimension, a slight difference during the sample assembling may lead the emergence of 'hot' emitters that are specific for each test. As a result the images of the emission site are different, even with the same sample. Although the same image cannot be repeated, the significant characteristics remain the same. For example, the center ring appears in every test and the sizes are all very close to 40 µm; the outer ring with a diameter about 260 µm appears in almost all tests; and the most important thing is the fine lines in the surrounding area of the center ring appears in different tests. This characteristic proves our FEM have the capability of capture the details of field emitter tip geometry. However, the capability of pick out the specific emitter in different tests is still desired for further studies.

7.5 Chapter Summary

A PMMA thin film based FEM has been successfully used to study a ZnO nanowire thin film field emitter. The images of the PMMA film have a high resolution. Details of the centre structure and the clear "petal" shape boundaries of crystal facets, reported in this chapter, have not been shown previously. The two-step electron beam resist developing process makes it possible to distinguish the electron beam dose qualitatively. In future studies, a PMMA dose index will be necessary to quantify the electron beam dose to the exposure rate for consistency, and a method of locating the emission sites on the thin film emitter corresponding to the defect sites will be an asset to characterize the field emission property of thin film emitters. Compare to the conventional FEM, our setup lacks the

capability of capturing time evolution images. However, it has the strength of recording fine details of the emission images, which is not achievable to the conventional FEM. Thus our FEM is a complementary to conventional FEMs.

Chapter 8
Field Emission based X-ray Tube

8.1 Review of Conventional X-ray Source

A conventional X- ray tube comprises a metal filament or a film cathode that emits electrons when heated to over 1700 K and a metal target (anode) that emits X-ray when bombarded by accelerated electrons which emitted from the cathode. The drawbacks of the thermal cathodes are their slow response time, high energy consumption, high operating temperature and essentially all current commercial X-ray tubes are single-pixel devices where X-rays are emitted from single focal spots on the anodes. The conventional X-ray cathode, either thermionic cathode or Schottky cathode, works at the high temperature over 1700 K, which is generated by a filament. The filament needs a certain time to heating up and cooling down. As a result, in a conventional X-ray tube, the beam is controlled by turn on and off the high voltage. This design increases the complexity of the control circuit and lead to a slow response time. Furthermore, due to the thermal radiation, even a thermionic emission array is made, the pitch between emitters cannot be very small. In contrast, field emission cathode has a high response time. It can works at terahertz scale without an extra beam shutter and the pitch of field emitter can be as small as several tens micrometer [129]. The conventional X-ray cathode is made with conventional machining technology. The height of the filament is several millimeters. On the other hand, field emission cathode is made with modern micro-fabrication technology. The thickness of the emitter is just several microns. As a result, the field emission cathode is a solid-state device and has a much better mechanical strength and vibration resist. The high temperature during the emission leads to an evaporation of the filament. As a result, the emission cathode will exhaust after several

thousand hours of operation. On the other hand, field emission cathode works at a low temperature, the cathode material is not consumed. Therefore, the field emission cathode has a longer lifetime than that of other electron emission cathodes.

In conclusion, when compared with conventional X-ray sauces, field emission X-ray has many advantages: 1) a longer lifetime; 2) working at room temperature avoid of thermal radiation; 3) fast response time; 4) smaller focal spot size; 5) smaller size, higher mechanical strength and vibration resist. Furthermore, field emission cathode makes flat panel X-ray, tiny X-ray tube, 2D X-ray array and stationary computed tomography feasible.

8.2 Field Emission X-ray Tube Structure

A typical X-ray tube may have a diode structure or a triode structure. Most of the conventional X-ray tubes used diode configuration, but in some applications, for example stationary computed tomography, a fast switch is desired. Therefore, a gate electrode is placed close to the cathode to control the electron beam. The gap between the cathode and the gate is range from sub micrometer to hundred micrometers, the corresponding control voltage range from several tens volts to over one thousand volts [44, 136]. It is obviously that the smaller the cathode-gate gap, the lower control voltage and the simpler the control circuit. Since the conventional X-ray tubes works well in many field, the design of the field emission based X-ray tubes are aimed to some special applications that are not suitable for the thermal cathode X-ray sources, such as tiny X-ray tube, flat panel X-ray source, addressable X-ray beam array, etc.

8.2.1 Diode X-ray Source

In the applications that a fast switching time is not necessary, for example electronic brachytherapy and radiation sterilization, a diode X-ray tube works well. Due to the high
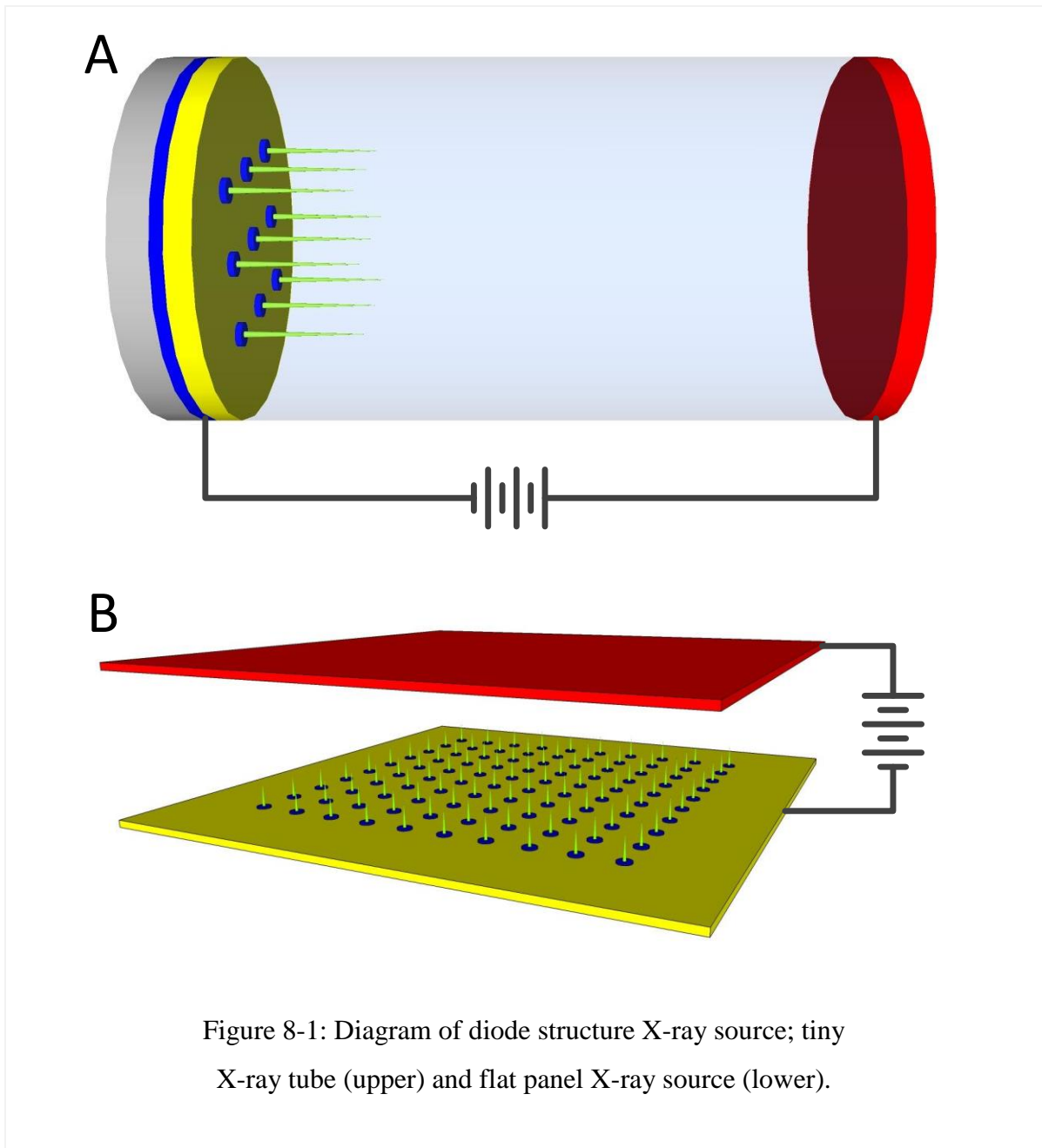
Figure 8-1: Diagram of diode structure X-ray source; tiny
X-ray tube (upper) and flat panel X-ray source (lower).

aspect ratio, CNT cathodes can emit electrons without applying extra energies. Figure 8-1 shows diagram of a tiny X-ray tube and a flat panel X-ray source. Due to the limitation of CNT synthesis devices, a large area CNT cathode has not been fabricated. Small area CNT array cathodes have been tested in a prototype of diode X-ray tube. The base pressure of the vacuum chamber is 5×10^{-8}Torr. The target, a 6 μm thick silver foil, is placed about 7 mm from the cathode. A constant high voltage is applied on the target, and the cathode is
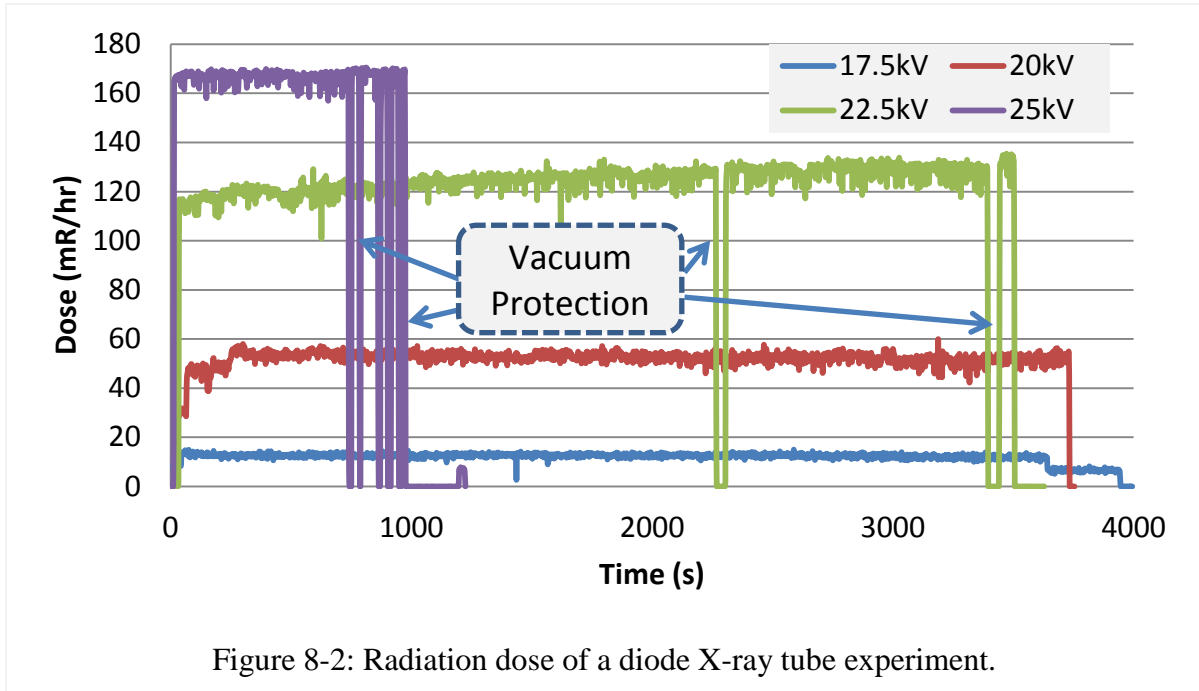
Figure 8-2: Radiation dose of a diode X-ray tube experiment.

grounded. By mounting a radiation dose rate meter outside the X-ray window, the maximum

achievable radiation dose rate is measured. Figure 8-2 shows radiation dose curve of the

following experiments. First, A 17.5 kV constant voltage is applied, and an average 20 μA

emission current is obtained. The corresponding radiation dose is between 13 to 17 mR/hr.

Due to the target outgassing, when a high voltage is applied, the pressure in the vacuum

chamber increases to about 8×10^{-8} Torr. The vacuum pressure decreases back to 5×10^{-8}

Torr in one hour. Target voltage of 20 kV, 22.5 kV, 25 kV, and 27.5 kV voltages are

subsequently applied. The corresponding currents and doses are 25 μA/ 50-55 mR/hr; 35 μA/

120-130 mR/hr; 50 μA/ 160-170 mR/hr; and 65 μA/ 180-185 mR/hr respectively. In the 22.5

kV, 25 kV, and 27.5 kV experiments, the vacuum pressure increases over a threshold

pressure and triggers vacuum protection to cut-off the high voltage. In this process, the

electron beam heats up the anode and releases gas molecules adsorbed on the anode. With the

removal of the adsorbed gas molecules, the X-ray tube power increases and achieves 1.8 W.

At 30 kV, the current is about 90 μA and the tube power is 2.7 W. At this power, outgassing
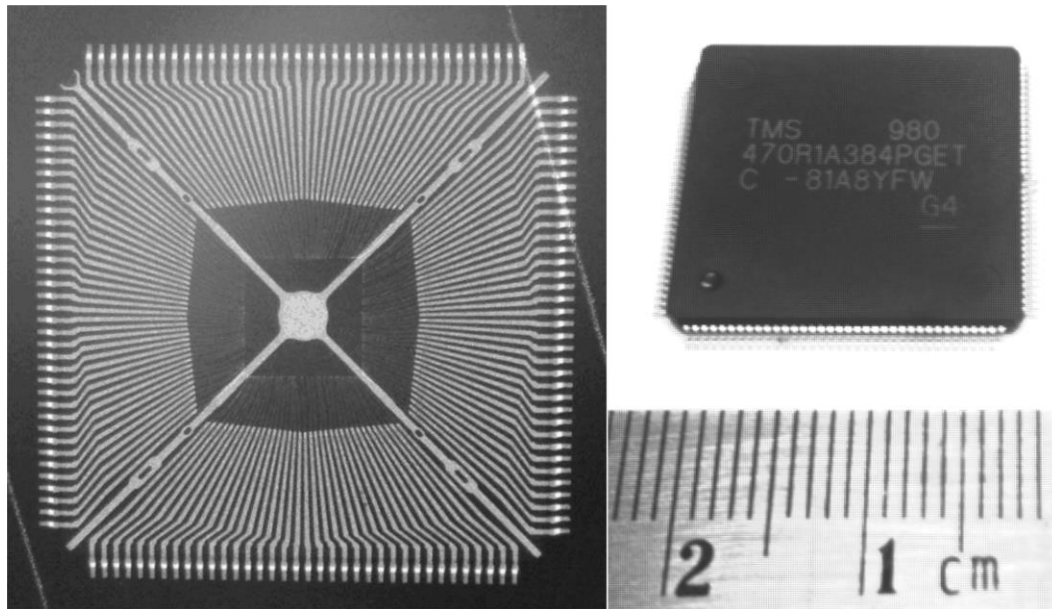
Figure 8-3: X-ray image (left) and optical image (right) of a

144 pin QFP IC
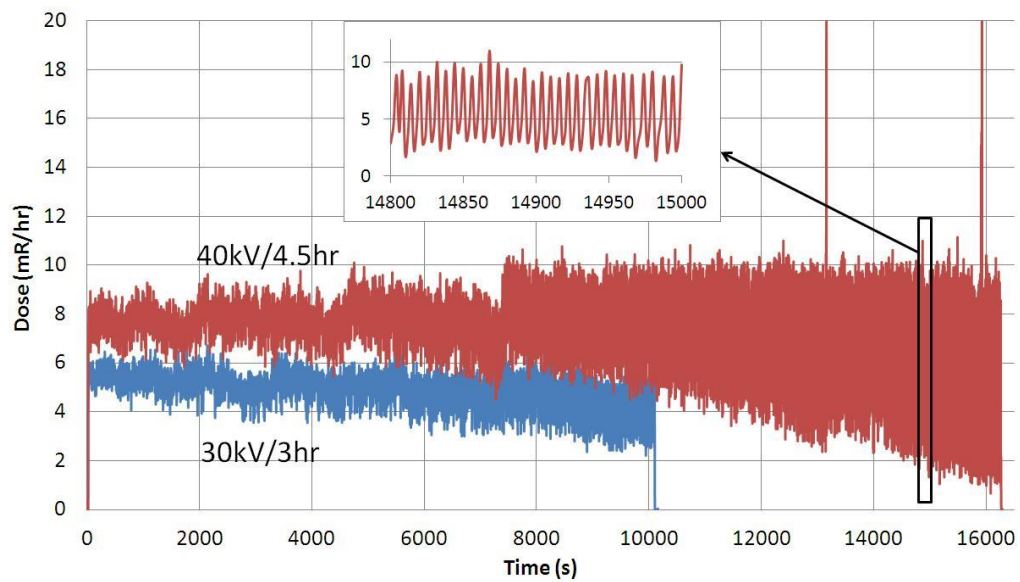
Figure 8-4: Radiation dose of two stability tests.

rate from the anode is too high to be pumped down, so we stopped the experiment at this point. No visible damage to the sample is observed when it is inspected under an optical microscope.

A sample is then tested to take some X-ray pictures. To increase the X-ray beam energy, the target/cathode gap is increased to 9 mm, about 2 mm larger than that of the above experiments; as a result, the operating voltage of this experiment is higher than that of the above experiments. Target voltages of 35 kV and 40 kV are applied, and the current and the power of the tube are about 15 μA/0.525 W, and 20 μA/ 0.8W respectively. X-ray images are taken by a Kodak PPL high speed X-ray film. Figure 8-3 shows an X-ray image of an integrated circuit in a 144 pin Quad Flat Package. The X-ray image is taken at 40 kV for 45 minutes. In this experiment, the electron beam is not focused, and pinhole tests show the spot size is about 2 mm in diameter. Even though the electron beam is not focused, bonding wire of the integrated circuit is still visible in the image. Figure 8-4 shows dose readings of two stability tests taken at 35 kV and 40 kV. In the 35 kV experiment, the dose reading has no noticeable degradation in 3.5 hours. However, at 40 kV, the dose reading starts to diverge range from 2 mR/hr to 10 mR/hr and the average dose decreases from 8 mR/hr to 5 mR/hr. After the sample has been tested for over twenty hours in total, no visible damage to the sample is observed when it is inspected under an optical microscope.

8.2.2 Triode X-ray Source Array

A triode X-ray tube consists of a cathode, a gate, and a target (anode). The cathode is grounded and the target connects to a high voltage range from several kilo-volts to sever hundred kilo-volts. A control voltage is applied on the gate electrode. Figure 8-5 shows a diagram of a triode X-ray source. Gate transmission efficiency is defined as the anode current
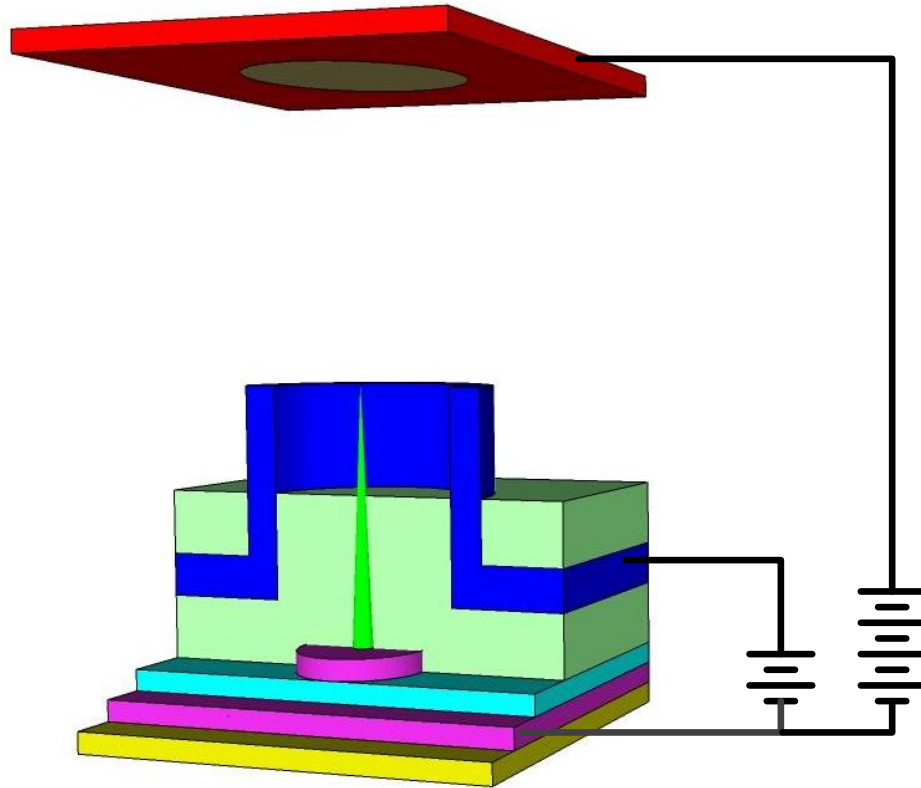
Figure 8-5: Diagram of triode X-ray tube

over the emitter current, and describes the percentage of emitted electrons that can reach the anode. High gate transmission rate is one of the biggest advantages of the Spindt cathode. It has been proved that the gate transmission efficiency of Spindt cathode can be 99%. Our emitter has the similar structure to Spindt cathodes. Therefore, the gate transmission efficiency of our design should be in the same order of Spindt cathodes. To achieve a scanning X-ray beam, an addressable cathode array is desired. The cathode array consists of a set of bottom column electrodes, a set of top row electrodes, and emitter arrays in between. When a column signal activates a single conductive strip within the grid, while a row signal activates a conductive strip within the emitter base electrode, at the intersection of an

115
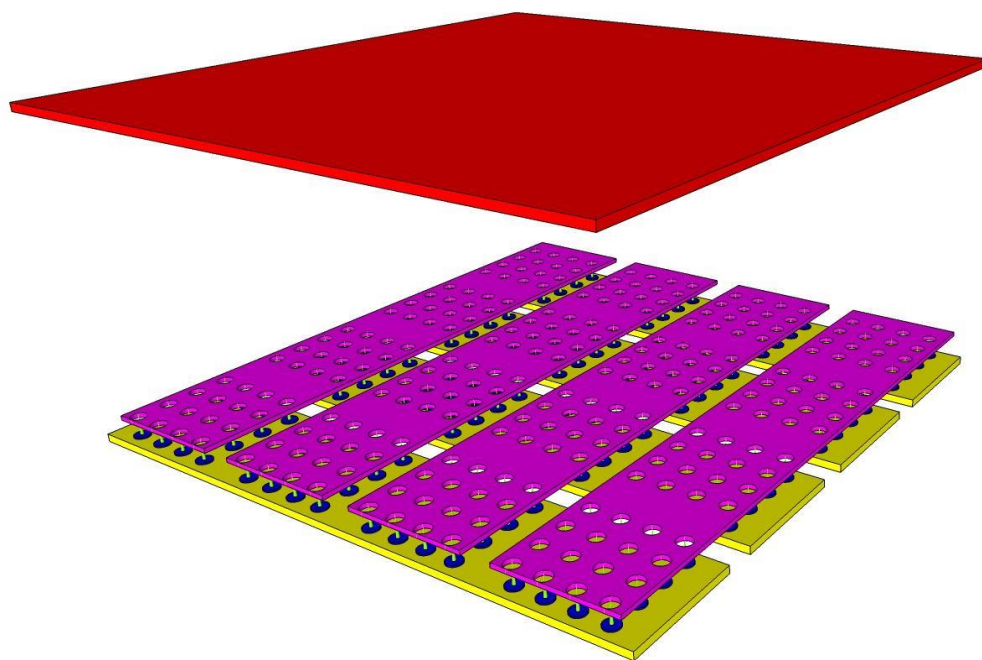
Figure 8-6: Diagram of an addressable multi-pixel X-ray source for applications such as stationary CT scanner.

activated column and an activated row, a gate-to-emitter voltage differential is sufficient to induce field emission, while other emitters are not emitting. Figure 8-6 represents the contemporary architecture. Each row-column intersection is corresponding to a single pixel of the X-ray beam array.

8.3 Flat Panel X-ray Tube

In a conventional CT scanner, besides the mechanical challenge, power density of the X-ray sources is another obstacle. For a body CT, approximately 250 mAs (i.e., tube current in milliamps times scan time in seconds) per slice are required. For a 20ms scanning time (no motion artifact cardiac scan), the required tube current is 12.5 Amps. A common target voltage of a CT scanner is 80 kV to 140 kV. The corresponding target power is over 1
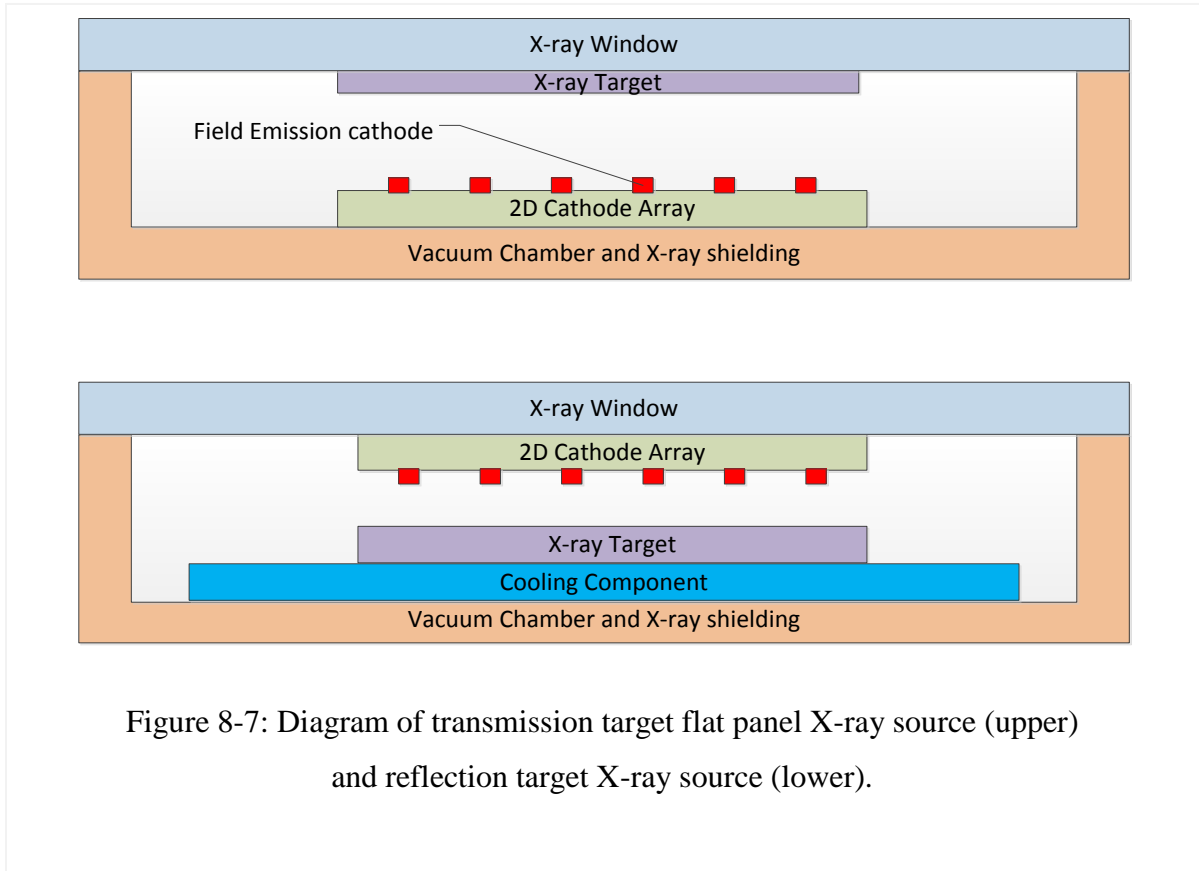
Figure 8-7: Diagram of transmission target flat panel X-ray source (upper) and reflection target X-ray source (lower).

Megawatts, which requires an extremely high cooling capacity to avoid of target melting [166]. One solution to increase the target power density is a reflection target, which is based on the cathode component has a low X-ray absorption. Figure 8-7 shows the diagram of a transmission target X-ray tube and a reflection target X-ray tube. The cathode array is fabricated on a silicon wafer with a thickness of 280 μm. The upper structures are made of aluminum, silicon, silicon dioxide, and carbon. The thicknesses of the layers range from 200 nm to 500 nm. The total thickness of the structures is about 2 μm. Due to the low atomic number of the materials used for this fabrication; the X-ray absorption of the cathode is pretty low. As a result, the cathode can be considered transparent to X-ray. Therefore a novel structure of the reflection target is feasible. The biggest advantage of the reflection target is that a cooling component can be mounted on the backside of the target thus increase the power density of the target significantly. On the other hand, a transmission target based

micro-focus X-ray tube has a small focal spot-object distance; therefore, the magnification of the X-ray image is high. Figure 8-8 shows an X-ray image and optical image of an X-ray cathode array. Thin film metal electrodes, CNT emitters, and ballast resistor connection pad is not distinguishable in the X-ray image. This result indicates that the field emission structures on the substrate are transparent to X-ray beam, thus the reflection target X-ray tube is feasible.

8.4 Chapter Summary

Ballasted CNT array based diode X-ray tube has been successfully demonstrated. Triode X-ray tube based on ballasted and gated cathode is still under construction. Reflection target, which have a capability of working under a high power density is proved feasible.

Chapter 9
Contribution and Future Works

9.1 Contributions

This work is motivated by the improving preferences of conventional X-ray tubes when they are used in some specific applications, for example, improve the scanning speed of computer tomography, the simplify the structure of tiny X-ray tube for electronic brachytherapy, and improve the uniformity and power density of flat panel X-ray source. In the past works, field emission preferences of Spindt cathode and CNT film field emitter have been demonstrated. The Spindt cathode has a near prefect gated emitter structure, and the carbon based field emitter has the capability of working in a high vacuum. In this work, we combine the advantages of the structure of Spindt cathode and the material property of CNT. The contribution of this work can be summarized as follow:

- Design and fabricate a connection pad for the ballast resistor in CNT array for the first time. Since the structure and fabrication process of metal cone in Spindt cathode and CNT are essentially different, a component that can provide a uniform size and compatible to the fabrication process of CNT is necessary. Optimization parameter of the connection pad is calculated by numerical simulation.

- Design and fabricate the ballast resistor array under layer in a low density vertically aligned CNT array for the first time. The ballast resistor works as a current limiter on individual CNT emitters to avoid of emitter melting and micro discharge caused by over current. The ballast resistor can improve the emission current uniformity and increases the lifetime of the emitter array.

- Design and demonstrate a ballasted CNT array based diode X-ray tube. The structure of the diode X-ray tube is simpler than the conventional X-ray tubes, and has a lifetime longer than the commercialized tiny X-ray tubes used in electronic brachytherapy. This simple structure is suitable for un-focused applications. But by applying a focusing electrode, a micro-focus X-ray tube is also feasible.

- Design and fabricate a cylinder shape coaxial gate electrode for CNT emitters. The fabrication process of the gate electrode is straight-forward. The emitter is self-centered to the cylinder gate and the apex of the CNT is self-aligned to the top surface of the gate electrode. Simulation results show this structure has the best transmission efficiency.

- Hundred nanometer scale emitter-tip gap is achieved with a simple fabrication process. When compared to the Spindt cathode fabrication process, this structure is much simpler and the quality of the device is guaranteed by the conformal deposition process.

- PMMA based field emission microscopy is designed and demonstrated for the first time. Resolution of this microscopy is 0.3 nm, much higher than a conventional FEM. Details of emission site can be captured. This design can also be used to evaluate the emission uniformity and distribution of emitter electrons from a field emitter array.

- Design and demonstrate the feasibility of reflection target for a flat panel X-ray source. This design has a much higher capacity of power density than a transmission target X–ray tube. Thin film field emission cathode is transparent to X-ray beam, therefore, the X-ray beam intensity is not reduced when passing through the cathode.

9.2 Future Works

The feasibility of making tiny X-ray tube and addressable X-ray array has been proven. But there are still a lot of works to do before it can be commercialized.

- Optimize fabrication process

  Electron-beam lithography can achieve a resolution of few nanometers. However, the process is slow and expensive. To reduce the cost and increase the productivity, nano-imprint is a good alternative of e-beam lithography. Due to a limitation of access fabrication devices, our previous fabrication uses electron beam evaporator to deposit the thin films. This method is slow and limits the maximum thickness. With the extension of the fabrication facility, some new devices are now available. With the access of the new devices, the pervious fabrication process needs some adjustment to achieve a higher productivity and high uniformity. Uniformity of CNT catalyst dot size is critical. Nucleation process of the catalyst dots needs some further studies to improve the CNT uniformity.

- Fabricate field emission cathode array

  To make an addressable X-ray beam array, bottom electrode and top electrode need to be patterned. Photolithography is the simplest process to pattern the electrodes, but it makes the surface of the sample non-flat. If the electrode is patterned before the CNT growth, the non-flatten affects the CNT uniformity. If the electrode is patterned after the CNT growth, the CNTs may be damaged by spin-coating the photo-resist. Laser cutter is a good choice to pattern the electrodes. Some experiments are needed to figure out the best process to pattern the electrodes while do not affect the CNT uniformity.

- Fabricate and test reflection target

Combination of reflection target and transparent cathode has been proved the best structure of flat panel X-ray source and X-ray beam array. By attaching a cooling component on the backside of the target, the power density of the X-ray tube can be increased significantly. Furthermore, the target can withstand high power density makes the X-ray tube have the capability of reduce it focal spot size and increase the image resolution.

9.3 Conclusion

In this dissertation, a CNT based field emission cathode is described. The goal of this work is to develop a field emission based electron source for some specific X-ray applications. Several progresses have been made to improve the performance of field emission cathode. However, there are still a lot of works to do. We believe, with the developing of the supporting technologies and the deep study of this device, some novel X-ray sources can be developed in the near future.

References

[1]   W. K. Rontgen, "On A New Kind of Rays," *Nature,* vol. 53, pp. 274-276, May 1, 1896.

[2]   NASA, "X-Rays ", http://science.hq.nasa.gov/kids/imagers/ems/xrays.html vol. 2012.

[3]   W. Crookes, "On the Illumination of Lines of Molecular Pressure, and the Trajectory of Molecules.," *Proceedings of the Royal Society of London,* vol. 28, pp. pp. 102-111, 1878.

[4]   W. D. Coolidge, "A Powerful R\ontgen Ray Tube with a Pure Electron Discharge," Phys.Rev., vol. 2, pp. 409-430, Dec, 1913.

[5]   W. D. Coolidge, "Cathode-Ray Device," US patent 1211091, 1917.

[6]   Anonymous "Chapter 6 Study Guide " http://whs.wsd.wednet.edu/faculty/busse /mathhomepage/busseclasses/radiationphysics/lecturenotes/chapter6/chapter 6.html vol. 2012, .

[7]   E. C. Beckmann, "CT scanning the early days," Br. J. Radiol., vol. 79, pp. 5-8, 2006.

[8]   M. Rossi, F. Casali, M. Bettuzzi, M. Morigi, D. Romani, S. V. Golovkin and V. N. Govorun, "Experimental micro-CT system for x-ray NDT," pp. 338-348, January 9, 2002.

[9]   L. W. Goldman, "Principles of CT and CT technology," J. Nucl. Med. Technol., vol. 35, pp. 115-28; quiz 129-30, Sep, 2007.

[10]   C. J. Ritchie, J. D. Godwin, C. R. Crawford, W. Stanford, H. Anno and Y. Kim, "Minimum scan speeds for suppression of motion artifacts in CT," Radiology, vol. 185, pp. 37-42, Oct, 1992.

[11]   M. Petersilka, H. Bruder, B. Krauss, K. Stierstorfer and T. G. Flohr, "Technical principles of dual source CT," Eur. J. Radiol., vol. 68, pp. 362-368, Dec, 2008.

[12]   L. W. Goldman, "Principles of CT: multislice CT," J. Nucl. Med. Technol., vol. 36, pp. 57-68; quiz 75-6, Jun, 2008.

[13] P. Raggi, "Imaging of cardiovascular calcifications with electron beam tomography in hemodialysis patients," American Journal of Kidney Diseases, vol. 37, pp. S62, 2001.

[14] A. Tingberg, "X-ray tomosynthesis: a review of its use for breast and chest imaging," Radiat. Prot. Dosimetry, vol. 139, pp. 100-107, Apr-May, 2010.

[15] F. A. Vicini, L. L. Kestin, G. K. Edmundson, D. A. Jaffray, J. W. Wong, V. R. Kini, P. Y. Chen and A. A. Martinez, "Dose-volume analysis for quality assurance of interstitial brachytherapy for breast cancer," Int. J. Radiat. Oncol. Biol. Phys., vol. 45, pp. 803-810, 1999.

[16] D. Liu, E. Poon, M. Bazalova, B. Reniers, M. Evans, T. Rusch and F. Verhaegen, "Spectroscopic characterization of a novel electronic brachytherapy system," Phys. Med. Biol., vol. 53, pp. 61-75, 2008.

[17] J. F. Diehl, "Food irradiation—past, present and future," Radiat. Phys. Chem., vol. 63, pp. 211, 2002.

[18] J. H. Park, R. Olivares-Navarrete, R. E. Baier, A. E. Meyer, R. Tannenbaum, B. D. Boyan and Z. Schwartz, "Effect of cleaning and sterilization on titanium implant surface properties and cellular response," Acta Biomater., vol. 8, pp. 1966-1975, MAY, 2012.

[19] L. N. Button, W. C. DeWolf, P. E. Newburger, M. S. Jacobson and S. V. Kevy, "The effects of irradiation on blood components," Transfusion, vol. 21, pp. 419-426, 1981.

[20] E. J. Grant, C. M. Posada, C. H. Castaño and H. K. Lee, "A Monte Carlo simulation study of a flat-panel X-ray source," Applied Radiation and Isotopes, vol. 70, pp. 1658, 2012.

[21] G. Travish, F. J. Rangel, M. A. Evans, B. Hollister and K. Schmiedehausen, "Addressable flat-panel x-ray sources for medical, security, and industrial applications," pp. 85020-85020-13, 2012.

[22] E. L. Murphy and R. H. Good, "Thermionic Emission, Field Emission, and the Transition Region," Phys.Rev., vol. 102, pp. 1464-1473, Jun, 1956.

[23] S. G. Christov and C. M. Vodenicharov, "On the experimental proof of the general theory of electron emission from metals," Solid-State Electronics, vol. 11, pp. 757, 1968.

[24] R. H. Fowler and L. Nordheim, "Electron Emission in Intense Electric Fields," Proceedings of the Royal Society of London.Series A, Containing Papers of a Mathematical and Physical Character, vol. 119, pp. 173-181, May 1, 1928.

[25] O. W. Richardson, "The Electrical Conductivity Imparted to a Vacuum by Hot Conductors," Philosophical Transactions of the Royal Society of London.Series A, Containing Papers of a Math.Or Phys.Character (1896-1934), vol. 201, pp. 497-549, 01/01, 1903.

[26] I. Langmuir, "The Effect of Space Charge and Residual Gases on Thermionic Currents in High Vacuum," Phys.Rev., vol. 2, pp. 450-486, Dec, 1913.

[27] C. D. Child, "Discharge From Hot CaO," Phys.Rev.(Series I), vol. 32, pp. 492-511, May, 1911.

[28] M. S. Benilov, "The Child-Langmuir law and analytical theory of collisionless to collision-dominated sheaths," Plasma Sources Sci. Technol., vol. 18, pp. 014005, 2009.

[29] H. S. Kim, M. L. Yu, M. G. R. Thomson, E. Kratschmer and T. H. P. Chang, "Energy distributions of Zr/O/W Schottky electron emission," J. Appl. Phys., vol. 81, pp. 461-465, 1997.

[30] Yunkang Cui, Xiaobing Zhang, Wei Lei, Yunsong Di, Mei Xiao, Qilong Wang and Jing Chen, "Thermal-assisted field emission from carbon nanotube cathode," in Vacuum Nanoelectronics Conference (IVNC), 2012 25th International, 2012, pp. 1-2.

[31] K. Junker and K. Heinz, "Experimental examination of the field-enhanced thermal emission of holes in CdS," Physica Status Solidi (a), vol. 21, pp. 451-456, 1974.

[32] R. W. Wood, "A New Form of Cathode Discharge and the Production of X-Rays, together with Some Notes on Diffraction. Preliminary Communication," Phys. Rev. (Series I), vol. 5, pp. 1-10, Jul, 1897.

[33] G. Fursey, Field Emission in Vacuum Microelectronics. New York; Boston, MA: New York : Kluwer Academic/Plenum Publishers, 2005.

[34] R. O. Jenkins, "Field emission of electrons," Reports on Progress in Physics, vol. 9, pp. 177-197, 1942.

[35] G. M. Fleming and J. E. Henderson, "The Energy Losses Attending Field Current and Thermionic Emission of Electrons from Metals," Phys.Rev., vol. 58, pp. 887-894, Nov, 1940.

[36] W. P. Dyke, J. K. Trolan, E. E. Martin and J. P. Barbour, "The Field Emission Initiated Vacuum Arc. I. Experiments on Arc Initiation," Phys. Rev., vol. 91, pp. 1043-1054, Sep, 1953.

[37] W. W. Dolan, W. P. Dyke and J. K. Trolan, "The Field Emission Initiated Vacuum Arc. II. The Resistively Heated Emitter," Phys. Rev., vol. 91, pp. 1054-1057, Sep, 1953.

[38] W. P. Dyke and J. K. Trolan, "Field Emission: Large Current Densities, Space Charge, and the Vacuum Arc," Phys. Rev., vol. 89, pp. 799-808, Feb, 1953.

[39] E. E. Martin, J. K. Trolan and W. P. Dyke, "Stable, High Density Field Emission Cold Cathode," J. Appl. Phys., vol. 31, pp. 782-789, 1960.

[40] W. P. Dyke, F. M. Charbonnier, R. W. Strayer, R. L. Floyd, J. P. Barbour and J. K. Trolan, "Electrical Stability and Life of the Heated Field Emission Cathode," J. Appl. Phys., vol. 31, pp. 790-805, 1960.

[41] C. A. Spindt, "A Thin-Film Field-Emission Cathode," J. Appl. Phys., vol. 39, pp. 3504-3505, June 1968, 1968.

[42] C. A. Spindt, "Field Emission Cathode Structure and Devices Utilizing such Structures," US Patent 3755704, August, 1973.

[43] C. A. Spindt, I. Brodie, L. Humphrey and E. R. Westerberg, "Physical properties of thin-film field emission cathodes with molybdenum cones," J. Appl. Phys., vol. 47, pp. 5248-5263, December 1976, 1976.

[44] C. O. Bozler, C. T. Harris, S. Rabe, D. D. Rathman, M. A. Hollis and H. I. Smith, "Arrays of gated field-emitter cones having 0.32 m tip-to-tip spacing," Journal of Vacuum Science & Technology B (Microelectronics and Nanometer Structures), vol. 12, pp. 629-32, 03, 1994.

[45] F. S. Baker, A. R. Osborn and J. Williams, "The carbon-fibre field emitter," J. Phys. D, vol. 7, pp. 2105-2115, 1974.

[46] F. Reif, Fundamentals of Statistical and Thermal Physics. New York ; Toronto; New York, Mcgraw-Hill (C1965): New York ; Toronto : McGraw-Hill, 1965.

[47] S. Coulombe and J. Meunier, "Thermo-field emission: a comparative study," J. Phys. D, vol. 30, pp. 776, 1997.

[48] J. Paulini, T. Klein and G. Simon, "Thermo-field emission and the Nottingham effect," Journal of Physics D (Applied Physics), vol. 26, pp. 1310-15, 08/14, 1993.

[49] E. Guth and C. Mullin, "Electron Emission of metals in electric fields III The transition from thermionic to cold emission," Phys. Rev., vol. 61, pp. 339-348, MAR, 1942.

[50] W. DOLAN and W. DYKE, "Temperature-And-Field Emission of Electrons from Metals," Physical Review, vol. 95, pp. 327-332, 1954.

[51] W. P. Dyke, J. P. Barbour, E. E. Martin and J. K. Trolan, "T-F Emission: Experimental Measurement of the Average Electron Current Density from Tungsten," Phys. Rev., vol. 99, pp. 1192, 08/15, 1955.

[52] M. Dionne, S. Coulombe and J. Meunier, "Field emission calculations revisited with Murphy and Good theory: a new interpretation of the Fowler-Nordheim plot," J. Phys. D, vol. 41, pp. 245304, 2008.

[53] T. E. Stern, B. S. Gossling and R. H. Fowler, "Further Studies in the Emission of Electrons from Cold Metals," Proceedings of the Royal Society of London.Series A, Containing Papers of a Mathematical and Physical Character, vol. 124, pp. pp. 699-723, Jul. 1, 1929.

[54]   X. Lu, Q. Yang, C. Xiao and A. Hirose, "Nonlinear Fowler–Nordheim plots of the field electron emission from graphitic nanocones: influence of non-uniform field enhancement factors," J. Phys. D, vol. 39, pp. 3375, 2006.

[55]   W. B. Nottingham, "Remarks on Energy Losses Attending Thermionic Emission of Electrons from Metals," Phys. Rev., vol. 59, pp. 906-907, Jun, 1941.

[56]   E. W. Muller, "Work Function of Tungsten Single Crystal Planes Measured by the Field Emission Microscope," J. Appl. Phys., vol. 26, pp. 732-737, 1955.

[57]   L. A. DuBridge and W. W. Roehr, "The Thermionic and Photoelectric Work Functions of Molybdenum," Phys.Rev., vol. 42, pp. 52-57, Oct, 1932.

[58]   F. G. Allen, "Field emission from silicon and germanium; field desorption and surface migration," Journal of Physics and Chemistry of Solids, vol. 19, pp. 87, 1961.

[59]   P. W. May, S. Hohn, M. N. R. Ashfold, W. N. Wang, N. A. Fox, T. J. Davis and J. W. Steeds, "Field emission from chemical vapor deposited diamond and diamond-like carbon films: Investigations of surface damage and conduction mechanisms," J. Appl. Phys., vol. 84, pp. 1618-1625, 1998.

[60]   F. S. BAKER, A. R. OSBORN and J. WILLIAMS, "Field Emission from Carbon Fibres: A New Electron Source," Nature, vol. 239, pp. 96-97, 09/08, 1972.

[61]   E. Braun, J. Smith and D. Sykes, "Carbon fibres as field emitters," Vacuum, vol. 25, pp. 425-426, 1975.

[62]   H. W. Kroto, J. R. Heath, S. C. O'Brien, R. F. Curl and R. E. Smalley, "C60: Buckminsterfullerene," Nature, vol. 318, pp. 162-163, 11/14, 1985.

[63]   S. Iijima and T. Ichihashi, "Single-shell carbon nanotubes of 1-nm diameter," Nature, vol. 363, pp. 603, 1993.

[64]   S. 1. Iijima, "Helical microtubules of graphitic carbon," Nature, vol. 354, pp. 56-8, 11/07, 1991.

[65]   M. Yudasaka, S. Iijima and V. H. Crespi, "Single-wall carbon nanohorns and nanocones," in Carbon Nanotubes. Advanced Topics in the Synthesis, Structure,

Properties and ApplicationsAnonymous Berlin, Germany: Springer-Verlag, 2008, pp. 605-29.

[66] A. V. Rode, E. G. Gamaly and B. Luther-Davies, "Formation of cluster-assembled carbon nano-foam by high-repetition-rate laser ablation," Applied Physics A, vol. 70, pp. 135-144, 2000.

[67] A. K. Geim and K. S. Novoselov, "The rise of graphene," Nat Mater, vol. 6, pp. 183-191, print, 2007.

[68] Y. Lan, Y. Wang and Z. F. Ren, "Physics and applications of aligned carbon nanotubes," Adv. Phys., vol. 60, pp. 553-678, 2011.

[69] M. Meyyappan, L. Delzeit, A. Cassell and D. Hash, "Carbon nanotube growth by PECVD: a review," Plasma Sources Sci. Technol., vol. 12, pp. 205-216, 2003.

[70] N. Sinha, "Characterization of carbon nanotube based thin film field emitter," 2008.

[71] G. Zhao, J. Zhang, Q. Zhang, H. Zhang, O. Zhou, L. Qin and J. Tang, "Fabrication and characterization of single carbon nanotube emitters as point electron sources," Appl. Phys. Lett., vol. 89, pp. 193113, 2006.

[72] H. Zhang, J. Tang, Q. Zhang, G. Zhao, G. Yang, J. Zhang, O. Zhou and L. Qin, "Field emission of electrons from single LaB6 nanowires," Adv Mater, vol. 18, pp. 87-91, 2006.

[73] H. Zhang, Q. Zhang, G. Zhao, J. Tang, O. Zhou and L. Qin, "Single-crystalline GdB6 nanowire field emitters," J. Am. Chem. Soc., vol. 127, pp. 13120-13121, 2005.

[74] Xia Lian-sheng1, Z. Huang1, Yang Xing-lin1, Pan Hai-feng1 and Liu Yun-long1, "Experimental research on field emission of carbon fiber," High Power Laser and Particle Beams, pp. 685-8, 2007.

[75] W. Zhu, G. P. Kochanski and S. Jin, "Low-Field Electron Emission from Undoped Nanostructured Diamond," Science, vol. 282, pp. 1471-1473, November 20, 1998.

[76] J. C. She, R. H. Yao, S. Z. Deng, J. Chen and N. S. Xu, "Field emission from vertically aligned silicon nanowires," in 2006 19th International Vacuum

Nanoelectronics Conference and 50th International Field Emission Symposium, 2006, pp. 51-2.

[77] J. Ma, J. T. W. Yeow, J. C. L. Chow and R. B. Barnett, "A carbon fiber-based radiation sensor for dosimetric measurement in radiotherapy," Carbon, vol. 46, pp. 1869-1873, 200811, 2008.

[78] S. Kim, J. Yim, X. Wang, D. D. C. Bradley, S. Lee and J. C. deMello, "Spin- and Spray-Deposited Single-Walled Carbon-Nanotube Electrodes for Organic Solar Cells," Advanced Functional Materials, vol. 20, pp. 2310-2316, 2010.

[79] X. Calderon-Colon, H. Geng, B. Gao, L. An, G. Cao and O. Zhou, "A carbon nanotube field emission cathode with high current density and long-term stability," Nanotechnology, vol. 20, pp. 325707 (5pp), 2009.

[80] Z. F. Ren, Z. P. Huang, D. Z. Wang, J. G. Wen, J. W. Xu, J. H. Wang, L. E. Calvet, J. Chen, J. F. Klemic and M. A. Reed, "Growth of a single freestanding multiwall carbon nanotube on each nanonickel dot," Appl. Phys. Lett., vol. 75, pp. 1086-1088, 1999.

[81] M. A. Pasha, A. Shafiekhani and M. A. Vesaghi, "Hot filament CVD of Fe–Cr catalyst for thermal CVD carbon nanotube growth from liquid petroleum gas," Appl. Surf. Sci., vol. 256, pp. 1365-1371, 12/15, 2009.

[82] S. J. Oh, J. Zhang, Y. Cheng, H. Shimoda and O. Zhou, "Liquid-phase fabrication of patterned carbon nanotube field emission cathodes," Appl. Phys. Lett., vol. 84, pp. 3738-3740, May 10, 2004, 2004.

[83] Y. Wei, L. Xiao, F. Zhu, L. Liu, J. Tang, P. Liu and S. Fan, "Cold linear cathodes with carbon nanotube emitters and their application in luminescent tubes," Nanotechnology, vol. 18, pp. 325702 (5pp), 2007.

[84] J. D. Hwang, K. F. Chen, L. H. Chan and Y. Y. Chang, "Using infrared laser to enhance field emission of carbon nanotube," Appl. Phys. Lett., vol. 89, pp. 033103, 17 July 2006, 2006.

[85] Y. Kanazawa, T. Oyama, K. Murakami and M. Takai, "Improvement in electron emission from carbon nanotube cathodes after Ar plasma treatment," Journal of

Vacuum Science & Technology B: Microelectronics and Nanometer Structures, vol. 22, pp. 1342-1344, 2004.

[86]   S. T. Purcell, P. Vincent, C. Journet and V. T. Binh, "Hot Nanotubes: Stable Heating of Individual Multiwall Carbon Nanotubes to 2000 K Induced by the Field-Emission Current," Phys. Rev. Lett., vol. 88, pp. 105502, Feb, 2002.

[87]   Xintek, "Xintek Inc. Field emission cathode," .

[88]   Y. Saito, "Carbon nanotube field emitter," Journal of Nanoscience and Nanotechnology, vol. 3, pp. 39-50, FEB-APR}, 2003.

[89]   S. Wang, X. Calderon, R. Peng, E. C. Schreiber, O. Zhou and S. Chang, "A carbon nanotube field emission multipixel x-ray array source for microradiotherapy application," Appl. Phys. Lett., vol. 98, pp. 213701, 2011.

[90]   J. Prasek, J. Drbohlavova, J. Chomoucka, J. Hubalek, O. Jasek, V. Adam and R. Kizek, "Methods for carbon nanotubes synthesis-review," J.Mater.Chem., vol. 21, pp. 15872-15884, 2011.

[91]   M. Meyyappan, "A review of plasma enhanced chemical vapour deposition of carbon nanotubes," J. Phys. D, vol. 42, pp. 213001, 2009.

[92]   M. Borel, "Electron source with micropoint emissive cathodes and display means by cathodoluminescence excited by field emission using said source," 4940916, July, 1990.

[93]   L. Chen and M. M. El-Gomati, "Fabrication of micro-field emitters on ceramic substrates," Microelectronic Engineering, vol. 84, pp. 95-100, 1, 2007.

[94]   S. Itoh, "Current Status of the Spindt-type Field Emitter," Discharges and Electrical Insulation in Vacuum, 2006. ISDEIV '06. International Symposium on, vol. 2, pp. 875-876, 2006.

[95]   J. D. Levine, "Benefits of the lateral resistor in a field effect display," in 1996, pp. 2008-2010.

[96]   G. N. A. van Veen, "Space-charge effects in spindt-type field emission cathodes," in 1994, pp. 655-661.

[97] C. A. Spindt, C. E. Holland and R. D. Stowell, "Field emission cathode array development for high-current-density applications," in 3rd Tri-Service Cathode Workshop, 1983, pp. 268-76.

[98] P. R. Schwoebel, "Field emission arrays for medical x-ray imaging," Appl. Phys. Lett., vol. 88, pp. 113902, 13 March 2006, 2006.

[99] L. Gangloff, E. Minoux, K. B. K. Teo, P. Vincent, V. T. Semet, V. T. Binh, M. H. Yang, I. Y. Y. Bu, R. G. Lacerda, G. Pirio, J. P. Schnell, D. Pribat, D. G. Hasko, G. A. J. Amaratunga, W. I. Milne and P. Legagneux, "Self-Aligned, Gated Arrays of Individual Nanotube and Nanowire Emitters," Nano Letters, vol. 4, pp. 1575-1579, 09/01, 2004.

[100] G. Pirio, P. Legagneux, D. Pribat, K. B. K. Teo, M. Chhowalla, G. A. J. Amaratunga and W. I. Milne, "Fabrication and electrical characteristics of carbon nanotube field emission microcathodes with an integrated gate electrode," Nanotechnology, vol. 13, pp. 1-4, 2002.

[101] M. A. Guillorn, X. Yang, A. V. Melechko, D. K. Hensley, M. D. Hale, V. I. Merkulov, M. L. Simpson, L. R. Baylor, W. L. Gardner and D. H. Lowndes, "Vertically aligned carbon nanofiber-based field emission electron sources with an integrated focusing electrode," J. Vac. Sci. Technol. B, vol. 22, pp. 35-39, January 2004, 2004.

[102] W. Shao, M. Q. Ding, C. Chen, X. Li, G. Bai and J. J. Feng, "Micro-gated-field emission arrays with single carbon nanotubes grown on Mo tips," Appl. Surf. Sci., vol. 253, pp. 7559-7562, 7/15, 2007.

[103] D. S. Y. Hsu and J. Shaw, "Integrally gated carbon nanotube-on-post field emitter arrays," Appl. Phys. Lett., vol. 80, pp. 118-120, January 7, 2002, 2002.

[104] D. S. Y. Hsu and J. L. Shaw, "Robust and regenerable integrally gated carbon nanotube field emitter arrays," J. Appl. Phys., vol. 98, pp. 1-10, 2005.

[105] M. Chhowalla, K. B. K. Teo, C. Ducati, N. L. Rupesinghe, G. A. J. Amaratunga, A. C. Ferrari, D. Roy, J. Robertson and W. I. Milne, "Growth process conditions of vertically aligned carbon nanotubes using plasma enhanced chemical vapor deposition," J. Appl. Phys., vol. 90, pp. 5308-17, 11/15, 2001.

[106] K. B. K. Teo, M. Chhowalla, G. A. J. Amaratunga, W. I. Milne, D. G. Hasko, G. Pirio, P. Legagneux, F. Wyczisk and D. Pribat, "Uniform patterned growth of carbon nanotubes without surface carbon," Appl. Phys. Lett., vol. 79, pp. 1534-6, 2001.

[107] K. B. K. Teo, S. Lee, M. Chhowalla, V. Semet, V. T. Binh, O. Groening, M. Castignolles, A. Loiseau, G. Pirio, P. Legagneux, D. Pribat, D. G. Hasko, H. Ahmed, G. A. J. Amaratunga and W. I. Milne, "Plasma enhanced chemical vapour deposition carbon nanotubes/nanofibres—how uniform do they grow?" Nanotechnology, vol. 14, pp. 204-211, 2003.

[108] S. Kanemaru, T. Hirano, K. Honda and J. Itoh, "Stable emission from a MOSFET-structured emitter tip in poor vacuum," Appl. Surf. Sci., vol. 146, pp. 198-202, 5, 1999.

[109] W. Zhu, Vacuum Microelectronics. New York: New York : Wiley, 2001.

[110] Electron source with microtip emissive cathodes, R. Meyer. Mar 16,1993). 5194780 .

[111] W. I. Milne, K. B. K. Teo, G. A. J. Amaratunga, P. Legagneux, L. Gangloff, J. -. Schnell, V. Semet, V. Thien Binh and O. Groening, "Carbon nanotubes as field emission sources," Journal of Materials Chemistry, vol. 14, pp. 933-943, 2004.

[112] W. Wei, Y. Liu, Y. Wei, K. Jiang, L. Peng and S. Fan, "Tip cooling effect and failure mechanism of field-emitting carbon nanotubes," Nano Letters, vol. 7, pp. 64-68, 2007.

[113] W. Wei, K. Jiang, Y. Wei, M. Liu, H. Yang, L. Zhang, Q. Li, L. Liu and S. Fan, "Measuring the stress in field-emitting carbon nanotubes," Nanotechnology, vol. 17, pp. 1994-1998, 2006.

[114] P. Vincent, S. T. Purcell, C. Journet and V. T. Binh, "Modelization of resistive heating of carbon nanotubes during field emission," Phys.Rev.B, vol. 66, pp. 075406, Aug, 2002.

[115] N. Y. Huang, J. C. She, J. Chen, S. Z. Deng, N. S. Xu, H. Bishop, S. E. Huq, L. Wang, D. Y. Zhong, E. G. Wang and D. M. Chen, "Mechanism responsible for initiating carbon nanotube vacuum breakdown," Phys. Rev. Lett., vol. 93, pp. 075501-1, 2004.

[116] Z. L. Wang, R. P. Gao, W. A. de Heer and P. Poncharal, "In situ imaging of field emission from individual carbon nanotubes and their structural damage," Appl. Phys. Lett., vol. 80, pp. 856-858, February 4, 2002, 2002.

[117] J. -. Bonard, C. Klinke, K. A. Dean and B. F. Coll, "Degradation and failure of carbon nanotube field emitters," Phys.Rev.B, vol. 67, pp. 115406, Mar, 2003.

[118] A. G. Rinzler, J. H. Hafner, P. Nikolaev, P. Nordlander, D. T. Colbert, R. E. Smalley, L. Lou, S. G. Kim and D. Tomanek, "Unraveling Nanotubes: Field Emission from an Atomic Wire," Science, vol. 269, pp. 1550-1553, September 15, 1995.

[119] M. Doytcheva, M. Kaiser and N. d. Jonge, "In situ transmission electron microscopy investigation of the structural changes in carbon nanotubes during electron emission at high currents," Nanotechnology, vol. 17, pp. 3226-3233, 2006.

[120] K. A. Dean, T. P. Burgin and B. R. Chalamala, "Evaporation of carbon nanotubes during electron field emission," Appl. Phys. Lett., vol. 79, pp. 1873-1875, 2001.

[121] Z. Yao, C. L. Kane and C. Dekker, "High-Field Electrical Transport in Single-Wall Carbon Nanotubes," Phys. Rev. Lett., vol. 84, pp. 2941-2944, Mar, 2000.

[122] P. G. Collins, M. Hersam, M. Arnold, R. Martel and P. Avouris, "Current Saturation and Electrical Breakdown in Multiwalled Carbon Nanotubes," Phys. Rev. Lett., vol. 86, pp. 3128-3131, Apr, 2001.

[123] J. J. Li, C. Z. Gu, Q. Wang, P. Xu, Z. L. Wang, Z. Xu and X. D. Bai, "Field emission from high aspect ratio tubular carbon cones grown on gold wire," Appl. Phys. Lett., vol. 87, pp. 143107, 2005.

[124] K. B. K. Teo, M. Chhowalla, G. A. J. Amaratunga, W. I. Milne, G. Pirio, P. Legagneux, F. Wyczisk, D. Pribat and D. G. Hasko, "Field emission from dense, sparse, and patterned arrays of carbon nanofibers," Appl. Phys. Lett., vol. 80, pp. 2011, 2002.

[125] L. Nilsson, O. Groening, C. Emmenegger, O. Kuettel, E. Schaller, L. Schlapbach, H. Kind, J. -. Bonard and K. Kern, "Scanning field emission from patterned carbon nanotube films," Appl. Phys. Lett., vol. 76, pp. 2071-2073, 2000.

[126] R. C. Smith and S. R. P. Silva, "Maximizing the electron field emission performance of carbon nanotube arrays," Appl. Phys. Lett., vol. 94, pp. 133104, 30 March 2009, 2009.

[127] T. Utsumi, "Vacuum microelectronics: what's new and exciting," Electron Devices, IEEE Transactions on, vol. 38, pp. 2276-2283, 1991.

[128] J. Chen1, Y. Y. 1. Dai, J. 1. Luo, Z. L. 1. Li, S. Z. 1. Deng, J. C. 1. She and N. S. 1. Xu, "Field emission display device structure based on double-gate driving principle for achieving high brightness using a variety of field emission nanoemitters," Appl. Phys. Lett., vol. 90, pp. 253105-1, 06/18, 2007.

[129] J. Zhu, B. Zeng, X. Liu, S. Tian and Z. Yang, "Simulation of Field Emission Micro-Triode Based on Coaxial Nanostructure," Journal of Infrared, Millimeter and Terahertz Waves, vol. 30, pp. 94-102, 01/01, 2009.

[130] A. Di Carlo, A. Pecchia, E. Petrolati and C. Paoloni, "Modeling of carbon nanotube-based devices: from nanoFETs to THz emitters," pp. 632808-632808-11, 2006.

[131] M. A. Guillorn, A. V. Melechko, V. I. Merkulov, D. K. Hensley, M. L. Simpson and D. H. Lowndes, "Self-aligned gated field emission devices using single carbon nanofiber cathodes," Appl. Phys. Lett., vol. 81, pp. 3660-3662, 2002.

[132] M. Q. Ding, W. S. Shao, X. H. Li, G. D. Bai, F. Q. Zhang, H. Y. Li and J. J. Feng, "Approach for fabricating microgated field-emission arrays with individual carbon nanotube emitters," Appl. Phys. Lett., vol. 87, pp. 233118, 2005.

[133] G. Z. Yue, Q. Qiu, B. Gao, Y. Cheng, J. Zhang, H. Shimoda, S. Chang, J. P. Lu and O. Zhou, "Generation of continuous and pulsed diagnostic imaging x-ray radiation using a carbon-nanotube-based field-emission cathode," Appl. Phys. Lett., vol. 81, pp. 355-357, 2002.

[134] A. Dickler, "Xoft Axxent[reg] electronic brachytherapy[mdash]a new device for delivering brachytherapy to the breast," Nat Clin Prac Oncol, vol. 6, pp. 138-142, print, 2009.

[135] X. Qian, A. Tucker, E. Gidcumb, J. Shan, G. Yang, X. Calderon-Colon, S. Sultana, J. Lu, O. Zhou, D. Spronk, F. Sprenger, Y. Zhang, D. Kennedy, T. Farbizio and Z. Jing,

"High resolution stationary digital breast tomosynthesis using distributed carbon nanotube x-ray source array," Med. Phys., vol. 39, pp. 2090-2099, 2012.

[136] Z. Liu, G. Yang, Y. Z. Lee, D. Bordelon, J. Lu and O. Zhou, "Carbon nanotube based microfocus field emission x-ray source for microcomputed tomography," Appl. Phys. Lett., vol. 89, pp. 103111, 2006.

[137] D. S. Engström, N. L. Rupesinghe, K. B. K. Teo, W. I. Milne and P. Bøggild, "Vertically aligned CNT growth on a microfabricated silicon heater with integrated temperature control—determination of the activation energy from a continuous thermal gradient," J Micromech Microengineering, vol. 21, pp. 015004, 2011.

[138] M. B. Jakubinek, M. A. White, G. Li, C. Jayasinghe, W. Cho, M. J. Schulz and V. Shanov, "Thermal and electrical conductivity of tall, vertically aligned carbon nanotube arrays," Carbon, vol. 48, pp. 3947-3952, 201011, 2010.

[139] X. Liu, K. H. R. Baronian and A. J. Downard, "Patterned Arrays of Vertically Aligned Carbon Nanotube Microelectrodes on Carbon Films Prepared by Thermal Chemical Vapor Deposition," Anal. Chem., vol. 80, pp. 8835-8839, 11/15, 2008.

[140] S. Fan, M. G. Chapline, N. R. Franklin, T. W. Tombler, A. M. Cassell and H. Dai, "Self-Oriented Regular Arrays of Carbon Nanotubes and Their Field Emission Properties," Science}, vol. 283, pp. 512-514, 1999.

[141] D. Li, L. Dai, S. Huang, A. W. H. Mau and Z. L. Wang, "Structure and growth of aligned carbon nanotube films by pyrolysis," Chemical Physics Letters, vol. 316, pp. 349, 2000.

[142] L. X. Benedict, S. G. Louie and M. L. Cohen, "Static polarizabilities of single-wall carbon nanotubes," Phys.Rev.B, vol. 52, pp. 8541-8549, Sep, 1995.

[143] V. I. Merkulov, D. H. Lowndes, Y. Y. Wei, G. Eres and E. Voelkl, "Patterned growth of individual and multiple vertically aligned carbon nanofibers," Appl. Phys. Lett., vol. 76, pp. 3555-3557, June 12, 2000, 2000.

[144] Z. F. Ren, Z. P. Huang, J. W. Xu, J. H. Wang, P. Bush, M. P. Siegal and P. N. Provencio, "Synthesis of Large Arrays of Well-Aligned Carbon Nanotubes on Glass," Science, vol. 282, pp. 1105-1107, November 6, 1998.

[145] Y. Tu, Y. Lin and Z. F. Ren, "Nanoelectrode Arrays Based on Low Site Density Aligned Carbon Nanotubes," Nano Letters, vol. 3, pp. 107-109, 01/01, 2003.

[146] C. F. Herrmann, F. H. Fabreguette, D. S. Finch, R. Geiss and S. M. George, "Multilayer and functional coatings on carbon nanotubes using atomic layer deposition," Appl. Phys. Lett., vol. 87, pp. 123110, 19 September 2005, 2005.

[147] S. M. George, "Atomic Layer Deposition: An Overview," Chem. Rev., vol. 110, pp. 111-131, 2010.

[148] W. I. Milne, Chi Li, Yan Zhang, D. G. Hasko, P. Hiralal, M. Mann, H. E. Unalan, G. A. J. Amaratunga, M. Cole, Daping Chu, Wei Lei, D. Pribat, J. Jang and Baoping Wang, "Optimisation of CNTs and ZnO nanostructures for electron sources," in Nanotechnology (IEEE-NANO), 2010 10th IEEE Conference on, 2010, pp. 62-65.

[149] Yonghai Sun, J. T. W. Yeow and D. A. Jaffray, "Simulation of field emission current uniformity of low-density freestanding CNT array," in Nanotechnology (IEEE-NANO), 2010 10th IEEE Conference on, 2010, pp. 836-840.

[150] H. Gamo, M. Kikuchi, T. Shibasaki, T. Ando, H. Tomokage and M. Nishitani-Gamo, "Field Emission Current Uniformity and Stability of Well-Aligned Carbon Nanotubes Synthesized in Methanol," Japanese Journal of Applied Physics, vol. 47, pp. 6606-6609, 2008.

[151] N. Liu, G. Fang, X. Yang, W. Zeng, C. Li, M. Wang, J. Li and X. Zhao, "Synthesis of patterned carbon nanotube arrays for field emission using a two layer Sn/Ni catalyst in an ethanol flame," Diamond and Related Materials, vol. 18, pp. 1375, 2009.

[152] X. Calderon-Colon, H. Geng, B. Gao, L. An, G. Cao and O. Zhou, "A carbon nanotube field emission cathode with high current density and long-term stability," Nanotechnology, vol. 20, pp. 325707 (5pp), 2009.

[153] M. Drechsler, "Erwin Müller and the early development of field emission microscopy," Surf Sci, vol. 70, pp. 1, 1978.

[154] W. Liu, S. Hou, Z. Zhang, G. Zhang, Z. Gu, J. Luo, X. Zhao and Z. Xue, "Atomically resolved field emission patterns of single-walled carbon nanotubes," Ultramicroscopy, vol. 94, pp. 175, 2003.

[155] M. Sasaki and T. Hibi, "High Resolution FEM Image of Tungsten," Japanese Journal of Applied Physics, vol. 9, pp. 405-405, 1970.

[156] D. J. Rose, "On the Magnification and Resolution of the Field Emission Electron Microscope," J. Appl. Phys., vol. 27, pp. 215-220, March 1956, 1956.

[157] B. Barwinski and S. Sendecki, "Fine structure of scanning field emission microscope (SFEM) image," Vacuum, vol. 47, pp. 1479, 1996.

[158] D. M. Tanenbaum, C. W. Lo, M. Isaacson, H. G. Craighead, M. J. Rooks, K. Y. Lee, W. S. Huang and T. H. P. Chang, "High resolution electron beam lithography using ZEP-520 and KRS resists at low voltage," in 1996, pp. 3829-3833.

[159] e. a. Huigao Duan, "Preparing patterned carbonaceous nanostructures directly by overexposure of PMMA using electron-beam lithography," Nanotechnology, vol. 20, pp. 135306, 2009.

[160] A. Olkhovets and H. G. Craighead, "Low voltage electron beam lithography in PMMA," J. Vac. Sci. Technol. B, vol. 17, pp. 1366-1370, July 1999, 1999.

[161] S. T. Martin, "On the Thermionic and Adsorptive Properties of the Surfaces of a Tungsten Single Crystal," Phys.Rev., vol. 56, pp. 947-959, Nov, 1939.

[162] Y. Neo, T. Matsumoto, M. Tomita, M. Sasaki, T. Aoki and H. Mimura, "Revealing real images of cloverleaf pattern emission sites by using field ion microscopy," in 2010, pp. C2A1-C2A4.

[163] W. Liu, F. Zeng, L. Xin, C. Zhu and Y. He, "Turn-on field distribution of field-emitting sites in carbon nanotube film: Study with luminescent image," Journal of Vacuum Science and Technology B: Microelectronics and Nanometer Structures, vol. 26, pp. 32-35, 2008.

[164] J. H. Lee, S. H. Lee, W. S. Kim, H. J. Lee, J. N. Heo, T. W. Jeong, C. H. Choi, J. M. Kim, J. H. Park, J. S. Ha, H. J. Lee, J. W. Moon, M. A. Yoo, J. W. Nam, S. H. Cho, T. I. Yoon, B. S. Kim and D. H. Choe, "Uniformity measurement of electron emission from carbon nanotubes using electron-beam resist," in 2005, pp. 718-722.

[165] B. Zajec, V. Nemanič, M. Žumer, E. N. Bryan and R. J. Nemanich, "Ring-shaped field emission patterns from carbon nanotube films," Carbon, vol. 49, pp. 3332-3339, 8, 2011.

[166] D E Grider and A Wright and,P.K.Ausburn, "Electron beam melting in microfocus X-ray tubes," J. Phys. D, vol. 19, pp. 2281, 1986.